

# Application of Adaptive Optics to Focusing and Imaging

THÈSE N° (2011)

PRÉSENTÉE LE 16 DÉCEMBRE 2011

À LA FACULTÉ INFORMATIQUE ET COMMUNICATIONS  
EMPA SECTION ÉLECTRONIQUE, MÉTROLOGIE, FIABILITÉ  
PROGRAMME DOCTORAL EN INFORMATIQUE, COMMUNICATIONS ET INFORMATION

ÉCOLE POLYTECHNIQUE FÉDÉRALE DE LAUSANNE

POUR L'OBTENTION DU GRADE DE DOCTEUR ÈS SCIENCES

Par

Daniel IWANIUK

acceptée sur proposition du jury:

Prof. C. Petitpierre, président du jury  
Prof. P. Rastogi, directeur de these  
Dr. E. Hack, rapporteur  
Prof. L. Bruno, rapporteur  
Dr. D. Inaudi, rapporteur

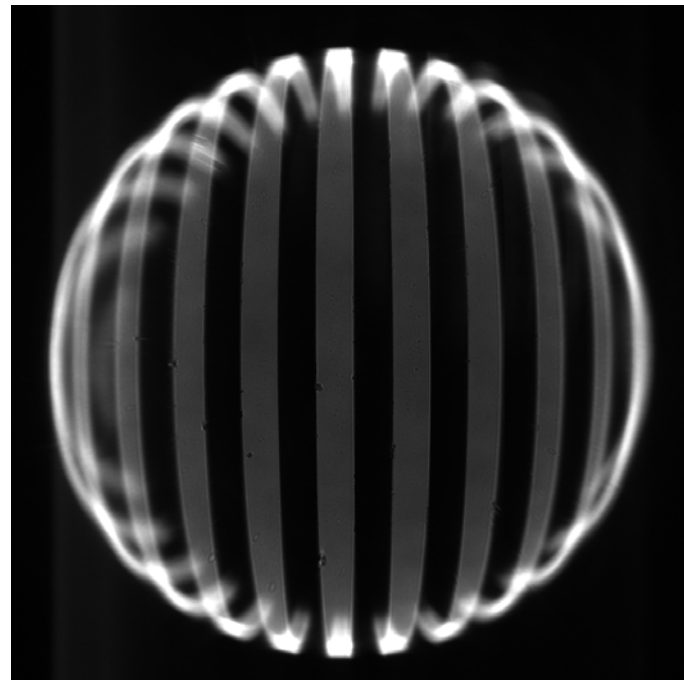


Dübendorf, Suisse

2011



# Application of Adaptive Optics to Focusing and Imaging



Daniel Iwaniuk

This thesis was funded by:



# Acknowledgement

I first thank Professor Rastogi for giving me the opportunity to do my research in such an interesting field and for very enlightening and encouraging discussions. Equally many thanks go to my supervisor Erwin Hack. Erwin's questions, remarks and suggestions pushed my progress through many difficult stages and improved the final work significantly.

I further thank the following people for their support and help:

- Simon Kuster from the Laboratory for Functional Polymers at Empa for the provision of and support in handling of fluorescent markers.
- Claudia Buser from Aquatic Ecology at EAWAG for the biological samples, which provided the awesome pictures as example for an imaging application.
- The group for Electronics, Metrology and Reliability at Empa for their great support in electronics, informatics, mechanics and general help in the lab, which made my daily life in research more comfortable.
- Prof. Rastogi's group, in particular Sai Siva Gorthi and Rajshekhar Gannavarpu for the support with the administration at EPFL.
- Robert Apter from CCAT to arouse our interest in high DOF lenses and for his collaboration in a CTI project.

## Acknowledgement

---

I very much enjoyed the daily work with my office and lab colleagues and I therefore thank René Mooser, Roman Furrer, Olivier Scholder, Eugen Zgraggen, Ivan Shorubalko, Konstantins Jefimovs, Victor Callegari, Rolf Brönnimann, Claudia Müller, and Christoph Keller for the pleasant time.

I also thank my family and friends for the immense support and the great time I had during my PhD. I love my parents for their efforts in motivating and financing me and for their never ending trust and believe (serdecznie dziękuję!). Thank you, Vera, for the daily support and cheering up you gave me. I owe you the power to finish my thesis and to get through cumbersome and exhausting moments. I further thank Chris Gräzer for many encouraging and intense discussions; they always inspired me and provided a new point of view on complicated topics. His general experience and immense help brought me to a higher personal level. I had magical moments with my friends Justus and Julian on Friday nights, which let me forget all about mundane negligibilities.

# Abstract

Adaptive optics is used to abate aberrations with a wavefront correction. It is widely used in astronomy and is starting to expand into applications of laser focusing and imaging with high numerical apertures, e.g. microscopy. The physical background of focusing laser light and imaging is the same, so we can use the same methods. In both cases, light is propagating through a lens; either it becomes focused into a small region or light from a small region becomes imaged on a camera. Modulations applied on the lens to implement wavefront corrections behave similarly in both applications. A powerful simulation tool was created to characterize the impact of those modulations. As an example, we validated a design for a Fresnel lens produced on a glass fibre tip to focus its emitting light.

We have developed solutions mainly for three different problems. First, a high depth of focus enables keeping a laser beam focused within a larger length or imaging objects from different positions simultaneously. In photography, this can be attained by stopping down the aperture, which introduces a huge loss of light. State-of-the-art for focusing into a line segment also shows an inefficient performance. We present an elegant lens design, which enables highly efficient elongation of the depth of focus. Preliminary studies have shown that it might be a feasible alternative for current intra-ocular lens implants in ophthalmology or for 3D visualization in imaging and microscopy. A high depth of focus also has a large potential in optical lithography and data storage, because the focal position is enlarged and does not have to be adjusted precisely to obtain a useful spot.

## Abstract

---

Second, specimen-induced aberrations can affect even a perfectly adjusted, diffraction limited lens system. A planar refraction index mismatch introduces spherical aberrations, degrading the optical resolution. As a first step to correct them, we were able to characterize simultaneously the refractive index and the thickness of an unknown medium that is placed between the lens and its focal region. This was done by clever manipulation of the beam angles with the same adaptive optics element in the focusing and in the imaging system.

Finally, the medium-induced spherical aberrations were corrected based on the characterization results. The point spread function degradation of a focused laser beam was completely removed, which might be useful in optical tweezers or in laser processing of biological samples. While imaging through the planar refractive index mismatch, the bending of the object field was corrected and the diffraction limited performance restored.

Keywords: Adaptive Optics, wavefront correction, phase modulation, SLM, PSF simulation, high depth of field, microscopy, planar refractive index mismatch, imaging aberrations, Fresnel lens.

# Zusammenfassung

Adaptive Optik wird verwendet, um Aberrationen mit Hilfe von Modulationen der Wellenfront zu korrigieren. In der Astronomie ist deren Gebrauch bereits seit Jahren üblich und beginnt sich nun in andere Anwendung auszubreiten, zum Beispiel für das Fokussieren von Lasern und in Abbildungssystemen mit hoher numerischer Apertur (z.B. Mikroskopie). Das Fokussieren von Laserstrahlen und das Abbilden haben denselben physikalischen Hintergrund, was es uns erlaubt, dieselbe Methodik zu verwenden. In beiden Fällen propagiert Licht durch eine Linse und wird entweder auf eine kleine Region fokussiert oder Licht einer kleinen Region wird auf eine Kamera abgebildet. Eine auf die Linse angewendete Korrektur der Wellenfront verhält sich gleich in beiden Systemen. Wir haben ein leistungsfähiges Simulationstool entwickelt, um die Auswirkungen verschiedener Modulationen zu charakterisieren. Wir haben die Simulationen validiert mit dem Design einer Fresnel Linse, die auf einer Glasfaserspitze aufgebracht wurde, um dessen emittiertes Licht zu fokussieren.

In unserer Arbeit haben wir hauptsächlich drei Probleme adressiert. Erstens eine erhöhte Tiefenschärfe, die das Fokussieren eines Laserstrahls über eine grössere Distanz oder das gleichzeitige Abbilden von Objekten aus verschiedenen Distanzen erlaubt. In der Photographie wird ein ähnlicher Effekt mit einer Reduktion der Blende erreicht, was zu sehr grossen Intensitätsverlusten führt. Auch Lösungen nach dem neusten Stand der Technik für das Fokussieren in ein Liniensegment weisen eine schlechte Effizienz auf. Wir präsentieren hierzu ein elegantes Design, das eine sehr effiziente Erhöhung der Tiefenschärfe erreicht. Erste Vorstudien haben gezeigt, dass unsere Methode für künstliche Augenlinsen in der Ophthalmologie oder für die

Visualisierung von 3D Objekten eine potentielle Anwendung findet. Eine erhöhte Tiefenschärfe weist auch interessante Anwendungen auf im Bereich der optischen Lithographie und der optischen Datenspeicherung. Mit unserem Design braucht der Laserstrahl nicht präzis eingestellt zu werden, weil über eine grosse Distanz ein brauchbarer Spot erreicht wird.

Zweitens können von der Probe induzierte Aberrationen auch ein perfekt eingestelltes, beugungsbegrenztes Linsensystem beeinträchtigen. Ein ebenflächiger Versatz des Brechungsindex erzeugt sphärische Aberrationen, die sich negativ auf die optische Auflösung auswirken. Als ersten Schritt zur Korrektur bestimmten wir die Dicke und den Brechungsindex eines unbekannten Mediums, das zwischen der Linse und dem Fokus platziert wurde. Die Charakterisierung wurde mittels raffinierter Manipulation der Strahlwinkel durchgeführt. Dieselben adaptiven Optiken wurden verwendet für ein Fokussier- und ein Abbildungssystem.

Schlussendlich wurden die durch das Fokussieren in das Medium eingeführten sphärischen Aberrationen anhand der Resultate der Charakterisierung korrigiert. Die Degradation der Punktspreizfunktion eines fokussierten Laserstrahls wurde komplett aufgehoben. Dies kann in Systemen für optische Pinzetten oder für die Lasermanipulation von biologischen Zellen genutzt werden. Beim Abbilden durch das Medium wurde eine Krümmung des Bildfeldes beobachtet, die ebenfalls komplett korrigiert wurde. Eine beugungsbegrenzte Performance wurde mit Hilfe der adaptiven Optik wieder hergestellt.

Schlüsselwörter: Adaptive Optik, Korrektur der Wellenfront, Phasenmodulation, SLM, PSF Simulation, erhöhte Tiefenschärfe, Mikroskopie, Brechungsindex, Abbildungsfehler, Fresnel Linse.

# Table of Contents

1.	Imaging and Resolution .....	1
1.1.	Introduction .....	1
1.2.	Imaging resolution – the point spread function.....	4
1.3.	Imaging aberrations .....	8
1.4.	Resolution in microscopy .....	11
1.5.	Imaging techniques in microscopy .....	14
1.6.	Superresolution in microscopy .....	15
1.7.	Adaptive optics.....	17
1.8.	Pupil filter.....	18
2.	Materials & Methods .....	21
2.1.	Overview .....	21
2.2.	PSF calculation.....	22
2.2.1.	Scalar diffraction theory .....	22
2.2.2.	Lens function .....	24
2.2.3.	Error estimation of the used approximations.....	27
2.2.4.	Simulation tool / implementation into MATLAB .....	29
2.3.	Figures of merit .....	30
2.4.	Experimental PSF analysis.....	34
2.4.1.	Phase modulator .....	36
2.4.2.	Focusing into glass .....	42
2.5.	Simulation validation with Fresnel lenses on optical fibre tips.....	44
3.	Extended Depth of Field for Intra-Ocular Lens Implants .....	47
3.1.	Concept and applications of high DOF systems .....	48
3.2.	Development of intra-ocular lens implants with increased DOF .....	49
3.2.1.	Cataract surgery and intra-ocular lenses.....	49
3.2.2.	State-of-the-art of IOLs .....	52
3.3.	State-of-the-art of pupil filter designs for extended DOF .....	54
3.4.	Quartic Multiplex (QM) lens design .....	55

## Table of Contents

---

3.5.	QM focusing results .....	59
3.5.1.	Numerical results.....	59
3.5.2.	Experimental results .....	62
3.5.3.	Discussion .....	64
3.6.	Extended simulation studies for specific applications .....	66
3.6.1.	Performance comparison of $\rho^4$ and $\rho^6$ terms .....	66
3.6.2.	Simulations of finite distance imaging .....	68
3.6.3.	Simulations of white light illumination .....	69
3.7.	Conclusion	
4.	Correction of Spherical Aberrations in Focusing Applications .....	73
4.1.	State-of-the-art of aberration correction.....	74
4.2.	Characterization of the aberration inducing medium.....	76
4.3.	PSF Measurement system .....	78
4.4.	Results for the glass plates .....	81
4.5.	Measurement results for an aberrated system .....	83
4.6.	Aberration correction with a phase SLM .....	84
4.7.	Accuracy estimation based on numerical simulations .....	86
4.8.	Conclusion.....	88
5.	Adaptive Optics Implemented in Microscopy.....	91
5.1.	Setup of the model microscope .....	92
5.1.1.	Alignment of the microscope .....	94
5.2.	Extended depth of field .....	98
5.3.	In-situ extraction of the refractive index and the thickness of a medium in imaging .....	103
5.3.1.	Apertures generated in-situ by the phase SLM .....	103
5.3.2.	Evaluation concept of the unknown parameters of the medium.....	105
5.4.	Spherical aberration correction .....	107
5.5.	Conclusion.....	112
6.	Conclusion .....	115
7.	Bibliography .....	118



# Chapter 1

## Imaging and Resolution

### 1.1. Introduction

Imaging processes visualize information from physical objects. Eyes are performing this task almost to perfection. Imaging by the human eye involves three main processes: image formation with the optical lens system, conversion of the information to an electronic signal by the retina acting as the detector, and finally image processing by the brain. Modern imaging systems follow the same three steps to generate a picture, which is inspected by our eyes. Examples are printed pictures or a display screen. The research progress of the last centuries greatly improved all three processing steps. By using imaging systems, we are now able to visualise details, which we could otherwise not see with the naked eye.

In the 13th-century, magnification glasses were introduced mainly to find more details of nature. Pushing the limits to decrease the observable object size, optical microscopy is nowadays able to visualise features as small as a few nanometres. At the other extreme, in 1609, Galileo Galilei substantially improved the telescopes to observe the stars and planets. Today, telescopes allow us to study light from around 13 billion light years away and to find planets in neighbouring solar systems. In the last century, advances in computer power and image capturing devices increasingly improved the processing of information and the storage of immense amounts of data.

## 1. Imaging and Resolution

---

Despite enormous improvements achieved, researchers still try to push physical limitations in imaging further. The main field of our investigation lies in optical full-field imaging and microscopy for real-time observation of biological samples, where we address two limitations:

(1) In most cases, the depth of field of standard imaging systems is too small to obtain a complete, sharp image of a 3D object. High depth of focus (DOF) systems have great potential for applications, for example, in endoscopic optical coherence tomography, microscopy, ophthalmology, material science, live-cell biology and automated recognition of multiple objects at different distances. Such applications require a constantly high imaging quality over an elongated axial region. High DOF could provide a purely optical image of a 3D object in a single-shot without the need for further computational image processing. Current methods achieve a full 3D representation by different approaches. Scanning the focus in the axial direction is time and computational resource consuming. Techniques, such as pseudo non-diffracting beams (PNDB) and pupil modulation filters, are primarily limited by very low light efficiency, inhomogeneities in resolution for different axial positions, complex diffractive optical elements, which are difficult to produce and introduce scattered light due to diffraction. Solutions for good image quality in combination with high resolution for every object within the depth of field are still scarce.

To extend the depth of field, we developed a phase modulation filter. It leads to a constant transversal resolution within the extended depth of field with a good light efficiency and relatively simple structure (see *chapter 3*).

(2) A severe limitation in imaging is aberration, which can occur in every measurement system. Usually, aberrations reduce resolution, contrast and image quality. An imaging system gets more sensitive to aberrations with higher numerical apertures. Although manufacturers of microscope objectives eliminate aberrations from known imperfections in the lens system, specimen-induced aberrations still remain. These might be induced by the medium surrounding an object or from imaging deep into a specimen. Basic formulas and corrections are known for certain geometrical shapes of a phase medium between the object under investigation and the imaging system. In real samples, however, the task of characterizing the phase

## 1. Imaging and Resolution

---

medium responsible for the aberration remains difficult. Standard techniques are able to measure the optical thickness only, which depends on the physical thickness and the optical density (refractive index) of the material. For a successful aberration correction, the two measures need to be known individually. Some microscopic techniques have been developed to measure the refractive index or the physical thickness separately, such as refractometry, ellipsometry or digital holography. A big disadvantage of these techniques is, however, that they require the use of two independent systems consecutively to fully characterize a medium. This entails difficulties, for instance, if the environment or the sample changes between the two measurements.

Our solution to correct for aberrations is an elegant in-situ method to get both values, the physical thickness and the refractive index, directly from two measurements with a modified microscope without remounting the object or changing the measurement system. Based on the fact that aberrations are angle dependent, we use different imaging apertures to characterize the source of aberration completely and correct them consecutively with appropriate phase modulation filters (see *chapter 4*).

We built a model microscope with an implemented phase modulator to verify the use of our new methods in real imaging. Standard microscopy targets were used to characterize the system extensively. Furthermore, pictures were taken of water fleas to illustrate potential applications in biology. We were able to show an extended depth of focus, correction of spherical aberrations and the characterization of a transparent medium using this imaging setup (see *chapter 5*).

In this chapter, a brief overview, basic relations and important definitions of imaging in microscopy and its recent developments follow. Selected examples of the existing diversity of techniques are briefly discussed. Our developments in numerical simulation and the experimental setups are presented in *chapter 2*.

## 1.2. Imaging resolution – the point spread function

Spatial resolution is a core issue in optical imaging. It is strongly correlated to the wave nature of light. Refraction, diffraction and interference have significant effects on the transversal (lateral) and axial (longitudinal) characteristics when coherent light is used in imaging. The three-dimensional distribution of the light in the focal region is called the point spread function (PSF).

The PSF represents the shape of the spot in transversal and axial direction, when light is focused with a lens system (*fig. 1*). The cylindrical coordinates  $r$  and  $z$  represent the radial and axial distance in the focal region. Using a lens system for imaging, the PSF is used to characterize the spatial resolution (transversal and axial), image quality and imaging aberrations. As the axial and transversal distribution sometimes look very similar, all figures of intensity distributions will be presented with a diagram representing the respective cross-section through the 3D PSF. Figures showing the axial and transversal direction together will be henceforth labelled 3D PSF (compare *fig. 1 top*). Line graphs can be either in axial or in transversal direction (*fig. 1 bottom*).

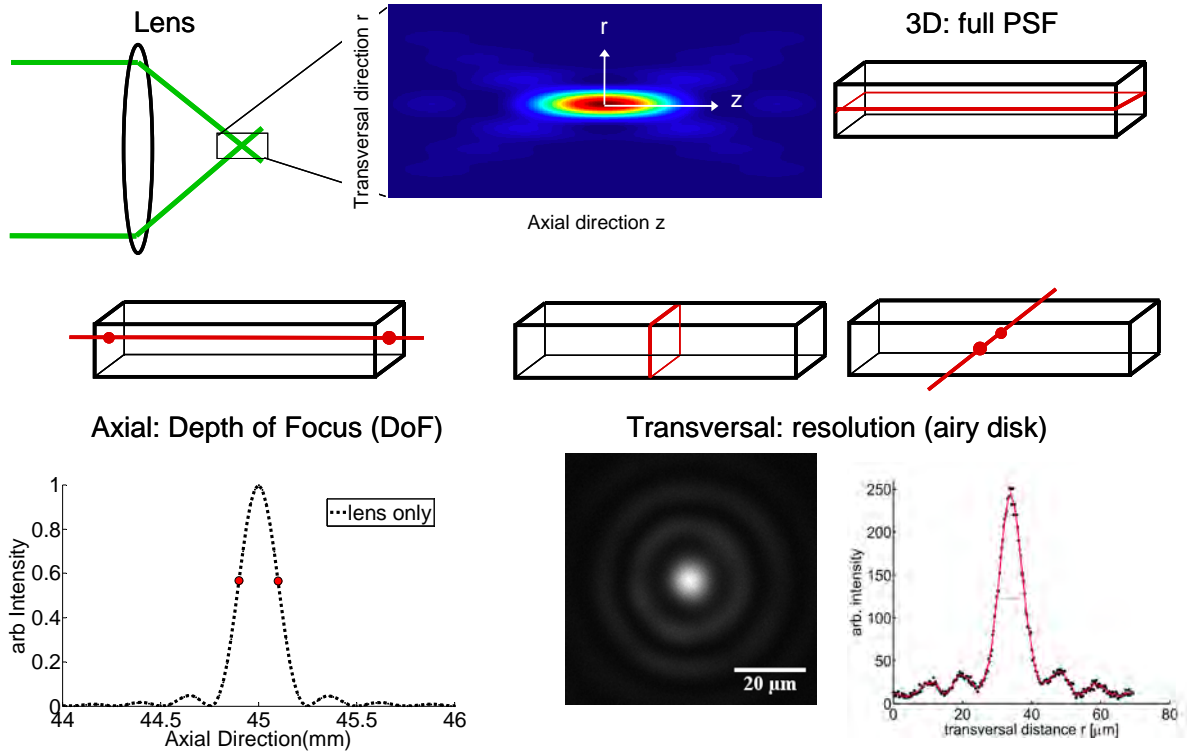


*Figure 1: Representation of the PSF. Top row: lens focusing system, zoom into the 3D PSF; Bottom row: axial cross-section of the PSF (simulated) and 2 representations of the transversal cross-section of the PSF (measured).*

A very basic imaging system is shown in *figure 2*. The specimen under investigation lies in the object plane. A lens within the pupil plane collects the light from the object. It has a radial coordinate  $\rho$  and an acceptance angle  $\alpha_{max}$ . The image is captured by a camera or visually examined with an eyepiece in the image plane with cylindrical coordinates  $r$  and  $z$ . From the analogy of focusing light (*fig. 1 top left*) and imaging (*fig. 2*) it is apparent that the light is travelling in a similar way through the lens system, and that the PSF represents the resolution in both cases.

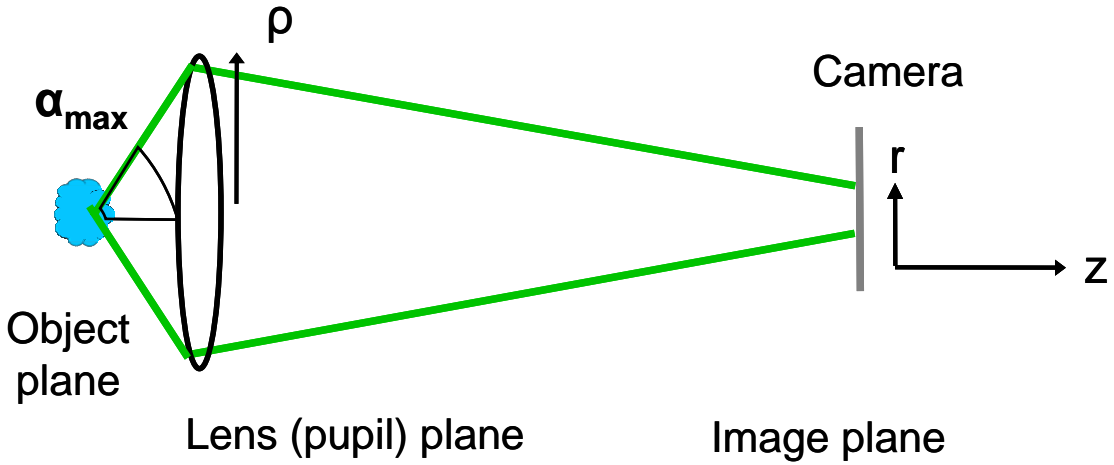


*Figure 2: Coordinate definition of a basic imaging system consisting of an image plane, lens plane (pupil plane) and object plane.  $\rho$  is the radial coordinate within the lens plane;  $\alpha_{max}$  is the maximum acceptance angle.*

If the system is optimized and corrected for the main aberrations (see chapter 1.2) it is called diffraction limited. The diffraction limited PSF of a circular aperture is called Airy disc [1]. The diffraction limited spot has a well-defined minimal spatial extent:  $d_{lim}$  in the transversal (eq. 1) and  $z_{lim}$  in the axial direction (eq. 2).

$$d_{lim} = 0.66 \cdot \lambda / \text{NA} \quad (1)$$

$$z_{lim} = \lambda \cdot n / \text{NA}^2 \quad (2)$$

$\lambda$  is the wavelength and NA the numerical aperture, which depends on the refractive index  $n$  of the medium (air has  $n = 1$ ) and the maximum acceptance angle  $\alpha_{max}$  (eq. 3).

$$\text{NA} = n \cdot \sin \alpha_{max} \quad (3)$$

For a given wavelength, the spot can be reduced by increasing the maximum acceptance angle or by increasing the refractive index of the medium. As the lateral and longitudinal resolutions are related to each other, changing one of them alters the other accordingly. By increasing the lateral resolution, the longitudinal depth of field decreases. This means that only light from a narrow plane is imaged sharply, which reduces the observable field immensely.

The transversal resolution is defined as follows: Two point sources of the object plane are considered resolved in the image plane, if their PSFs are distinguishable (fig. 3c). The Ray-

Leigh resolution criterion [2] is reached if the maximum of one curve overlies the first minimum of the other (*fig. 3b*). If the points get together closer than  $d_{lim}$  their images get overlapped and become indistinguishable and therefore unresolved (*fig. 3a*).

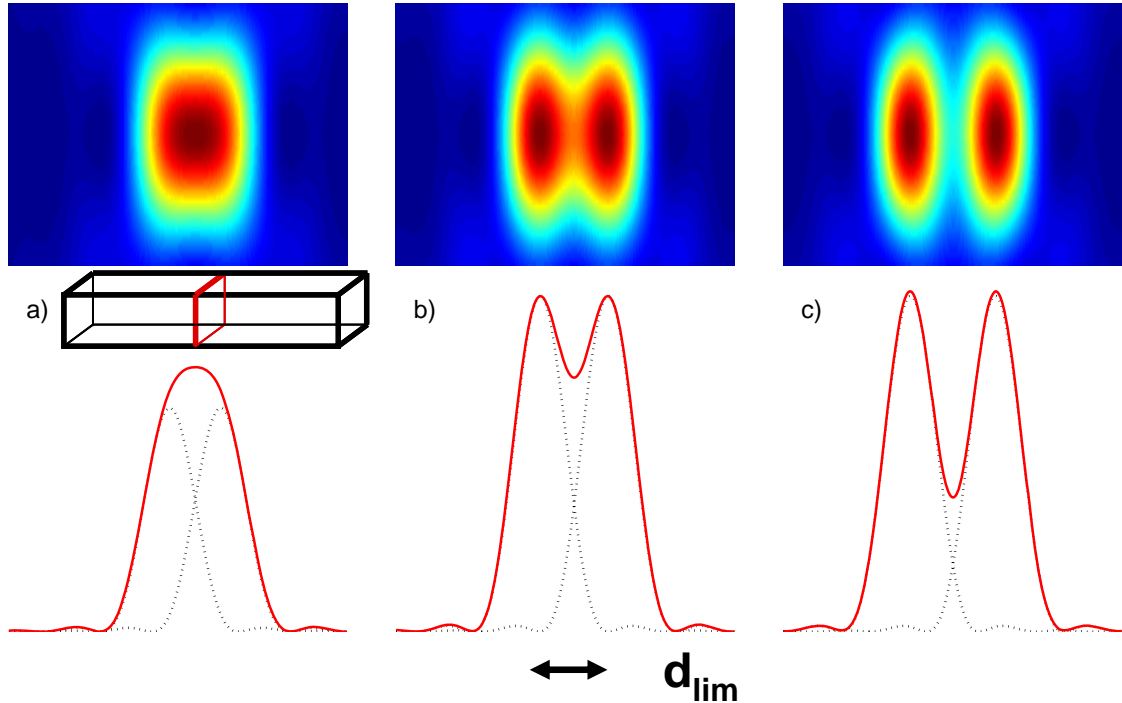


*Figure 3: Rayleigh resolution criterion visualized with transversal cross sections of the image of 2 point sources: a) unresolved, b) maximum resolution criterion according to Rayleigh, c) resolved.*

A conventional optical microscope, for example, with visible light (between 400 and 700 nm) and oil-immersion microscope objective (NA 1.4) has a lateral resolution limited to around 250 nm and a longitudinal resolution of around 500 nm. On the other hand, a single object that is smaller than the resolution limit gets blown up to the size of the limiting PSF. In practice this means that objects close to the diffraction limit must be interpreted carefully as they could be smaller than expected from their image. Further, it is important to focus the setup, such that the picture is taken at the maximum intensity of the axial PSF. If the system is defocused, i.e. shifted in the  $z$  direction according to *fig. 1*, the actual transversal distribution gets wider. This would decrease the actual image resolution.

### 1.3. Imaging aberrations

Different kinds of aberrations can impair the image quality severely. There are two main sources of imaging aberrations: system-induced and specimen-induced aberrations. System-induced aberrations arise from imperfect imaging optics or unequal behaviour of rays with different angle or different wavelength during propagation. Specimen-induced aberrations can occur if the object under investigation is immersed in a surrounding or by imaging deep into the specimen. The latter can occur, for example, when observing the interior of a three-dimensional biological cell through a microscope. The specimen-induced errors can be static or vary in time. The following subsections will describe the origin of aberrations, their effects on imaging and possibilities to correct them.

Many different system-induced aberrations can appear in imaging [3]: chromatic aberration, spherical aberration, field distortion, coma and astigmatism. Chromatic aberration occurs if different colours do not propagate identically through the system (*fig. 4a*). The focal region of green, blue and red light is shifted to each other. This means that an image is sharp at different positions for different colours. The final contrast of a picture, therefore, is decreased, because to a sharp image in one colour, blurry images from the other colours are added.

A lens with spherical aberrations is not able to focus rays at different angles to the same focal plane (*fig. 4b*). Marginal rays are focused either closer to or farther away from the focal point of the central rays resulting in a decrease of axial resolution together with a reduction of image sharpness and contrast. The very same effect distorts the image of a lens affected by coma (*fig. 4c*), where tilted rays are not bundled to the same point. In astigmatism, the axial resolution of the image of two perpendicular lines is unequal. Such asymmetrical imaging leads to different resolution, sharpness and contrast along the *x* and *y* coordinate. Another type of aberrations is field distortion (*fig. 4d*). A grid of straight lines gets distorted to an image with bent lines, either inward or outward.

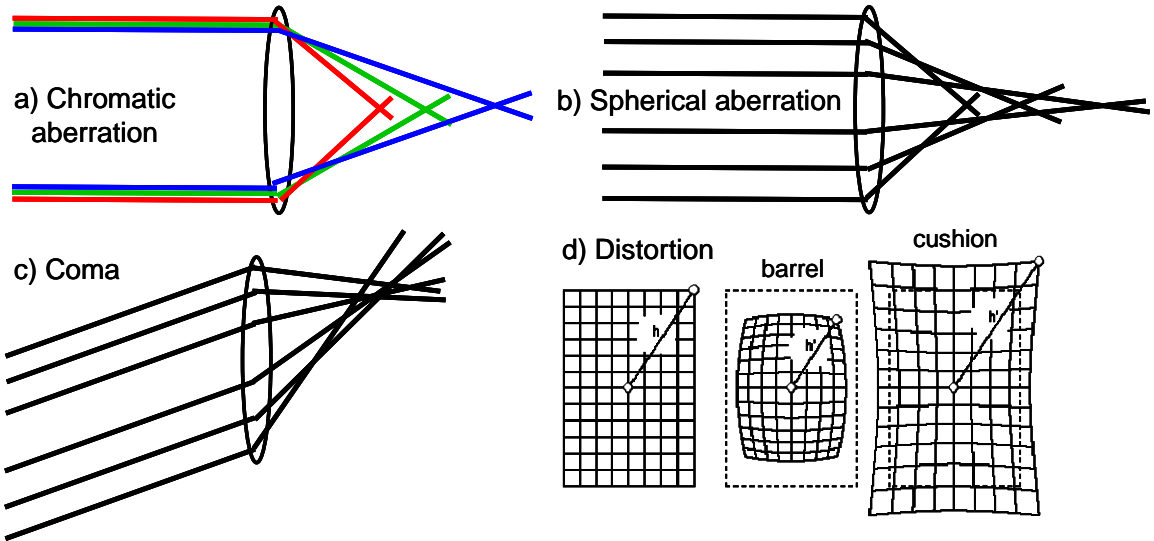


*Figure 4: Impact on imaging of system induced aberrations: a) chromatic aberration, b) spherical aberration, c) coma, d) two kind of distortions (cushion & barrel).*

A distorted wavefront at the pupil plane can be described as a linear superposition of Zernike polynomials (eq. 4). The Zernike terms are a set of orthogonal normalized polynomials (table 1), which are defined within the pupil plane with the normalized radius  $\rho \in [0,1]$  and the azimuth angle  $\theta \in [0, 2\pi]$ . As they are orthogonal to each other, the wavefront can be decomposed and the source of distortion examined with the use of corresponding coefficients. The phase distributions of the aberration polynomials are presented in fig. 5.

$$\phi_{m,n} = \sum_{m,n} a_{m,n} \cdot Z_m^n \quad (4)$$

**Table 1: Zernike polynomials up to the third order.**

$Z_n^m$	$Z_n^m(\rho, \theta) = R_n^m(\rho) \cos(m\theta)$	Description
$Z_0^0$	1	Piston (constant)
$Z_1^1 & Z_1^{-1}$	$\rho \cdot \cos(\theta)$ & $\rho \cdot \sin(\theta)$	x & y tilt
$Z_2^0$	$2\rho^2 - 1$	Defocus
$Z_2^2 & Z_2^{-2}$	$\rho^2 \cdot \cos(2\theta)$ & $\rho^2 \cdot \sin(2\theta)$	0° & 45° astigmatism
$Z_3^1 & Z_3^{-1}$	$(3\rho^2 - 2) \cdot \rho \cdot \cos(\theta)$ & $(3\rho^2 - 2) \cdot \rho \cdot \sin(\theta)$	x & y coma
$Z_4^0$	$6\rho^4 - 6\rho^2 + 1$	Spherical aberration

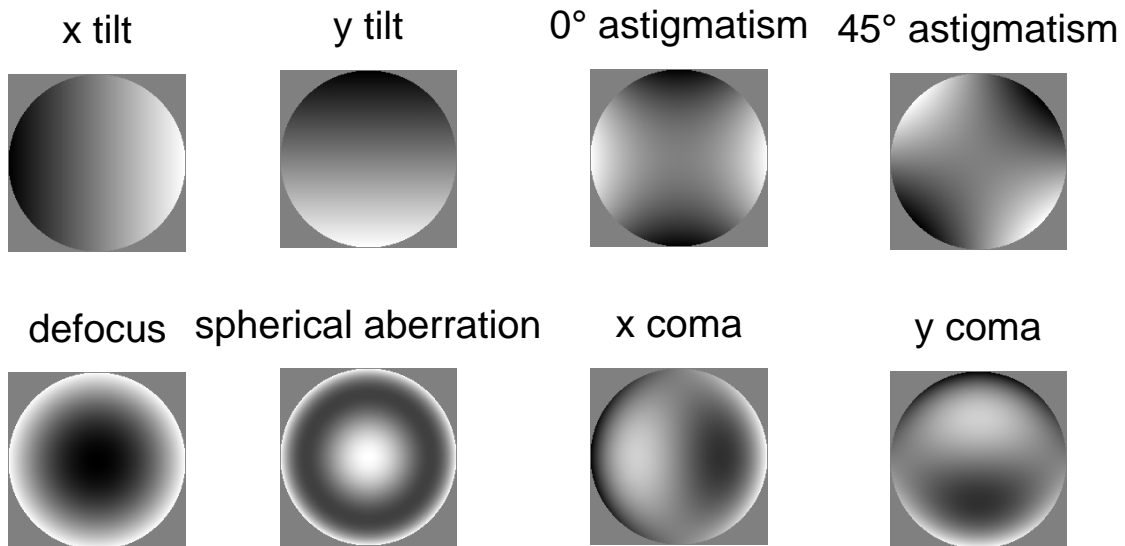


*Figure 5: Visual representation of the Zernike polynomials in the unit disk.  
(black: -1, white: +1)*

System induced aberrations are well studied and corrected in microscope objectives from most manufacturers by proper lens design and optimization of the production procedure.

The impact of specimen-induced aberrations is usually not well predictable. For certain geometrical shapes of the aberration source, such as the cover plate where a specimen is mounted, the effect can be mathematically described. The impact on imaging can be ex-

pressed again by the Zernike coefficients in the same way as in system-induced aberrations. A planar phase object is known to induce mainly spherical aberrations. However, when imaging into an inhomogeneous or time varying medium, resulting aberrations are unknown and sometimes change dynamically. In that case, the distorted wavefront has to be measured constantly and compensated with adaptive optics. Usually, it is recommended to eliminate strong aberrations before the use of improving imaging techniques. This will be the topic of the next subchapters.

### 1.4. Resolution in microscopy

So far, imaging resolution was discussed based on the optical resolution of a single imaging lens. In microscopy this corresponds to the microscope objective (MO). However, the final picture is a combination of the resolutions of the different imaging parts. The basic scheme of a simple microscope is shown in *figure 6*. It consists of an illumination part, object or sample, the imaging optics including the MO and the detector. Every part influences the resolution of the final image.

The lens resolution (*eq. 1*) is only valid if the illumination has the same opening angle and medium refractive index as the imaging lens. The  $2^*\text{NA}$  term is, in fact, the sum of the two numerical apertures. A crucial part is the detector, which has to be able to sample the image resolution with an appropriate spatial resolution according to the minimal required Nyquist frequency. Finally, the image of the microscope has to be displayed suitably to be able to see the tiniest features. Nowadays, the determining part is the resolution of the microscope objective, as cameras, computers and displays with very high resolution are readily available.

By changing the wavelength, acceptance angle or refractive medium of the microscope objective the spatial resolution is optimized (*eq. 1*). With a shorter wavelength giving a smaller PSF size the resolution becomes better. Ultra-violet instead of visible light increases the resolution by a factor of two. Increasing the acceptance angle has a physical limitation given by the sine value of 1 corresponding to a  $90^\circ$  angle. To collect light from larger angles, therefore, is only possible with a 4- $\pi$  microscope [4], which collects the light of the object from two sides with two equal microscope objectives. This increases the resolution by another factor of

two. Furthermore, the use of oil-immersion objectives is a common technique to reach the maximum resolution of a given optical system. Matching the oil with the refractive index of the objective's material can reduce specimen-induced aberrations as a welcome side effect.

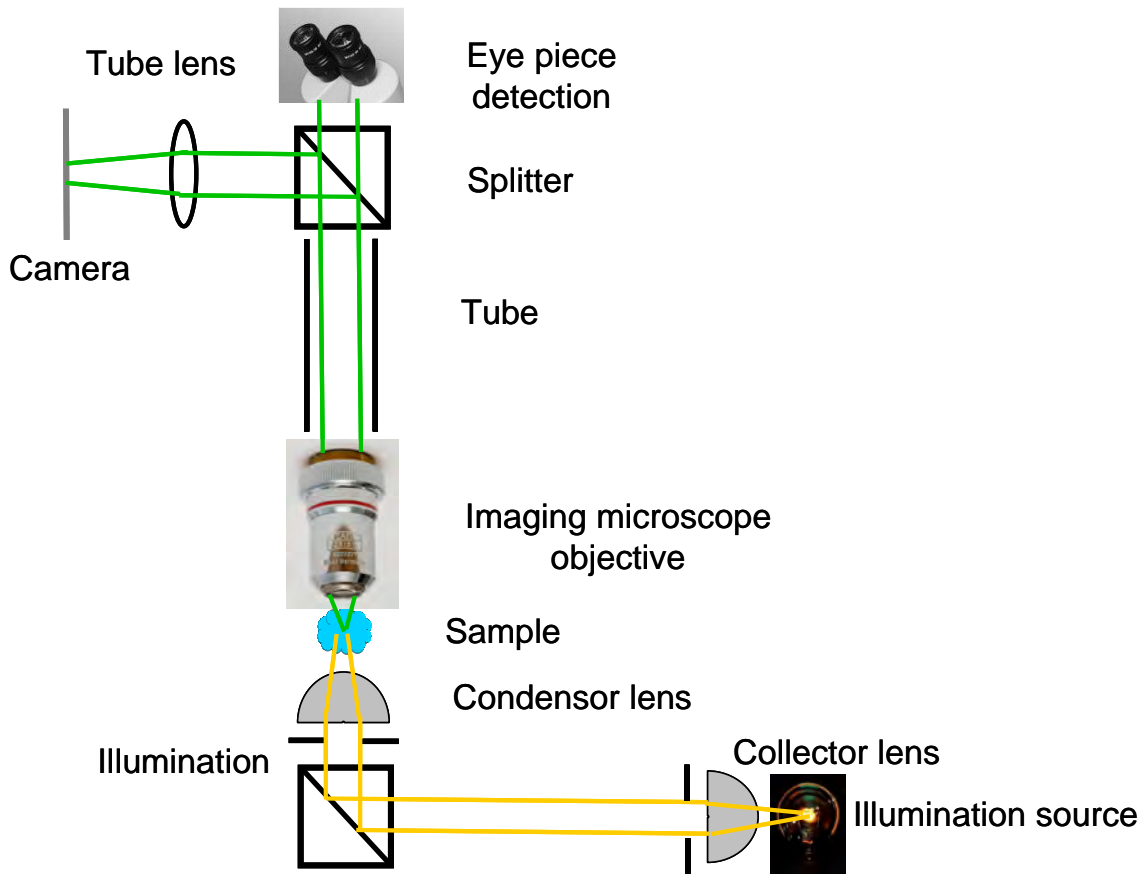


*Figure 6: Basic scheme of a microscope with its main parts: illumination, sample, imaging optics and detection.*

There are two main methods to measure the resolution of a given optical system experimentally. First, the PSF can be measured directly by imaging a bead, which has to be smaller than the resolution limit. The bead can be viewed as a point source, which gets convolved with the system's PSF.

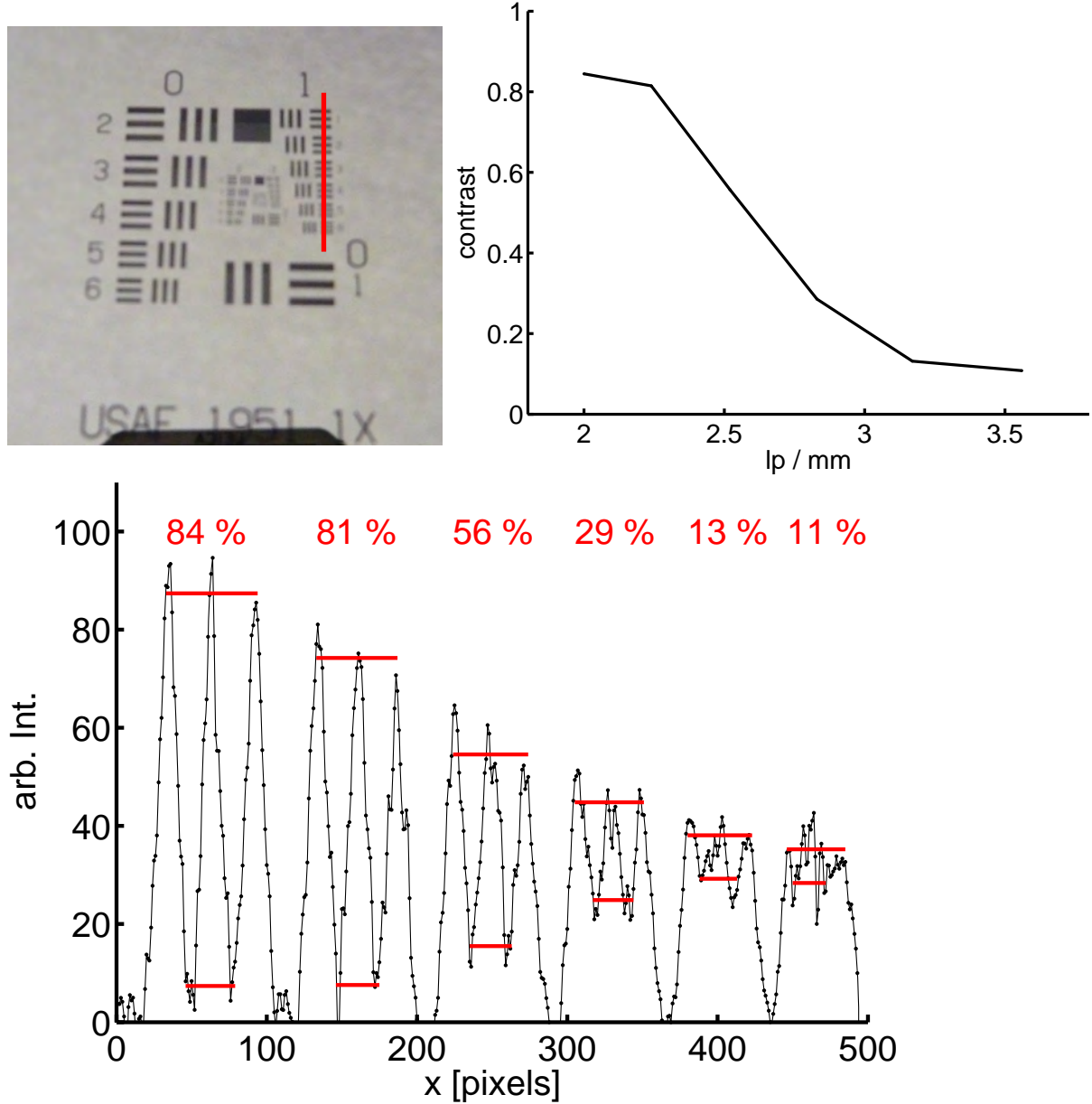


*Figure 7: Top left: Transparent USAF 1951 target for resolution calibration. Bottom: Intensity profile at the indicated line to visualize the contrast. Top right: MTF of the imaging system.*

Second, the resolution can be measured using an imaging test target, for example, the US air force target USAF 1951 (fig. 7 top left). The target has triple line-pairs, which differ in size. The contrast of the lines represents the ability to resolve them (eq. 5).

$$\text{Contrast} = \frac{I_{\max} - I_{\min}}{I_{\max} + I_{\min}} \quad (5)$$

If the lines are wide enough, a good contrast with almost 100% can be reached (*fig. 7 bottom*). In the test target, the contrast, however, decreases constantly with decreasing size of the lines until it reaches zero for non-resolved line pairs. The resolution can be calculated using the group and element number of the last resolved line pair (*eq. 6*).

$$\text{Res} = 2^{\text{group} + (\text{element}-1)/6} [\text{lp / mm}] \quad (6)$$

A graph, which consists of the contrast depending on the size of the line pairs, can provide the modulation transfer function (MTF). The MTF is a measure taken in the frequency domain (*fig. 7 top right*), whereas the PSF is taken in the spatial domain. A Fourier transformation relates them to each other.

### 1.5. Imaging techniques in microscopy

Other measures next to resolution are also important to describe the performance of an imaging system. The image quality depends on the contrast of the object compared to the background or other objects not under investigation. If the contrast, for example, is very weak, an increase in resolution will usually not result in a better image. A highly resolved picture with poor contrast still results in a poor image. Different reasons can lead to a weak contrast.

If the object under investigation is transparent and only differs from the surrounding by its refractive index, it will not be visible in standard bright-field microscopy. The light passes through the object and the contrast is zero. To extract the tiny deviations in optical density of transparent objects, dark field, phase contrast and differential interference contrast (DIC) techniques were invented. They share the main idea to separate the illumination light into two beams, which travel differently through the same object. As the optical density changes slightly within one path, they get a phase difference, which can be visualised by interference [1]. The resulting contrast difference is based on the optical thickness difference  $d_{\text{opt}}$  depending on the physical thickness  $d_{\text{phys}}$  and the optical density  $n$  (refractive index) of the object (*eq. 7*). Using these methods, the contours or interfaces of different materials can be imaged.

$$d_{\text{opt}} = d_{\text{phys}} \cdot n \quad (7)$$

Light originating from regions out-of-focus can be another reason for obtaining a low contrast. In this case, the axial resolution has a different impact than the transversal resolution on the resulting image quality. Every point within the object plane is sharp, whereas the image gets more blurry from objects further away from the resolved axial region. Observing weak phase objects, which are axially close to more intense objects results in a low image contrast, because the bright but blurry image of the unwanted object adds a high background. From the known axial light intensity distribution for every image point, it is possible to remove the blurry overlaying images by deconvolution. In order to do so, it is necessary to take a full stack of images focused at sequential  $z$  positions. The deconvolution algorithm can detect the correct axial region of every object and remove the images from the other positions. The objects are only presented in the sharpest plane, which corresponds to different depths. This increases the axial resolution and also the contrast. It is important to perform the deconvolution with care. Usually, real samples with many objects close to each other and at different  $z$  positions are very difficult to recreate. Wrong reconstruction results and artefacts can corrupt the image and, thus, lead to false interpretations.

With a z-stack of images, a full three-dimensional representation of an object can be generated. This process is supported by confocal microscopy, which optically improves the contrast by selecting only a small axial and lateral region [5]. As the light from the “wrong” axial plane travels with a slightly shifted angle through the confocal microscope, a pinhole at an intermediate image plane cancels them out. The axial resolution in confocal microscopy is, therefore, limited by the size of the aperture, while the transversal resolution remains unchanged. With decreasing pinhole size the transmitted light irradiance is decreasing, which impacts on contrast and requires high detector sensitivity. Furthermore, the image acquisition time is elongated, because the whole sample has to be scanned in three dimensions.

### 1.6. Superresolution in microscopy

We have seen that the optical resolution of an imaging system is limited by diffraction. However, this limit is not fundamental. This finding has led to investigations in superresolution (sub-diffraction) microscopy. The most established techniques are hereafter briefly discussed.

An elegant method to overcome the resolution limit is performed by scanning near-field optical microscopy (SNOM). In SNOM, the illumination or the detection is performed with a glass fibre, whose aperture tip has a scale of only a few nanometres. Therefore, light is physically collected only within a region much smaller than the diffraction limit. The resolution limit of a modern SNOM is in the range of single-digit nanometres. The main limitations of SNOM are the very low light efficiency, the scanning time and the close distance of the tip to the surface.

A different milestone in the development of microscopy is the use of fluorescence. Fluorescence is produced, when light with high-energy is absorbed and subsequently re-emitted at a lower frequency, i.e. at a different colour. In fluorescence microscopy, the illumination light is filtered out and only the fluorescence light generates the image. For biological samples, researchers chemically attach fluorescent molecules or beads to a structure of their object. In this case, a very specific object feature, for example, the cytoskeleton within a cell, can be examined without the distortions of the surrounding environment.

A further method reduces the transversal spot size. This is used, for example, in stimulated emission depletion (STED) [6]. STED is a scanning fluorescence microscopy technique, where a doughnut shaped laser beam is overlaid over the excitation beam as in a pump and probe method. The fluorescence bead is quenched and cannot get excited within this ring-shaped beam. Its transmission gets inhibited and gives no rise to the image. By controlling the intensity of the quenching beam, the active middle region can be adjusted to a much smaller size than the actual diffraction limit due to non-linear effects. The total PSF size is finally smaller and the resolution is increased.

Other common superresolution techniques use fluorescence beads as objects. Every bead gives one transversal PSF in the image plane. By imaging only one bead at the time, there is no overlap between the PSFs. A precise localization of each single fluorescence bead is possible and, therefore, reaching resolutions of a fraction of the diffraction limit depending on the detector sensitivity and localization algorithms. In this case, the real imaging resolution is not changed, as every bead is still imaged blurry with a size of around 250 nm. However, being able to localize their centre very precisely, an image with far better resolution is constructed. Examples of techniques, which use fluorescence beads for superresolution, are photo-

activated localization microscopy (PALM) [7] or stochastic optical reconstruction microscopy (STORM) [8].

The mentioned techniques using structured illumination or precise bead localization can improve the resolution to around 10 nm. The main drawback, however, lies in the elongated acquisition time. In the former, the sample has to be illuminated with different patterns and in the latter, the beads have to be localized in space one after another. Furthermore, sensitive biological samples may get destroyed by the strong illumination light, which is needed for the method.

### **1.7. Adaptive optics**

Adaptive optics was introduced in optical astronomy to correct aberrations arising from fluctuating atmospheric distortions while observing the stars. While telescopes use large lenses and, therefore, large devices, these needed to be miniaturized to make the technique applicable to microscopy. Technical devices with suitable size for microscopy, such as deformable mirrors or liquid crystal displays, have only recently been developed. Since then, adaptive optics evolved rapidly in microscopy [9] with the aim to correct aberrations from changing or fluctuating surroundings, such as immersion media, glass cover slides, cell environment or to image deep into thick specimens. Adaptive optics is of great value for correcting aberrations in microscopy, because aberrations become more severe for higher numerical apertures of an imaging system.

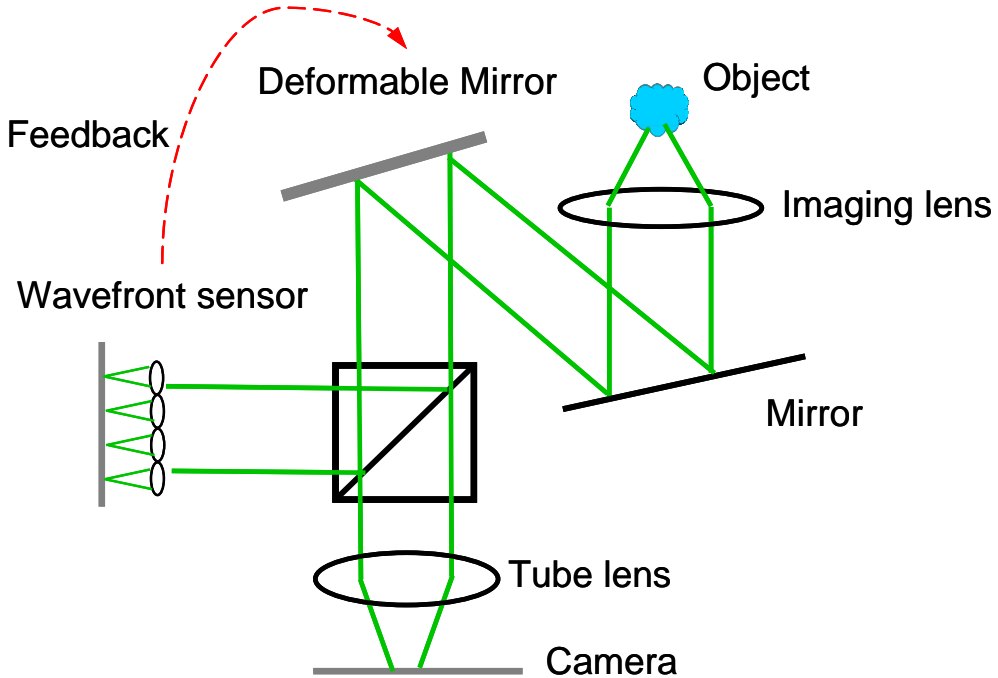


*Fig. 8: Schematic adaptive feedback loop to reduce aberrations in a microscope by measuring the distorted wavefront with a Shack-Hartmann sensor.*

Standard adaptive optics uses a feedback loop consisting of a wavefront sensor and an active wavefront modulator to correct aberrations (fig. 8). During active performance, the feedback system alters the wavefront to optimize the signal on the sensor in a closed loop. Closed loops are needed for rapidly changing aberrations, while static aberrations can be efficiently reduced with open loops. There is also the possibility to measure the specimen surrounding with an independent system and then use the obtained information to correct the induced aberrations without a wavefront sensor integrated in the imaging system. However, changing the optical system may entail serious problems, for example, if the sample itself or its environment varies during that process. Techniques to measure the refractive index and the thickness of a planar transparent medium are discussed in detail in *chapter 4*.

## 1.8. Pupil filter

Pupil filter is the comprehensive term for modulating the light in the pupil plane of imaging and focusing systems (fig. 9). Pupil filters shape the PSF of the lens according to the demands of the application. They were invented by Toraldo di Francia (in 1952) to improve the resolu-

tion in imaging with binary annular amplitude pupil filters [10]. He showed that the classical diffraction limit is not strict. The resolving power of a lens can be theoretically increased to infinity, limited by the amount of light that can pass the filter.

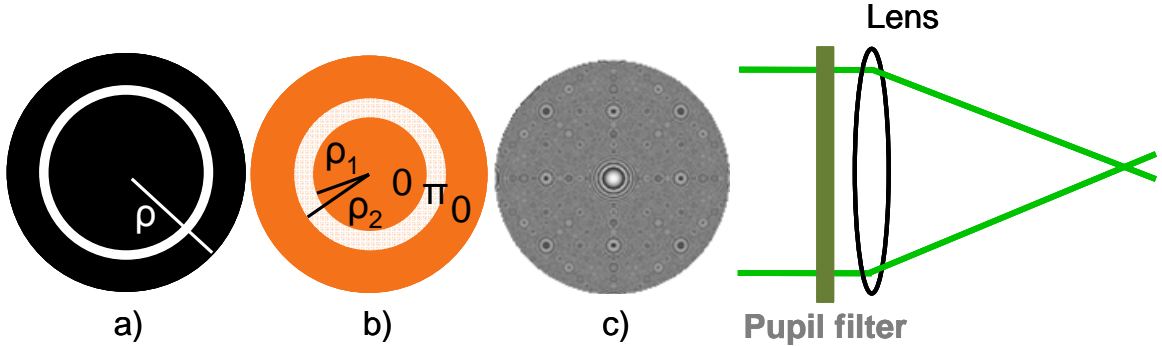


*Fig. 9: Basic scheme of pupil filter modulation at the lens plane with three exemplary functions: a) annular amplitude, b) three-zone phase and c) diffractive modulation.*

Meanwhile, different kinds of pupil filters exist, which can be divided into three main types: amplitude, phase, and complex pupil filters. To simulate numerically the performance of pupil filters, the intensity distribution near the focus of a lens can be calculated using the Huygens-Fresnel diffraction integral (see *chapter 2.2*). Amplitude pupil filters are blocking or attenuating the light across the lens plane. Phase pupil filters on the other hand transmit all the light but introduce a spatial phase modulation. To obtain a complex modulation, two consecutive modulators have to be applied for the amplitude and phase, respectively. Most popular are binary amplitude or phase functions, as they are quite simple to implement, and their resulting intensity distribution near the focus can be analytically solved due to the simple design. However, there are many different designs with continuous, diffractive, asymmetric and more exotic modulation, both in amplitude and phase.

The technical implementation of pupil filters strongly depends on their type and application. Binary amplitude filters are nothing more than a transmission mask, which can be produced with different methods easily, for example lithography. For intermediate gray-levels, there exist micro-mirror-arrays that tilt individual mirrors at a certain frequency. A spatial modulation is achieved from the average time that the “mirror-pixel” is upright. Liquid crystal devices are suitable to generate continuous amplitude or phase modulation. Different types are on the market as helix shaped twisted-nematic liquid crystal devices and liquid crystals on

silica. For pure phase modulation, there also exist deformable mirrors, where the relative phase change is induced by a spatial deformation of the mirror surface. Complex pupil filters are more complicated, as they require a set of two consecutive modulators with proper alignment of every pixel. Our choice of phase modulator based on their characteristics and advantages is discussed in *chapter 2.3.1*.

As diverse the designs are, as different are the achieved results of the modulated lens systems. Already mentioned is the task of narrowing the PSF, obtaining a superresolution effect. However, superresolution performed with pupil filters is very limited represented by an efficiency factor of  $G^{-6}$  [11], where  $G$  is the target transversal gain factor. An effective and successfully used technique is optical trapping, where the incoming light is redistributed to focus into a specific pattern that can generate enough force to trap small objects. With a set of multiple focus points, several objects can be trapped and even moved separately by adaptively changing the illumination pattern [12]. Other pupil filter designs can generate pseudo non-diffractive beams or extend the depth of field to improve the output from imaging or focusing applications (see *chapter 3.3.1*).

# Chapter 2

## Materials & Methods

### 2.1. Overview

This chapter summarizes the methods used to obtain the results for the simulations and the experiments. To complete the tasks mentioned in *chapter 1*, we developed a simulation tool in MATLAB and two optical systems. The simulation tool calculates the Huygens diffraction integral in Fresnel approximation to obtain the light intensity near the focus of focusing or imaging lenses (*chapter 2.2*). Although it is valid for paraxial rays, it proved to generate valuable results for numerical apertures up to 0.7 (typically a 40x or 60x microscope objective). Using the MATLAB tool, any lens design including variable modulations in the lens plane (pupil filter) can be evaluated. A complete three-dimensional analysis of the focused spot shape in lateral and longitudinal direction was performed for various designs. This provided a complete point spread function (PSF), which was characterized with different figures of merit (*chapter 2.3*).

A PSF measuring system was built to experimentally validate the simulated data (*chapter 2.4*). The main idea was to magnify the focal spot of the lens system on to a camera. By scanning through the focal region, a complete three-dimensional analysis could be done and directly compared to the simulations. With the help of an adaptively changeable phase modulator based on a liquid crystal array, phase pupil filters could be examined in the experiment.

Finally, a model microscope including the adaptively changeable phase modulator was assembled (chapter 5). It allowed evaluating the full imaging performance of the different phase modulation designs. By imaging through glass plates, a planar refractive index mismatch was created.

## 2.2. PSF calculation

As first step, we investigated in the derivation of the Kirchhoff diffraction integral to calculate the light intensity distribution of a focusing lens within the scalar diffraction theory. This formula is valid for any polarization of the propagating light beam, which represents our experimental case. As we are interested in the focusing properties of lenses, the lens equation is evaluated and included. During the process of reformulating and simplifying the equations, many approximations were applied and will be discussed in *chapter 2.2.3*. A short discussion about their impact on the calculation accuracy is important. Finally, the implementation and optimization of the code in MATLAB is discussed.

### 2.2.1. Scalar diffraction theory

The scalar diffraction theory was applied to simulate the light intensity distribution near the focus. This means, the fundamental vectorial nature of light with its electromagnetic fields and the time behaviour were neglected. We start discussing the formulations from the point where the determining and restrictive approximations were applied to obtain a simplified equation. The scalar diffraction theory arising from the Maxwell's equations have already been intensively studied and are not further investigated in this work.

We start our calculations from the scalar superposition integral by Rayleigh-Sommerfeld (*eq. 8*), which directly arises from the optical Maxwell equations in combination with Greens theorem [13] and the Huygens-Fresnel Principle [14].

$$U(P_0) = \frac{1}{i\lambda} \iint_{ap} U(P_1) \cdot \frac{e^{ikr_{01}}}{r_{01}} \cdot \cos\theta ds \quad (8)$$

The field  $U$  in a point  $P_0$  in the image space consists of the superposition of the spherical waves from all points  $P_1$  in the pupil plane with phase delays that depend on the travelled path length  $r_{01}$  (fig. 10).

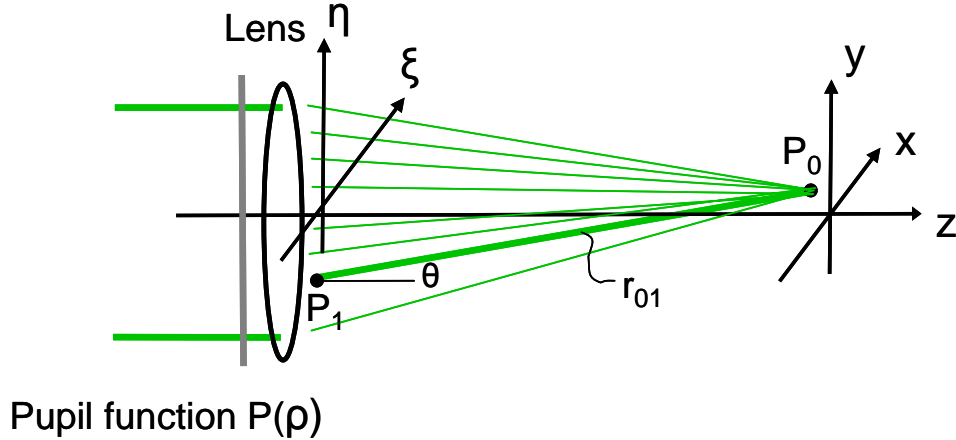


Figure 10: Huygens-Fresnel superposition principle.

Here,  $\lambda$  is the wavelength,  $k = 2\pi/\lambda$  is the wave number,  $r_{01}$  is the distance between the points  $P_0$  and  $P_1$  and  $\theta$  is the angle with the optical axis. The superposition principle states, that the field amplitude  $U$  in the image space at point  $P_0$  can be calculated by superposing the amplitude with its corresponding propagation term for each point  $P_1$  of the aperture. The Rayleigh-Sommerfeld solution requires that the diffraction screen (aperture) is approximately planar.

Replacing the cosine by the exact geometrical transformation,  $\cos \theta = z/r_{01}$ , and expressing the aperture plane in  $\xi\eta$ - and the image plane in  $xy$ -coordinates leads to

$$U(x, y, z) = \frac{z}{i\lambda} \iint_{ap} U(\xi, \eta) \cdot \frac{e^{ikr_{01}}}{r_{01}^2} d\xi d\eta \quad (9)$$

with the distance  $r_{01}$  given by

$$r_{01} = \sqrt{z^2 + (x - \xi)^2 + (y - \eta)^2} \quad (10)$$

Equation 9 is considered exact as long as the scalar diffraction approximation is valid (see chapter 2.2.3). However, analytical solutions only exist for simple geometries. To simplify the calculation, the Fresnel approximation uses a second order Taylor series expansion of the square root (eq. 11).

$$r_{01} \approx z \cdot \left( 1 + \frac{(x-\xi)^2}{2z^2} + \frac{(y-\eta)^2}{2z^2} \right) \quad (11)$$

For the  $r_{01}$  term in the denominator, the first order approximation is sufficient, while the exponential term needs the second order to be accurate enough. This leads to the Fresnel equation that is valid for any kind of planar aperture:

$$U(x, y, z) = \frac{e^{ikz}}{i\lambda z} \int_{-\infty}^{\infty} \int U(\xi, \eta) \cdot e^{\frac{ik}{2z}((x-\xi)^2 + (y-\eta)^2)} d\xi d\eta \quad (12)$$

Since in imaging and focusing applications circular symmetric apertures are used, we can rewrite the Fourier like equation. Applying a zero order Hankel transform [15, 16], *equation 13* is obtained for calculating the intensity distribution near the focus without further approximations.

$$I(r, z) = \left\{ \frac{k}{z} \int_0^{\rho_{\max}} F(\rho) \cdot e^{\frac{i k \rho^2}{2z}} \cdot J_0\left(\frac{k}{z} \rho r\right) \cdot \rho \cdot d\rho \right\}^2 \quad (13)$$

The  $xy$  and  $\xi\eta$  coordinates were transformed to the radial coordinates  $r$  and  $\rho$ , respectively. The circular symmetric pupil plane has an aperture  $\rho_{\max}$  and  $J_0$  is the Bessel-function of the first kind arising from the Hankel transform. The initial field  $U(\xi, \eta)$  was transformed to the pupil function  $F(\rho)$ .

### 2.2.2. Lens function

For a spherical lens without any further aperture function, the pupil function is a pure phase factor dependent on the lens thickness. *Figure 11* shows a scheme for the lens thickness and definition of the distances.  $OA$  is the optical axis,  $R_1$  and  $R_2$  are the front and back radii of the lens,  $\Delta_i$  are the maximal lens thicknesses,  $t_i$  are the lens thicknesses at radial distance  $\rho$  and  $n$  is the refractive index of the corresponding medium [17].

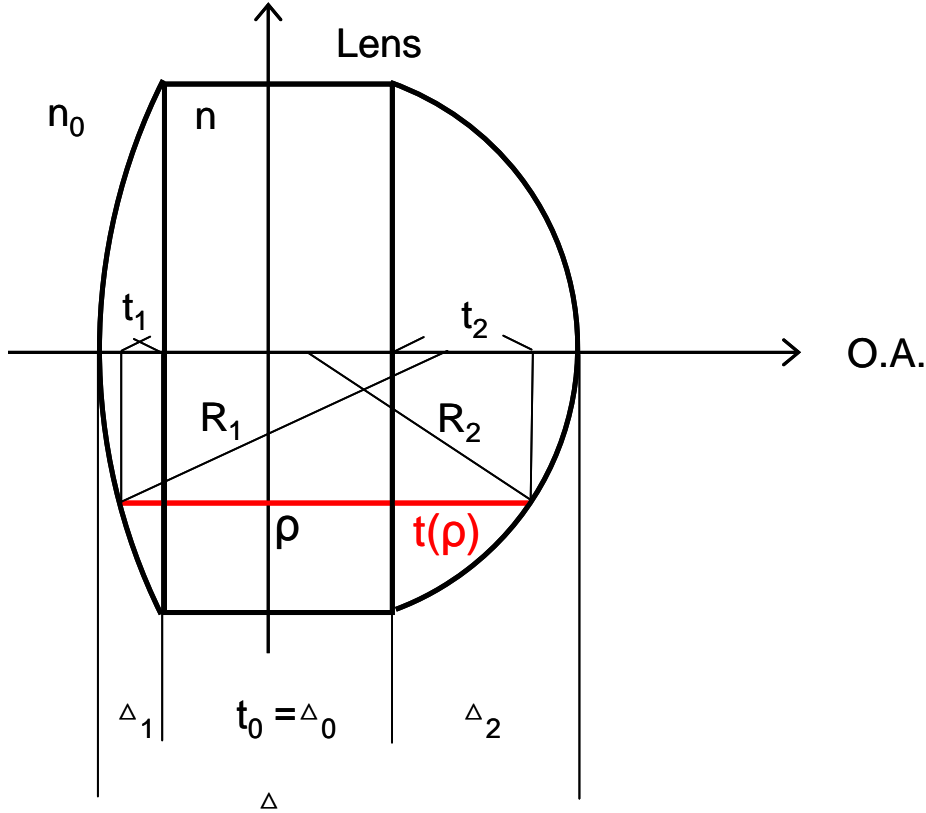


Figure 11: scheme for calculating the phase function for a simple lens (parameters described in the text).

The total lens thickness  $t$  at position  $\rho$  is

$$t(\rho) = t_1 + t_o + t_2 \quad (14)$$

The partial thicknesses  $t_i$  can be calculated geometrically from the lens radii  $R_i$  and  $\rho$ . By convention, the front and back focal radii have opposite signs.

$$t_i = \Delta_i - \left( R_i - \sqrt{R_i^2 - \rho^2} \right) \quad (15)$$

Applying a first order approximation of the square root with a Taylor series (*eq. 16*) yields *equation 17*.

$$\rho \ll R_i \rightarrow \sqrt{R_i^2 - \rho^2} \approx R_i \left( 1 - \frac{\rho^2}{2R_i^2} \right) \quad (16)$$

## 2. Materials and Methods

---

$$t(\rho) = \Delta_1 - \frac{\rho^2}{2R_1} + \Delta_o + \Delta_2 + \frac{\rho^2}{2R_2} = \Delta - \frac{\rho^2}{2} \left( \frac{1}{R_1} - \frac{1}{R_2} \right) \quad (17)$$

The next conversion with the help of the thin lens equation (*eq. 18*) and the relation between the phase  $\varphi$  and the physical thickness  $t$  (*eq. 19*) yields the final phase function  $\varphi_{lens}$  for a thin lens with approximated thickness  $\Delta=0$  (*eq. 20*).

$$\frac{1}{f} = (n - n_0) \left( \frac{1}{R_1} - \frac{1}{R_2} \right) \quad (18)$$

$$\varphi(\rho) = k \cdot (n - n_0) \cdot t(\rho) \quad (19)$$

$$\varphi_{lens}(\rho) = -\frac{k\rho^2}{2f} \quad (20)$$

The pupil function  $F(\rho)$  from *equation 13* can be split into two parts (*eq. 21*), an exponential phase term for the lens and an amplitude pupil filter  $P(\rho)$  or aperture.

$$F(\rho) = P(\rho) \cdot e^{i\varphi_{lens}(\rho)} \quad (21)$$

The final equation for the simulation of the light intensity near the lens focus is obtained.

$$I(r, z) = \left\{ \frac{k}{z} \int_0^{\rho_{\max}} P(\rho) \cdot e^{-i\frac{k\rho^2}{2f}} \cdot e^{i\frac{k\rho^2}{2z}} \cdot J_0\left(\frac{k}{z}\rho r\right) \cdot \rho \cdot d\rho \right\}^2 \quad (22)$$

The pupil filter term  $P(\rho)$  is now independent of the lens term. This is important to memorize, as in the following parts, the pupil filter will always be the additional phase or amplitude modulation on top of the used lens. In summary, the first exponential function containing the focal length  $f$  describes the focusing of the lens, the second exponential function the propagation to distance  $z$ . The Bessel function provides information on the transversal behaviour and  $\rho$  is derived from a cylindrical coordinate transformation.

For 2D calculations, the equation can be simplified. Calculating the transversal light intensity distribution at a certain distance  $z_{tr}$ , the exponential propagation term becomes constant

and can be taken out of the integral (*eq.* 23). In case of on-axis calculation, the transversal distance  $r$  is zero and therefore the Bessel term is 1 (*eq.* 24).

$$I(r, z_{tr}) = \left\{ \frac{k}{z_{tr}} \int_0^{\rho_{\max}} P(\rho) \cdot e^{-i \frac{k\rho^2}{2f}} \cdot e^{i \frac{k\rho^2}{2z_{tr}}} \cdot J_0\left(\frac{k}{z_i} \rho r\right) \cdot \rho \cdot d\rho \right\}^2 \quad (23)$$

$$I(0, z) = \left\{ \frac{k}{z} \int_0^{\rho_{\max}} P(\rho) \cdot e^{-i \frac{k\rho^2}{2f}} \cdot e^{i \frac{k\rho^2}{2z}} \cdot \rho \cdot d\rho \right\}^2 \quad (24)$$

### 2.2.3. Error estimation of the used approximations

The approximations made to obtain *equation* 22 for calculating the light intensity distribution of a focusing lens are listed in *table 2*. Restrictions and consequences of violation for each of them are discussed consecutively.

**Table 2:** Approximations used in the simulation.

Source	Approximation	Description
scalar diffraction	$\rho_{\max}, t_{\text{pupil}} \gg \lambda$	Diffraction structure larger than the light wave
far field	$r_{01} \gg \lambda$	Observation plane is far from the lens
thin lens	$\Delta \ll R_i$	Lens thickness is much smaller than lens radii
small angles	$\rho_{\max} \ll 2f$	For small NA: $\sin \theta = \rho / 2f$
Fresnel	$(x - \xi)^2 \ll z^2$	Binomial expansion of square root
axial depth	$w = z - f \ll f$	Only valid near the focal position
paraxial	$x, y, \rho \ll R_i$	Only valid near the optical axis

## 2. Materials and Methods

---

The scalar diffraction theory [18] requires that the aperture radius  $\rho_{max}$  and the thickness of the diffraction structures  $t_{pupil}$  in the pupil plane are much larger than the wavelength  $\lambda$ . As far field requirement, the observation of the diffraction field must be far from the aperture ( $z \gg \lambda$ ). These requirements are fulfilled for the lenses used in this work. The diffraction aperture radius is around 5-10 mm while the diffraction structures are several  $\mu\text{m}$  large; both are much larger than the wavelength of the visible light with a median size of 500 nm. The observation plane lies around the lens focus at a range of several mm, much further away than a wavelength as required from the far field approximation. Close to aperture calculations are not performed in this work and near-field diffraction calculations not needed therefore.

The lens equation is obtained by applying the thin lens approximation. In that case, the lens plane and the pupil plane are equal. The additional aperture or pupil filter function  $P(\rho)$  is applied on approximately the same plane. Therefore, the experimental results can vary slightly from the numerical simulations, as the combined total lenses have a physical thickness. In the experiment, the pupil filter phase modulation should be applied as close to the lens as possible to guarantee good results.

According to the small angles approximation, the accuracy of calculations for high numerical apertures (NA) systems is limited. Investigations in the usefulness of the simulations for high NA systems were already performed [15, 19]. The results for high NA lead to quantitative similar light intensity distributions as for low NA. The calculations are widely accepted to be correct for NAs up to 0.7. In our work, we have lenses with numerical apertures below 0.3.

The paraxial, axial depth, and Fresnel approximations limit the numerical investigations to regions close to the focal point, thus the axial distance from the focal length and the transversal distance from the optical axis have to be small. This inhibits numerical investigations of intermediate planes or image points far away from the focal point. In focusing applications, this limitation is insignificant because the light is always focused at the focal spot. It becomes more crucial in imaging applications where points further away from the optical axis are also of interest. In that case, the simulations are only valid for on-axis imaging, while the off-axis imaging characteristics need to be examined in the experiment.

### 2.2.4. Simulation tool / implementation into MATLAB

To simulate the light intensity distribution of a focusing lens, *equation 22* has to be implemented. This was done with the MATLAB software from MathWorks. As the integral has no analytical solution, the symbolic function INT (integration) and the function handle integration ODE (ordinary differential equation) are not able to solve the problem. Therefore, a numerical evaluation is needed.

The cylindrical coordinates  $r$  and  $z$  and the aperture radius  $\rho$  as integration variable are the three independent variables to obtain the light intensity (*eq. 22*). This requests three convoluted FOR loops to add the terms together. The QUAD function of Matlab is based on adaptive Simpson quadrature, but when used to evaluate numerically the integral wrapped in three convoluted FOR loops, it is very slow.

An improvement is offered by the TRAPZ function, a trapezoidal numerical integration. Although this gave some speed enhancement by avoiding adaptive procedures, there were still three loops needed to solve the full integral. Therefore, we used the CUMTRAPZ function, a cumulative trapezoidal numerical integration to avoid one loop. Since Matlab is computed and optimized for vector and matrix calculations, the cumulative integration works at least one order of magnitude faster than an equal solution with FOR loops. In the 2D case of axial (*eq. 23*) or transversal (*eq. 24*) calculation, a matrix is built up from the matrix product of the pupil radius  $\rho$  and the transpose of the axial length  $z$  or the transverse distance  $r$ , respectively. This reduces another loop in the calculation of the integral. The cumulative integral CUMTRAPZ therefore calculates the integral of the matrix without any loop in case of 2D calculation. In the 3D case, only one loop for one of the remaining spatial dimension has to be added.

While the program code with 3 loops and only  $60 \times 40 \times 256$  ( $z \times r \times \rho$ ) calculation points took around 20 minutes, the calculation time was reduced to less than 2 minutes with much more calculation points of  $3000 \times 1000 \times 1000$ . That corresponds to an improvement in calculation speed of a factor of 50'000. This dramatic time shortening was achieved by choosing speed-optimized Matlab functions and by profiting of the Matlab specialisation in matrix calculations, replacing time consuming loops.

This calculation core was embedded into a GUI (graphical user interface) with the additional feature of choosing different pupil function designs and their respective parameters (*fig.*

## 2. Materials and Methods

---

12). In that way, any pupil filter design could be evaluated, and the necessary sampling for every dimension was adjusted.

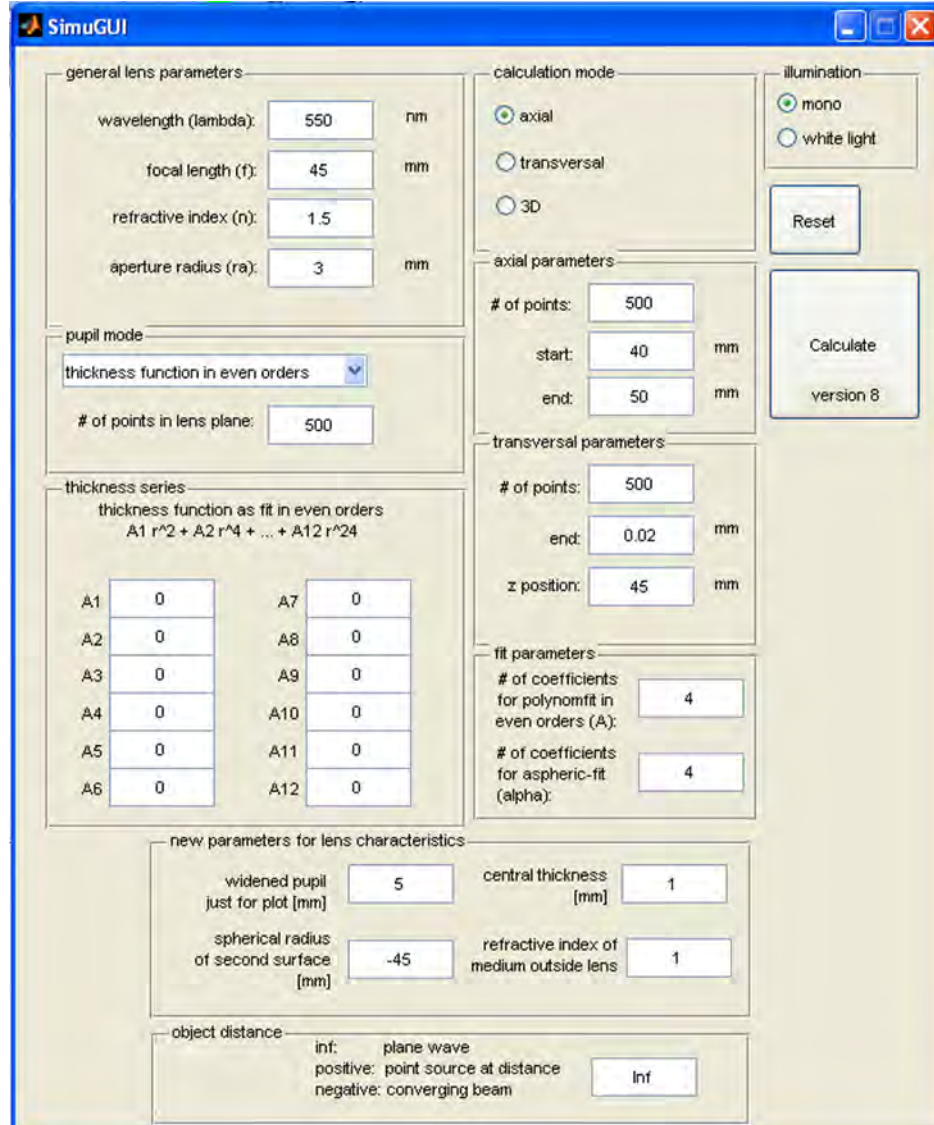


Figure 12: Graphical user interface (GUI) in Matlab for the choice of pupil functions.

### 2.3. Figures of merit

The powerful Matlab tool to calculate any pupil filter design was used to analyze the axial and transversal intensity distribution systematically. To this end we defined figures of merit in axial and transversal direction. They have been applied for both the simulation and the experimental analysis for direct comparison. The different figures of merit are summarized in *table*

## 2. Materials and Methods

---

3 and displayed in *figure 13* and *14*. The usual measures as the Strehl ratio  $S$ , depth of field  $DOF$ , full width at half maximum  $FWHM$  and resolution  $R$  are taken from the literature [20, 21]. We have defined two additional figures of merit, the axial mean intensity within the  $DOF$  and the radiant flux within the first main transversal peak.

**Table 3:** Figures of merit to characterize intensity distributions.

Figure of merit	Direction	Description
$f_{max}$	Axial	Position of the axial peak maximum
Depth of field $DOF$	Axial	Full width at half maximum of axial peak
Strehl ratio $S$	Ax. and Transv.	Maximum intensity compared to reference peak
$I_{mean}$	Axial	Mean intensity within the $DOF$
$FWHM$	Transversal	Full width at half maximum of transversal peak.
Resolution $R$	Transversal	Distance between the first minima.
Radiant flux $W$	Transversal	Radiant flux within main peak compared to the reference lens

The Strehl ratio  $S$  is the ratio of the intensity peak maximum value at the axial peak maximum position  $f_{max}$  and the diffraction limited reference peak maximum. The Strehl ratio is equal for the axial intensity and the transversal intensity in the focal plane. By calculating the transversal intensity distribution at a plane shifted to the focus point, the maximum peak value gets smaller and does not correspond to the Strehl ratio.

The depth of field ( $DOF$ ) is defined as the full width at half maximum of the axial intensity distribution (green points in *fig. 13*). To normalize the axial gain  $G_A$ , the value of the  $DOF$  is divided by the value of the diffraction limited reference  $DOF$ . An axial gain value larger than 1 corresponds to an elongation of the depth of field, while a narrowed depth of field has an axial gain value smaller than 1.

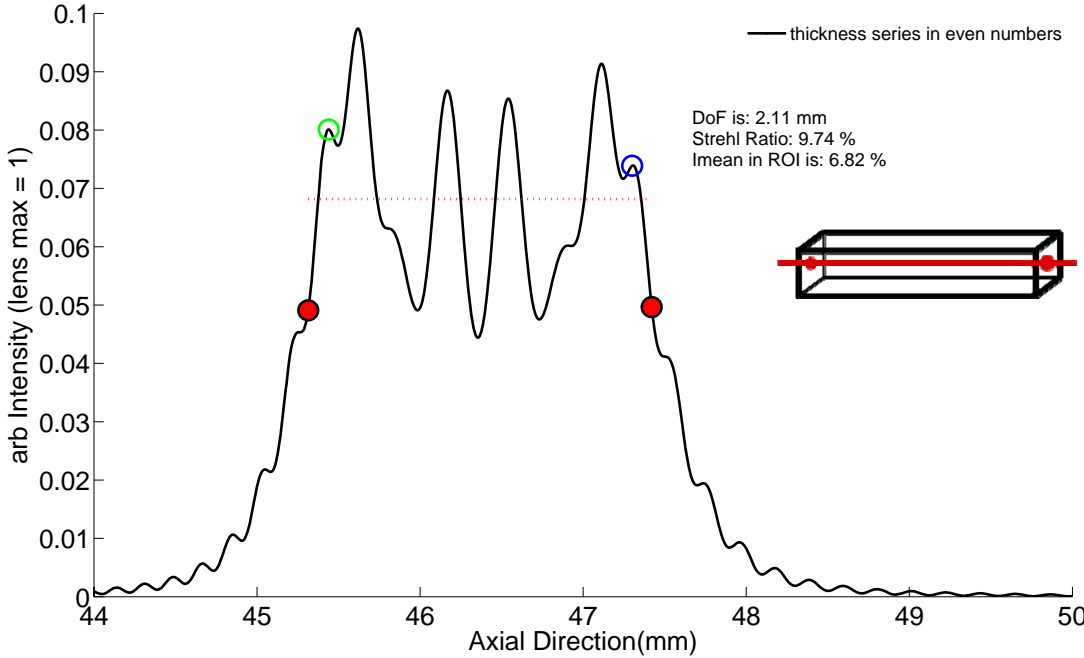


*Fig. 13: Figures of merit for an axial intensity distribution: Strehl ratio  $S$ , depth of field  $DOF$  (red circles), mean intensity  $I_{mean}$  (red dotted line) and close & far foci (green & blue circles).*

$I_{mean}$  is the axial mean intensity value within the  $DOF$  (dotted line in fig. 13). The mean intensity takes into account peaks and valleys inside the  $DOF$  and gives sometimes a better characterization than the Strehl ratio.

In transversal direction, we define three figures of merit. The full width at half maximum  $FWHM$  of the transversal spot and the transversal resolution  $R$  represent the width. The normalized transversal gain  $G_T$  is again the ratio of the actual  $FWHM$  divided by the reference value of the diffraction limited spot. The transversal resolution  $R$  is defined as the distance between the first minima (diamonds in fig. 14). The  $FWHM$  and the resolution  $w$  are in general giving similar relative results. While both values are easily obtained from simulated distributions, the background noise in experimental measurements can hide the side lobes and therefore hinder the evaluation of the resolution.

## 2. Materials and Methods

---

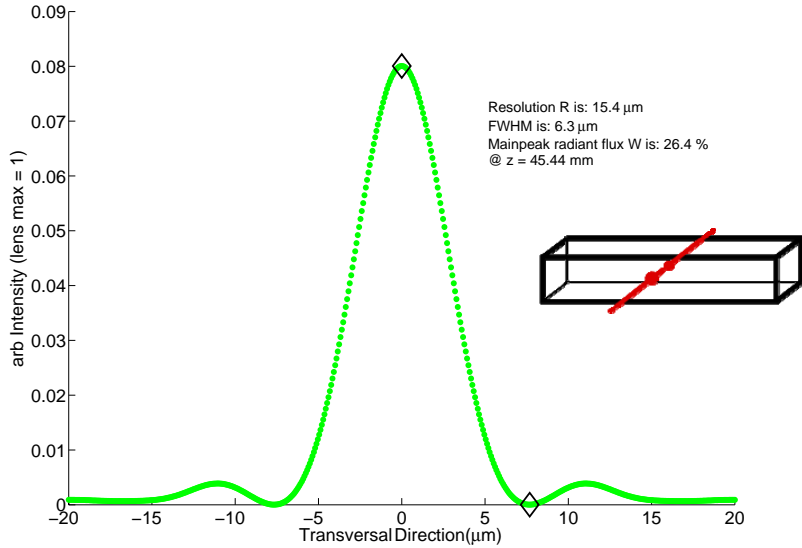


*Fig. 14: Figures of merit output for a transversal intensity distribution: resolution R (diamonds), main peak radiant flux W and FWHM.*

The radiant flux  $W$  is the full 3D intensity content of the transversal central spot, resulting from the lateral integral of the irradiance within the resolution  $w$  (eq. 25).

$$W = \int_0^R 2 \cdot \pi \cdot r \cdot I(r) \ dr \quad (25)$$

The radiant flux value contains combined information on the Strehl ratio and the resolution. As one would expect, the integral of the transversal intensity distribution is higher for broadened distributions and lower for narrowed ones. For intensity distributions with low Strehl values, the radiant flux in the main peak is also low. To check that no light is lost in the simulation of the reference lens or phase only pupil filters, the radiant flux inside a 1 mm disc was calculated and gave more than 95% of the reference at all axial positions. Therefore, for every axial position the light is differently distributed in the transversal direction.

## 2.4. Experimental PSF analysis

The experiments are performed with a home-built PSF measurement system (*fig. 15*) combined with a commercial phase-only spatial light modulator (SLM) [22]. A green laser beam (Nd:YAG Crystalaser, wavelength 532 nm) is expanded and its polarization set along the axis of the reflective liquid crystal SLM (Pluto from Holoeye, 1980x1080 pixels). The reflected beam is passed through a 10x objective (Nikon, Plan Fluor) with NA = 0.3 and infinity correction. Its focal plane is magnified with a 100x objective (Edmund Optics, DIN100, 1.25 Oil) with a much higher numerical aperture of 0.9 onto a CCD camera (Prosilica, 2 Mpix). The complete PSF analyzer is mounted on a translation stage with a step size of 100 nm allowing for a full measurement of the 3D PSF by scanning through the focus. The size calibration of the analyzer was performed with a grating with known spacing.

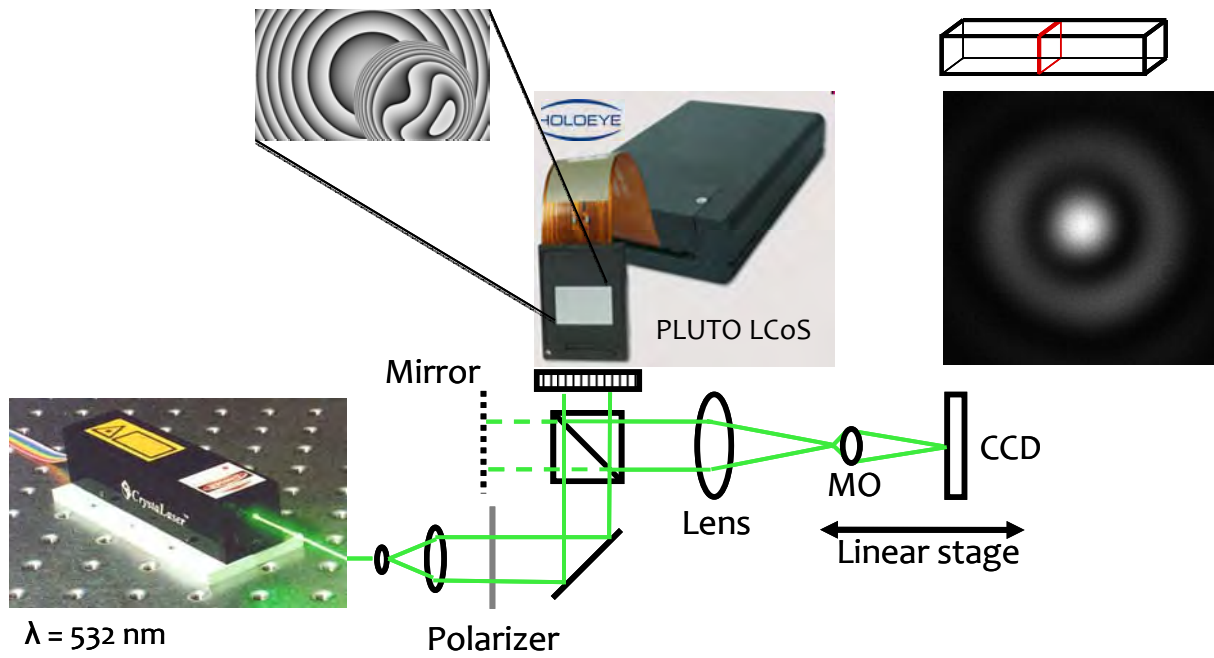


*Figure 15: Basic experimental scheme to measure the PSF of a focusing lens. (LCoS: liquid crystal on silicon, MO: microscope objective, CCD: camera). Left inset: LCoS modulation function containing the flatness correction overlaid with the pupil function; right inset: transversal PSF on the CCD.*

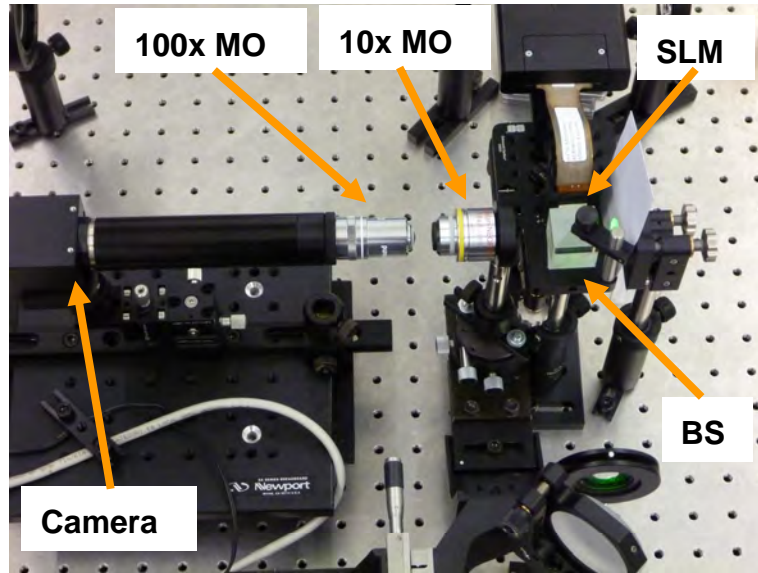


*Photo 1: Experimental setup to measure the PSF of a 10x MO with a 100x MO.*

There are two crucial optical parts that have to be arranged precisely for a proper measurement. The first important thing is that the focusing lens and the analyzer lens are parallel and axially aligned. If not, the peak on the camera would move and eventually leave the detector while scanning in the axial direction. The second and even more sensitive part is the illumination of the focusing lens. If it is illuminated off centre or under an angle, the focusing properties change and aberrations alter the PSF. The measurement cannot be used with an illumination angle above only 2 degrees (*fig. 16*).

This basic experimental setup was modified for the different methods and applications targeted in this work. They all share the use of the phase modulator, which is described and characterized in the following *subchapter 2.4.1*. The study of extended depth of focus (*chap. 3*) needs no further modification to the basic setup. For the characterization of a glass plate and correction of its spherical aberration (*chap. 4*), the plate has to be implemented in between the focusing objective and the analyzer (*chap. 2.4.2*). Finally, the imaging application (*chap. 5*) combines all the previous methods and designs from the focusing application and converts it into an imaging setup with inverted travel direction of the light.

## 2. Materials and Methods

---

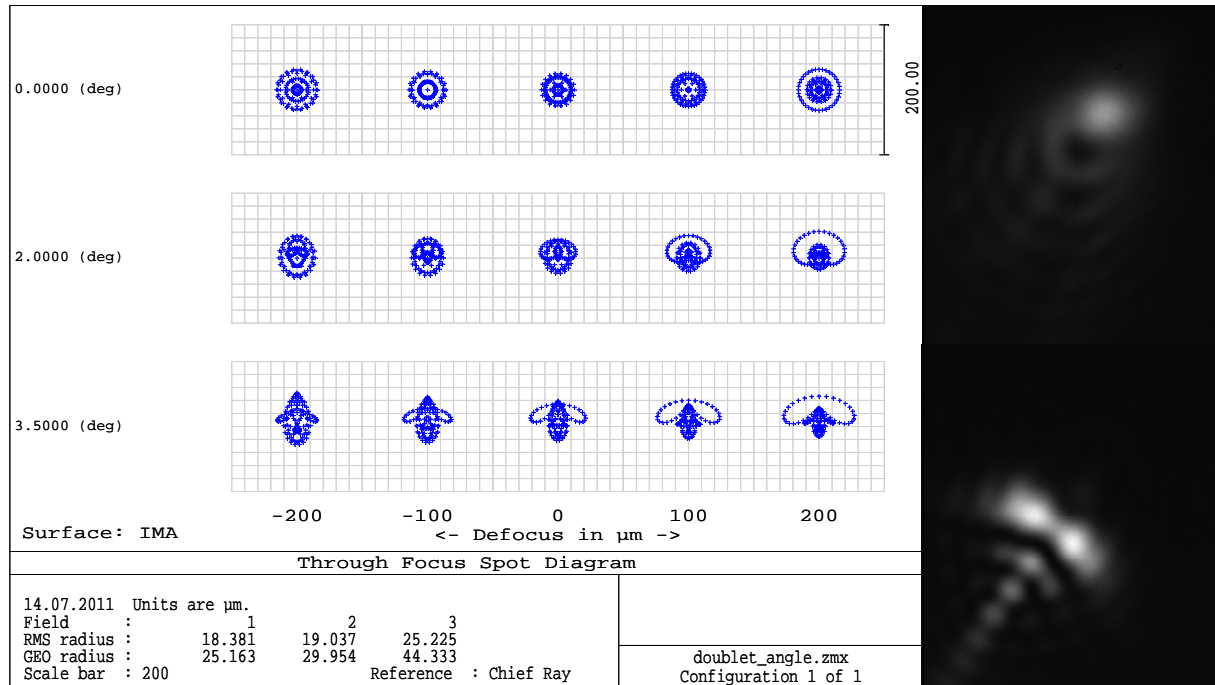


*Fig. 16: Transversal PSF for tilted illumination (left: Zemax simulation, right: 2 measurements with different tilt illuminations)*

### 2.4.1. Phase modulator

Different spatial light modulators are on the market, which usually belong to one of the following types.

#### Deformable mirror

Deformable mirrors are widely used in applications where diffracted light has to be avoided. They induce a phase change by applying a force to the mirror from behind with a small pin, changing the surface contour in a small region. Between the “pixels” is no border and the mirror surface remains continuous. On the other hand, the maximum resolution is rather small with values around 50x50.

#### Twisted-nematic liquid crystal

Tn-LC displays were developed for use in projectors. A pixel consists of a stack of birefringent liquid crystals, each tilted slightly with respect to the previous one. Correctly polarized light passes through and its polarization gets rotated. By applying a voltage to a pixel, all crystals

arrange themselves to a parallel position, inhibiting the change of polarization and changing the effective birefringent axis. This induces a relative phase shift compared to the unmodulated pixel. With a certain range of possible values for the voltage, intermediate shifts can also be generated. With the right adjustment of the polarizer and analyzer, phase or amplitude modulation can be achieved in transmission mode.

However, the main disadvantage lies in the need of elliptically polarized light for proper phase-only modulation, requiring a set of quarter wave plates. This leads to four independent directions to adjust, which makes the setup complicated and quite large. Even with relatively good adjustment for phase-only operation, there usually remains a small amplitude modulation.

### Liquid crystal on silicon (LCoS)

In recent years, liquid crystals on silicon were developed based on the good knowledge of silicon processing, for example for computer chips. The basic principle of modulation is slightly different to tn-LCD. A pixel consists of a birefringent rod-shaped liquid crystal stuck on a highly reflective mirror. In the ground state without applied voltage, all the crystals are in parallel arrangement, and an incoming light beam gets reflected without spatial modulation. By applying a voltage to a pixel, it gets tilted up to 90 degree to the front, depending on the strength of the voltage. A light beam with polarization parallel to the crystal travels therefore longer inside the birefringent crystal along the second axis, inducing a relative phase shift compared to the initial state. The reflective arrangement doubles the effective travel distance. Depending on the used wavelength, the size or the tilt of the liquid crystal has to be adjusted. For phase-only modulation, no further optics is needed, allowing for a very compact arrangement. Amplitude modulation is achieved with additional polarizer and analyzer.

The reflective operation mode can induce additional complexity to the setup, but the compact form and high resolution of up to 2000x1000 pixels with 20x10 mm dimension were enough good reasons to choose such a device for this work.

### LCoS Pluto from Holoeye: characterization

The Pluto phase-only modulator from Holoeye is connected to the computer as an external display and is operated by a black and white bitmap picture. The correlation of the gray level to the induced phase modulation for the used wavelength of 532 nm had to be calibrated. This was done with a Mach-Zehnder interferometer arrangement, where beams of a reference mirror and the LCD are overlaid together. In order to connect the gray level to the induced phase shift, a changing gray level from 0 (black) to 255 (white) was sent to the LCD. The individual interferograms get shifted to each other depending on the applied gray level (*fig. 17*). One line pair corresponds to a  $2\pi$  shift. From a series of measurements for every gray level, a calibration curve to correlate the phase shift with the bitmap gray value was generated (*fig. 18*).

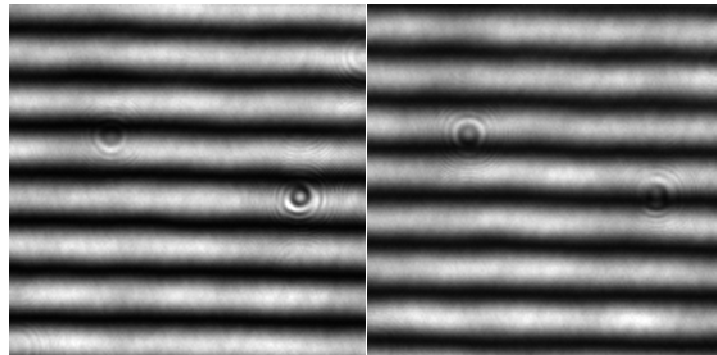


*Fig. 17: Two interference patterns used to calibrate the phase shift. Left: 0 gray level (black) sent to the LCD, right: gl 160 (corresponding to  $\pi$ ) shifts the lines by half a line pair (compare position of the dust).*



*Fig. 18: LCD calibration curve showing the induced phase shift vs. the applied gray level.*

With the same interferometric setup, the flatness of the LCD surface was measured with a four-step method [14]. From four different interferograms measured with  $90^\circ$  optical phase shifts each (fig. 19), the surface can be calculated as optical thickness  $\varphi(x,y)$  (eq. 26 & 27). Usually the phase shift is induced by a variation of the beam arm length of the reference mirror. In our case, we can directly modulate the LCD beam with the corresponding gray level values.

$$\left. \begin{array}{l} I_i = I' + I'' \cos(\varphi + \Delta_i) \\ \Delta_i = 0, \frac{\pi}{2}, \pi, \frac{3\pi}{2} \end{array} \right\} \begin{array}{l} I_1 = I' + I'' \cos \varphi \\ I_2 = I' - I'' \sin \varphi \\ I_3 = I' - I'' \cos \varphi \\ I_4 = I' + I'' \sin \varphi \end{array} \quad (26)$$

$$\varphi(x,y) = \arctan \frac{I_4 - I_2}{I_1 - I_3} \quad (27)$$

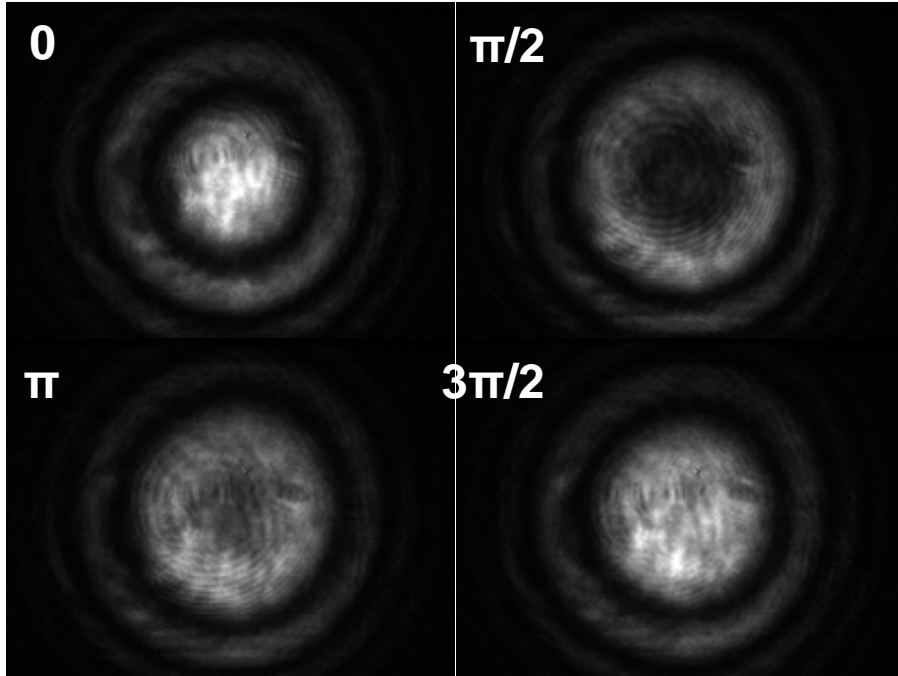


*Fig. 19: Interferograms of the SLM surface measured with  $90^\circ$  phase shifts each.*

The resulting surface curvature is presented in *figure 20*. As the arctan function returns only values between 0 and  $2\pi$ , the output is wrapped. The wrapped surface is transformed to a continuous surface with an unwrapping algorithm. A structure of the LCD mirror surface corresponds to an unwanted phase modulation.

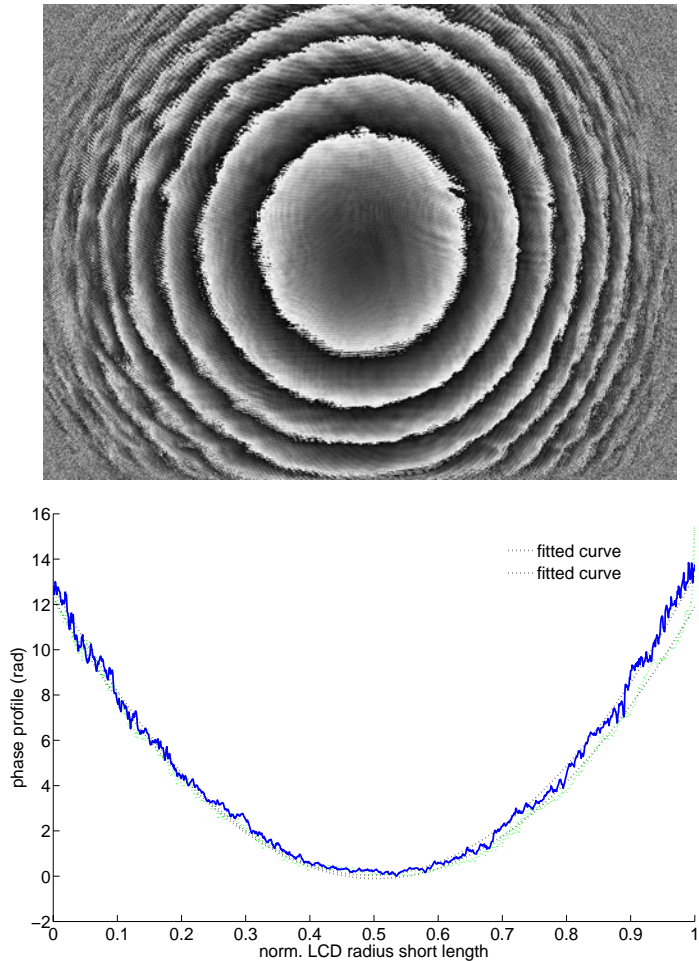


*Fig. 20: SLM surface curvature obtained by four-step interferometry. (top: 2D phase map; bottom: unwrapped profile)*

To avoid that, we compensate the surface curvature with an opposite phase modulation on the LCD. After this process, the LCD becomes optically flat which is seen from the straight interference lines (*fig. 21*).

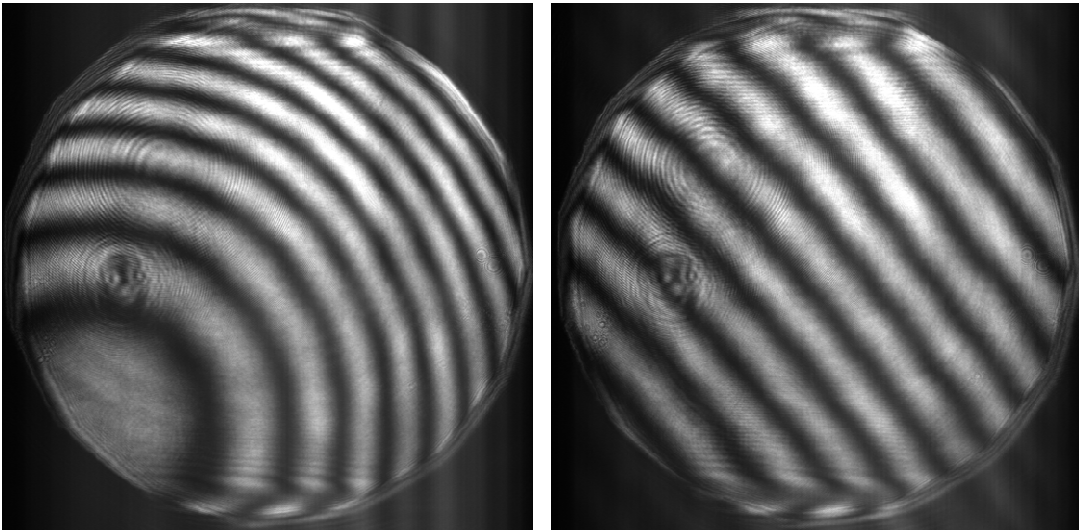


*Fig. 21: Interferogram of the SLM surface before and after flatness correction.*

### 2.4.2. Focusing into glass

For the planar refractive index mismatch, we introduce different glass plates (Thorlabs) between the two objectives (*fig. 22*): calcium fluoride ( $\text{CaF}_2$ ,  $n = 1.43$ ,  $d = 5.25$  mm), BK7 ( $n = 1.52$ ,  $d = 5.35$  mm), sapphire ( $\text{Al}_2\text{O}_3$ ,  $n_{\text{ord}} = 1.77$ ,  $d = 5.00$  mm), and a quartz glass ( $n = 1.52$ ,  $d = 8$  mm). Their refractive indices were identified at a wavelength of 532 nm. Their thickness was measured with a calliper with a measurement accuracy of 0.05 mm, which corresponds to 1 % of the thickness  $d$ . Each glass plate was evaluated independently to determine the measurement accuracy of our method.

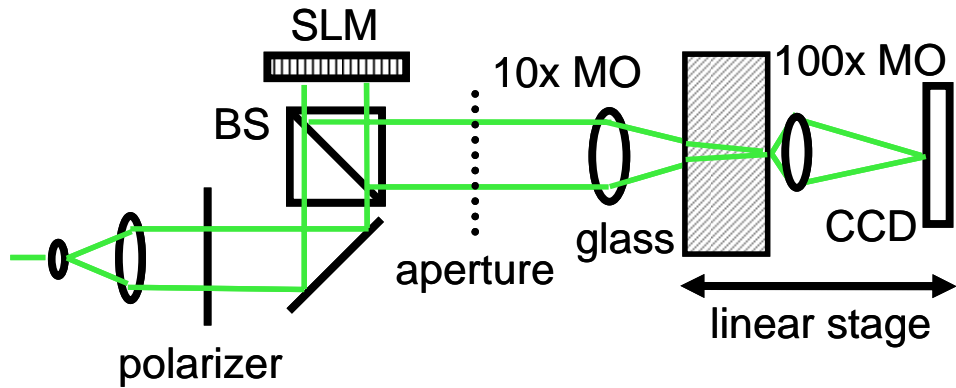


*Figure 22: Experimental setup to focus into a glass medium (BS: beam splitter, SLM: spatial light modulator; CCD: camera).*

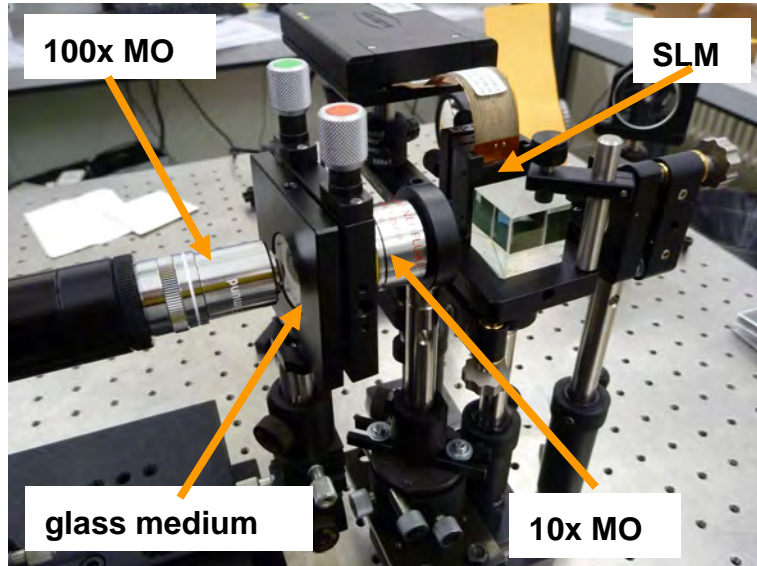


*Photo 2: Experimental setup to focus into a glass medium.*

The glass plate has to be inserted very carefully and aligned properly. By touching one of the objectives slightly, the relative position can get shifted by several  $\mu\text{m}$  and consecutive measurements become therefore inaccurate. If the glass plate is tilted, the beam gets displaced and can vanish from the detector when scanning through the focus.

## 2.5. Simulation validation with Fresnel lenses on optical fibre tips

We performed a joint project within our group, resulting in a paper in Journal of Micromechanics and Microengineering with the title “*Optimized fabrication of curved surfaces by FIB for direct focusing with glass fibres*” [23]. Victor Callegari was performing the production optimization with focused ion beam (FIB), Emanual Schmid the scanning near field optical microscopy and I was doing the numerical simulations. That was the first opportunity to validate the numerical simulations with measured data.

In that work, FIB was used to fabricate Fresnel phase lenses on optical fibre tips. The influence of dwell time and the scanning strategy to produce parabolic structures in silicon was investigated, because these parameters have a strong influence on the shape of the fabricated structures. The lens shape was characterized by atomic force microscopy and it was shown that FIB does not roughen the surfaces. The optical performance of the lenses was characterized by (SNOM) and the results were compared to simulations taking into account fabrication imperfections of the Fresnel lenses.

The contribution from the simulation was first to provide a thickness function for the production of the surface. An optimized FIB method was then used to produce a Fresnel phase lens on the centre of the tip of an optical fibre (*fig. 23 left*). The diameter was 10 µm. A FIB cross section was imaged by SEM to assess the fabrication quality (*fig. 23 right*).

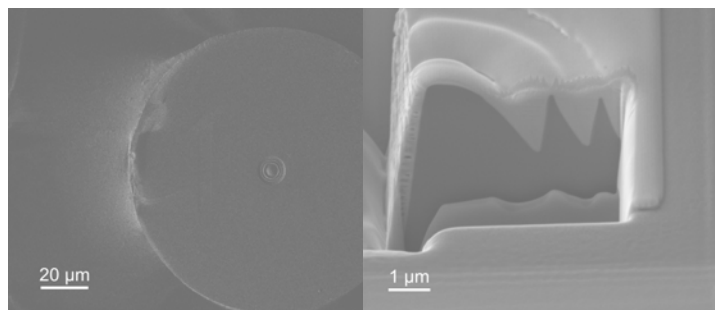


*Figure 23 left:* FIB image showing an overview of a 125 µm diameter optical fibre with a Fresnel phase lens milled on the core in the centre of the fibre. The lens diameter is 10 µm.

*Figure 23 right:* SEM micrograph of the cross section of a lens.

A comparison of the cross section expressed in phase shift with the design function is shown in *figure 24*. The general agreement is good. The largest deviations occur in the vicinity of the sharp peaks. The peaks are truncated due to the tails of the ion distribution. For the same reason, the sidewalls are slanted by about  $5^\circ$  over the depth of  $1.8 \mu\text{m}$ .

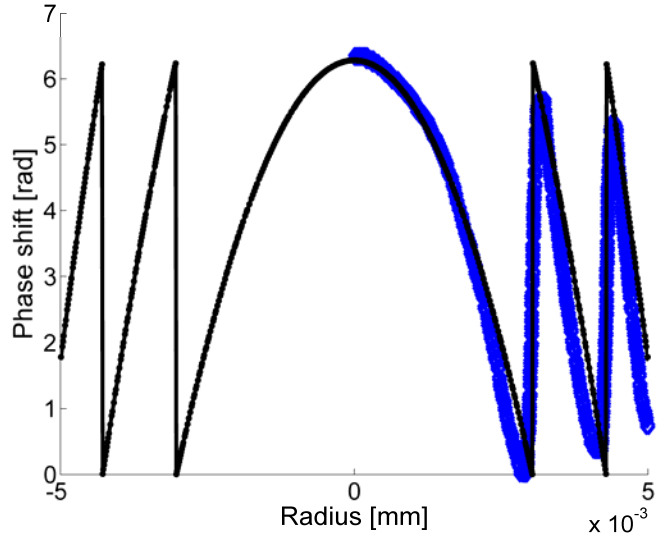


*Figure 24: Cross section of the theoretical (black) Fresnel phase surface, and the fabricated surface (blue diamonds)*

The optical properties of the lens were analyzed by SNOM at the operating wavelength of  $840 \text{ nm}$  (*fig. 25 left*, blue circles). Simulation of the axial intensity (*fig. 25 left*, red line) using the real lens profile (*fig. 24*, blue line) shows reasonable agreement with the experimental data. The deviations between the SNOM data and the simulation are partly attributed to the convolution with the SNOM fibre aperture and partly to the approximations made in the model. Alignments both during the fabrication and the measurement have minor influence. The FWHM was determined to be  $2.1 \mu\text{m}$  from the experiment and  $1.5 \mu\text{m}$  from the simulation. SNOM data and the simulated transversal intensity distribution in the focal plane are shown in *figure 5 right*. The agreement between experimental data and simulation is satisfactory. A FWHM of  $740 \text{ nm}$  is found experimentally and  $440 \text{ nm}$  from the simulation.

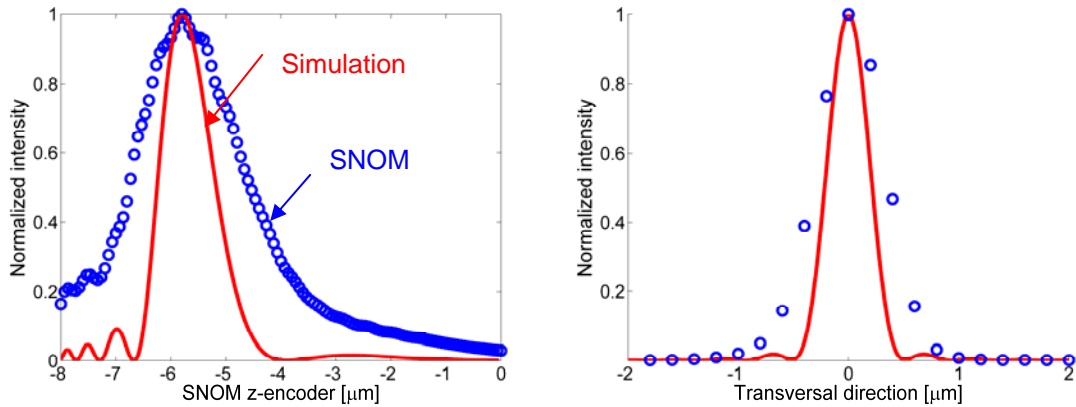


*Figure 25 left:* Normalized SNOM measurement (blue circles) and simulation (red line) of the axial distribution above the fibre surface. Because no contact could be established with the fibre,  $-8\text{ }\mu\text{m}$  does not correspond to the lens surface. *Figure 25 right:* Transversal intensity distribution at the focal position.

In summary, the optimized fabrication process was employed to fabricate Fresnel phase lenses on the facet of optical fibres. The obtained lens shape showed only small deviations mainly due to the ion beam shape, with truncated peaks and slanted ( $\sim 85^\circ$ ) sidewalls. The surface roughness was characterized by AFM to be 3.6 nm rms for the central part of the Fresnel phase lens. Optical measurements with SNOM showed satisfactory agreement with numerical simulations of real Fresnel lenses.

# Chapter 3

## Extended Depth of Field for Intra-Ocular Lens Implants

We investigated in extending the depth of field (DOF) of lenses. A brief overview of application fields is given, while special focus is laid on ophthalmologic applications. A CTI project called “Development of intra-ocular lens implants with increased depth of focus” (project nr. 9203.1) was conducted in collaboration with Contacts & Communication for Advanced Technology (CCAT, Rotkreuz) and an ophthalmologist (Dr. P. Othenin-Girard, Lausanne). The objective of the project was to develop a method to tailor the DOF of ophthalmic intra-ocular lenses (IOL) to correct focus deficiencies of the eye’s optical system after cataract surgery. Within this CTI project, we performed a study to design and manufacture intra-ocular lens (IOL) implants with increased DOF. Such lenses have the potential to replace existing monofocal cataract IOL’s. As main outcome, we developed a pure phase pupil filter, which is able to extend the DOF while maintaining a homogeneous transversal resolution. The results were published in Journal of Modern Optics [24]. In addition to the design of the pupil filter, we present further studies and features that were investigated during the CTI project.

### 3.1. Concept and applications of high DOF systems

High depth of field (DOF) lens systems hold a strong potential in a large number of applications such as optical data storage, endoscopic optical coherence tomography, microscopy, video imaging, ophthalmology, automated pattern recognition or optical microlithography. These applications require a homogeneous transversal spot size over an elongated region along the optical axis, i.e. a tube-like point spread function (PSF) (*fig. 26*). Further, the device should offer high light efficiency and should be easy to produce and implement. This device would enable to achieve a single-shot purely optical imaging of a 3D object without the need of further computational image processing.

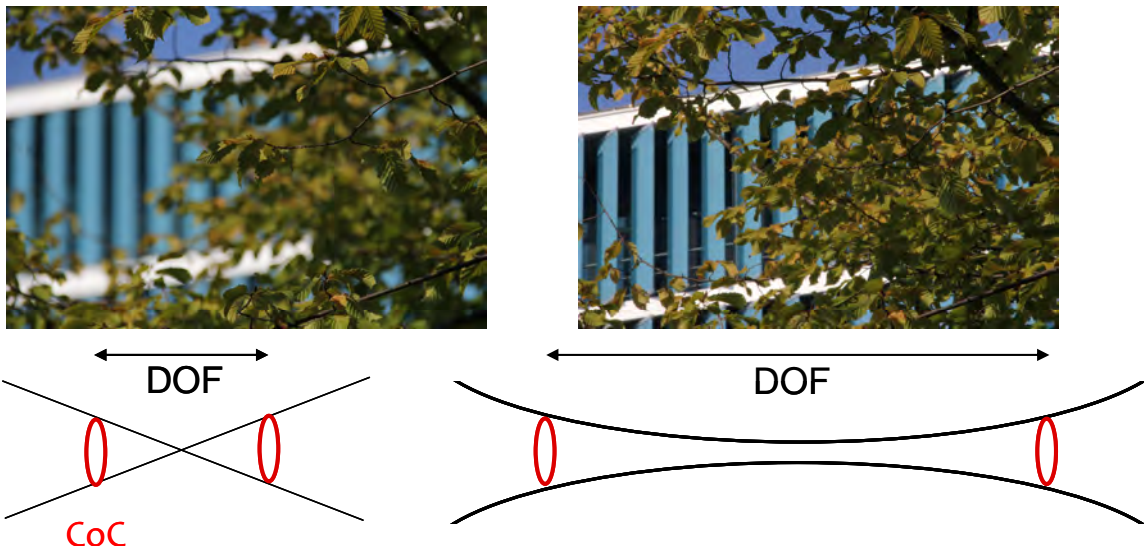


*Fig. 26: The circle of confusion (CoC) defines the depth of field.*

One possibility to generate an elongated DOF within a given numerical aperture (NA) is to combine a lens with a pupil filter. This filter modulates the amplitude, the phase, or both of the incoming wavefront within the lens or pupil plane. Many different designs have been developed so far, but their performance changes severely within the depth of field with respect to light efficiency, function complexity and transversal spot size. The goal is to elongate the axial DOF with respect to the clear pupil while to keep the transverse resolution constant and close to the diffraction limit. Inevitable side effects should be minimized, such as increased sidelobes in the transverse direction generating halo effects and a strongly reduced Strehl ra-

tio, representing a low light efficiency. Such limitations can disturb or even impede scientific measurements or industrial applications.

In the field of industrial imaging with cameras, the introduced artefacts could be removed by computational post processing. However, it must be clearly distinguished between full 3D imaging and extended DOF 3D visualisation. The former method tries to assign all objects to all three spatial coordinates. In the extended DOF method, the objects from different distances are projected equally sharp on the same 2D image with a single shot. It is not possible to assign a feature within that image back to its original axial position in the object.

## **3.2. Development of intra-ocular lens implants with increased DOF**

The CTI study was initiated to find the relevant optimised parameters of a phase pupil filter and to assess the improvement in ophthalmologic applications. Special emphasis was laid on the producibility with reasonable complexity and cost. A new technology for implantable intraocular lenses was targeted, which could solve many issues related to multifocal IOLs as it allows tailoring the DOF case by case.

### **3.2.1. Cataract surgery and intra-ocular lenses**

The human eye (*fig 27*) focuses the light onto the retina to execute vision. It has a diameter of about 24 mm and a weight of around 7.5g among adults. Imaging is performed with a two lens system, which is usually described in dioptre powers. Dioptre is the inverse of the focal length in metres. Incoming light is first refracted at the cornea, which has a refractive power of around 43 dioptres. It contributes most to the focusing in the human eye, but at a fixed focal length. The light is further passed to the iris, which is an aperture that controls the intensity of light. Its diameter varies between 2 mm at bright daylight to 8 mm in the dark. In between the cornea and the iris is the anterior chamber, also called the aqueous. The second lens is a crystalline lens with a biconvex structure. It performs the accommodation of the eye, which is the adjustment to focus at different distances by changing its shape. Its refractive power covers around 12 diopters. In its relaxed state, the crystalline lens is adjusted to far distances with around 20 diopters, thus focusing collimated light at 50 mm. To see a close object

### 3. Extended Depth of Field for Intra-Ocular Lens Implants

---

at around 10 cm distance, the ciliary muscles contract, letting the zonular fibres relax. The lens thickens and gets more bent, increasing the focusing power. To adjust the vision back to far distances, the muscles relax, stretching the fibres and thus pulling the lens back to a flatter shape. Thus, the incoming light gets focused onto the retina, which covers the whole inner back part of the eye. The retina is a layer with two kinds of receptors, rods and cones, to achieve optimized detection at different brightness and for every colour. The fovea is the spot with the highest receptor density and, therefore, produces the sharpest picture with highest spatial resolution of around  $2 \mu\text{m}$ . The optic nerves lay on the surface of the retina and are bent together at the optic disk, which is called the blind spot of the eye. The largest part of the eye is the vitreous chamber between the crystalline lens and the retina.

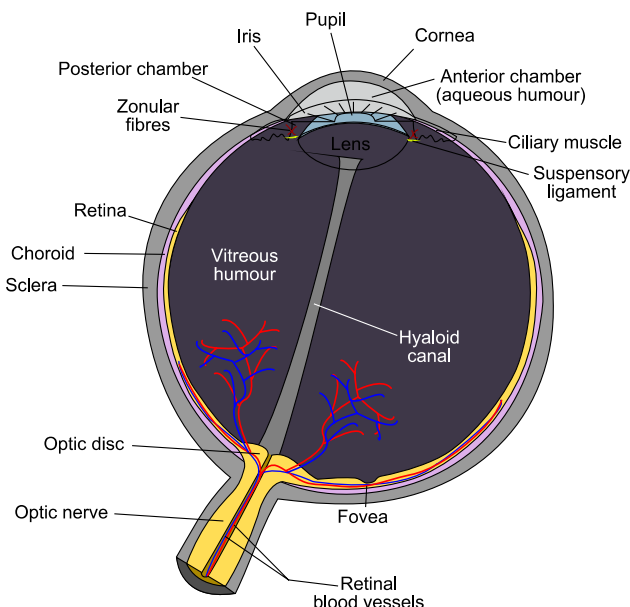


*Figure 27: Schematic drawing of the human eye (from ref [25])*

Cataract is an eye disease that clouds the natural crystalline lens. It is the most common eye disease in people over 40 years old. Age-related cataract affects around 17% of people older than 40 years and increases up to 50% of people older than 80 years. The crystalline lens consists mostly of water and proteins. With increasing age, these proteins eventually may clump together and lose their transparency, in a manner similar to cooking the white of egg. Over time the opaque region may grow larger and eventually lead to complete blindness. The exact

### 3. Extended Depth of Field for Intra-Ocular Lens Implants

reasons for this process are still unknown. Some studies suggest that UV light or other kind of radiation might alter the proteins [25].

Presbyopia is another age-related eye disease, which changes the proteins of the lens and makes it harder and less elastic. It is clearly different from near- and farsightedness, where the size of the eyeball does not match the lenses and the retina to form a clear picture. Because the lens is more difficult to bend, near vision requires more effort and thus possibly introducing eye strain, headaches and exhaustion. Presbyopia and cataract often occur at the same time and may be treated with a single surgery to replace the crystalline lens with a synthetic intra-ocular lens (IOL). Artificial IOLs were implanted for the first time in the 1960s.

To restore vision, cataract surgery has become a common technique. It is simple and relatively painless, only taking around 10 minutes to perform. During surgery, the clouded lens is replaced by an IOL implant through a small incision, which usually seals by itself afterwards. Studies reported that 95 % of the surgeries are successful. This is statistically one of the highest success rate among all surgeries. However, the ability of the eye to change focus for near and far distances gets lost, because the new implant cannot be attached to the muscular system of the eye. Monofocal lenses, therefore, enable acute vision only in the distance they were designed, either near, intermediate or far. New types of IOL were developed to increase the depth of field, which are discussed in the next sub-chapter.

There still remain unsolved issues regarding cataract surgery:

- Adequate choice of the material and the optical design to avoid rejection, glare and halo.
- Inaccuracy in measurements of all dimensions of the eye to compute the required power correction.
- Inaccuracy in measurements of the focusing power of the lenses because of the use of hydrophilic materials.
- Inaccuracy in positioning of the lens in the centre of the eye.
- Development of special versions for customized designs, for example against astigmatism and extreme eye dimensions (near- and farsightedness).

The goal of this CTI project was to find an optical design to optimize vision with minimized side effects described above. Consecutive steps are a concern of medicine to solve the remaining problems of customized designs for individual patients including eye measurements and accurate positioning.

#### **3.2.2. State-of-the-art of IOLs**

The market for cataract surgery is huge and still growing. The development of new designs for better vision is crucial, introducing a nice competition among producers. Therefore, neither details nor publications are available for these designs. For this reason, only their basic ideas will be presented generally without references to the companies. [26, 27]

##### Monofocal lenses

Traditional IOLs are monofocal, i.e. they offer clear vision at one distance only (either far, intermediate or near). This means that one must wear eyeglasses or contact lenses for the other distances. In the last few years, new IOLs were introduced and the patient has to choose from a variety of designs. If both eyes are affected by cataract, it is possible to implement two different mono-focal IOLs. Usually one can adapt to such vision, but the estimation of depth and distances might become disturbed.

##### Bi-, tri- and multi-focal lenses

Bi- and tri-focal lenses enable simultaneous clear vision at two or three distances. The multi-focal lenses try to achieve full vision in near, intermediate and far vision homogeneously. They all divide the circular lens surface into a number of zones, each of which focuses the light with different power [28]. Only the light from the respective distance becomes focused on the retina through that zone, while light from other distances adds homogeneously to the background. The brain is able to adapt to the new kind of vision and only “see” the wanted picture ignoring the other inputs. However, there remain certain distances where the brain cannot focus on and where the image remains blurry. In addition, only a portion of the lens produces the final image, while the rest of the light is lost or evenly distributed over the retina

as background. This is a reason why the vision still remains worse than usual, especially under low light conditions.

#### Accommodating lenses

Accommodating lenses restore the original natural system with a lens that can adapt to different vision distances [29]. They have a large advantage over multi-focal IOLs, because the full incoming light is focused onto the retina as in healthy natural vision. This reduces diffuse and blurry images. There are different possibilities to achieve a modulation of the lens with the eye muscles. The idea of these accommodating IOLs include that the ciliary body directly causes the IOL to vault. Therefore, either the ciliary body presses directly on the lens, or the contraction of the ciliary muscle generates a pressure gradient between the aqueous and vitreous, causing displacement of the anterior diaphragm and steepening of the anterior central lens curvature. The amount of excursion generated (usually between 0.4 and 0.7 mm) limits the accommodative range of a design with only one lens. Another design is produced from a silicon gel or fluid-based structures, which get reshaped by movements of the eye muscles, very similar to the crystalline lens. However, accommodation performance is much worse than that of the natural crystalline lens. For reading, therefore, glasses are still needed.

In summary, it is expected that multi-focal and accommodating lenses will become the standard technique in cataract surgery. The designs need further visual improvement to avoid blur and halo, though. The achieved changes of the focal length for currently approved IOLs are of the order of 2 dioptres, which is not fully satisfactory compared to a normal eye performance of 12 dioptres. Therefore, even if multifocal or accommodating IOLs have been implanted, no one can be 100 percent certain of seeing well without eyeglasses or contact lenses after cataract surgery.

### 3.3. State-of-the-art of pupil filter designs for extended DOF

Pupil filters can be designed to extend the DOF. To compare the reported designs and highlight their advantages and drawbacks, a detailed analysis of the obtained intensity distribution was performed. Different vocabulary was invented to name an extension of the DOF that all mean the same physical performance: pseudo non-diffractive beams, uniform intensity, Bessel beam and long beam.

#### Amplitude filters

Several studies reported an increased DOF with amplitude modulations. Binary 2- and 3- zone filters became very popular [30-32]. They are easy to adapt for different DOF extension performances and to implement in the experiment.

Continuous amplitude filters [33-35] produce a nice homogeneous extended DOF. Because of the gray values that need to be generated, they need a rather complicated set-up for the implementation.

Amplitude filters can have a good performance to extend the DOF, but they show inhomogeneous transversal spot sizes within the DOF. The main disadvantage, however, is the immense loss of light with efficiencies below 5%.

#### Phase filters

To avoid the loss of light, phase-only pupil filter designs were considered and have taken the lead. Many different phase filter designs with radial symmetry were published to achieve a high DOF: continuous [36-39], binary multi-zone [40-43], diffractive [44-46], multifocal [47, 48] and multiplex filters [49, 50]. Angular dependent modulations were also proposed, as in the light sword optical element [51]. The main idea is to focus the light to different axial positions depending on the angular coordinate. The resulting PSF has a helix shape, requiring computational post processing in imaging applications.

The common disadvantage of all these phase-only designs is that they lead to an inhomogeneous transversal spot size within the elongated focus for short focal lengths. As no light is blocked, the redistributed light decreases the image contrast. In the extreme case the transversal side lobes of the intensity distribution are much larger than the actual main peak. Such

ring artefacts can disturb or even impede many scientific measurements or industrial and ophthalmologic applications. Although some diffractive phase filters show a constant transversal gain, they have complicated structures that need multiple difficult fabrication steps, which can introduce artefacts due to higher diffraction orders [45]. The 3-zone binary phase filter is a simple design, but its practical performance is limited to an axial gain of around 1.2. For higher gains the transversal spot is extremely inhomogeneous [31, 52].

#### Complex filters

Complex filters have the largest variety of intensity distributions due to many free parameters from the combination of amplitude and phase functions. Many different designs to extend the DOF have been published [53-56]. A nice recursive design simplification was shown with a Fourier transform approach, obtaining a complex function to extend the DOF with an adjustable gain [57]. Radial multi-zone filters are able to generate high DOF with large gain [58]. Another common type of pupil filters for extended DOF are axicons [59]. Linear axicons are a combination of a binary amplitude ring mask with a linear phase modulation, without the use of a lens [60, 61]. Logarithmic axicons have a lens with or without a simple phase function in addition to the amplitude ring mask [62-64]. The design is usually pretty simple. The picture captured with a camera usually needs further computational processing to obtain a representation of the object, making it inappropriate for real-time observation or ophthalmology.

Equivalent to amplitude filters, the light efficiency is low for complex filters. In addition, the complicated implementation of two modulation systems, the amplitude and the phase, makes complex pupil filters impractical. The total amount of optical components and the difficult precise alignment of both modulators prevent a compact easy to use device. Some complex pupil filter designs are able to generate a homogeneous transversal spot size, but with a very low light efficiency of below 1%.

#### **3.4. Quartic Multiplex (QM) lens design**

To improve multifocal IOLs, our goal was to enlarge the field of view homogeneously for simultaneous near, intermediate and far vision and therefore to avoid regions with strong blur.

We developed a new design which we called Quartic Multiplex (QM) and tested it with numerical simulations of the PSF based on the scalar diffraction theory (*eq. 22-24 in chap. 2.1*). Experimental proof is given with the basic focusing set-up (*chap. 2.3*). To adapt the use of the pupil filter for IOL purposes, we scaled the eye properties by a factor of 2. Therefore, the lens diameter was set to 10 mm and the focal length to 100 mm, resulting in a NA of 0.05, similar to the eye's NA. The focusing range of common multi-focal IOLs is 2 dioptres on top of the 43 dioptres of the cornea, which is equivalent for a combined focusing range of 22 to 24 mm. The DOF of a diffraction limited lens with a NA of 0.05 is 0.5 mm. Therefore, we designed our pupil filter for a four-fold increased DOF to obtain the required 2 mm DOF.

Quartic-polynomial pure-phase radial-symmetric functions were reported to generate a high DOF with good efficiency [36]. The pupil functions are:

$$P_{\pm}(\rho) = \exp(-\frac{1}{2}ik(A_1 \cdot \rho^2 \pm A_2 \cdot \rho^4)) \quad (28)$$

where  $A_1$  induces a focal shift and  $A_2$  generates spherical aberration which results in an extended focus. A positive sign of the quartic coefficient  $A_2$  extends the axial distribution away from the lens, while a negative sign extends it towards the lens. In transversal direction, there is an apodization at one end of the DOF and a superresolution effect at the other end. Depending on the sign of the quartic coefficient, this effect is mirrored.

The basic idea of our design is to combine two quartic functions with the same  $A_2$  value but with opposite signs. The resulting PSF would have the same DOF as the two single functions produce. In transversal direction, a combination of an apodization and superresolution at each end should eliminate each other and generate a diffraction limited, homogeneous transversal spot over the elongated DOF. Therefore, the first step was to obtain two quartic functions  $P_+$  and  $P_-$  with overlapping axial intensity distributions. The same  $A_2$  value with different signs was used to obtain the same axial gain of the DOF. However, without a focal shift, the two resulting distributions are completely separated, each one at one side of the corresponding unmodulated reference distribution. For that reason, one function is shifted by adjusting its quadratic parameter  $A_1$  until the axial intensity distribution of both functions overlap. The re-

maining task was to combine the functions in an appropriate way to generate the desired intensity distribution.

Several approaches were attempted. First, a linear addition or an averaged function do not result in an extended DOF distribution. Both methods eliminate the quartic order term and lead to a simple quadratic function, which is just a focus shift. If the two quartic parameters have a different value, the resulting function tends towards the larger absolute  $A_2$  value with considerably smaller extension of the DOF and still inhomogeneous transversal spot size.

Therefore, the pupil plane was divided into radial zones each assigned with alternating quartic functions. However, a two zone approach did not result in the desired distribution. By dividing the pupil plane into two radial zones with equal area, one function is only performed in the central region while the other function is applied to the outer region. Because the spherical aberration term, depending on the radius to the power of four, is much more prominent at the outer region, the two functions did not perform equally. Therefore, the two distributions did not overlap properly and the effective performance was not satisfactory. Consequently, we divided the pupil plane into several radial zones with alternating quartic functions. In that case, both functions are applied at inner and outer regions in a multiplexed manner. Thus, we called our design Quartic Multiplex (QM). The remaining task was to find a reasonable width of the radial zones. There is a trade-off between complexity of the function with many zones and performance of the final pupil function. With few zones, the distribution remains simple with few changes, but the distribution of the two functions to inner and outer zones is insufficient to get a proper overlap of their resulting intensity distributions. With more zones, that overlap becomes better with the drawback of a more complicated pupil function. We decided to define radial zones of alternating functions with the same radial width  $\rho_z$ , which simplifies the design and is a reasonable approximation that both functions  $P_+$  and  $P_-$  cover a similar pupil area for enough numbers of zones:

$$P_{QM} = \left\{ \begin{array}{ll} P_+ & 0 \leq \rho < \rho_z \\ P_- & \rho_z \leq \rho < 2\rho_z \\ P_+ & 2\rho_z \leq \rho < 3\rho_z \\ \dots & \\ & \rho_{max} \end{array} \right\} \quad (29)$$

We thus obtain a phase function that shows a mix of continuous and diffractive behaviour. By extending the first radial zone to  $\rho_z = \rho_{\max}$  one obtains a purely continuous behaviour of one of the quartic functions. On the other hand, if the radial zone width becomes very small with a width of one pixel, a purely diffractive behaviour is obtained. From the simulations we expected a reasonable performance with around 10-20 radial zones, which results in a zone width of 0.5-0.25 mm for a 10 mm diameter lens.

To demonstrate the use for IOLs, the axial gain  $G_A$  was set to four as previously stated. This leads to a quartic parameter of  $A_2 = 5.2*10^{-5} \text{ mm}^{-3}$  and quadratic parameters of  $A_1 = 0$  and  $0.55 \text{ mm}^{-1}$ , respectively. The latter value corresponds to a focal shift of 1.8 mm. The argument of the Quartic Multiplex phase function  $P_{QM}$  is shown in *figure 28*. The upper and lower envelopes represent the argument of the  $P_+$  and  $P_-$  function, respectively.

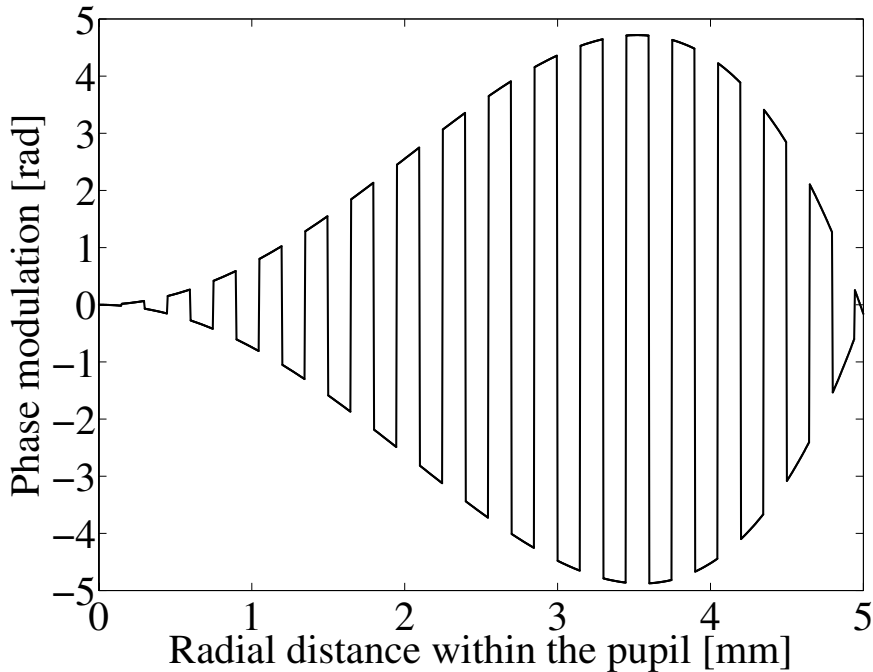


*Fig. 28: Argument of the phase function  $P_{QM}$  of the Quartic Multiplex design.*

### 3.5. QM focusing results

To illustrate the performance of the QM design, we present results for the following situation in *table 4*: the unmodulated lens with  $f = 100$  mm (RL100), the two quartic functions ( $P_+$  and  $P_-$ ), and the Quartic Multiplex (QM). The most important quantity of interest for this application is the *FWHM* of the transversal intensity distribution along the DOF. The transversal gain along the DOF directly represents the transversal homogeneity of the elongated focus. While a gain factor larger than 1 corresponds to an apodization of the spot, a gain factor smaller than 1 corresponds to a narrowing of the spot, i.e. superresolution in case of a diffraction limited lens.

The results of the simulation and the experiment are discussed in the following subsections. The spot size obtained by the reference lens is the basis for calculating the axial and transversal gains. The minimal and maximal transversal gains were evaluated only for axial positions with intensities higher than a quarter of the maximum intensity.

**Table 4:** Axial and transversal gain for four designs: simulation and experiment.

Design	Simulation				Experiment			
	Axial		Transversal		Axial		Transversal	
	DOF	Gain	$G_T$ min	$G_T$ max	DOF	Gain	$G_T$ min	$G_T$ max
	[mm]	$G_A$			[mm]	$G_A$		
RL100	0.39	1.0	1.00	1.06	0.72	1.0	1.00	1.8
$P_+$	1.61	4.1	0.68	2.80	2.30	3.2	0.90	2.8
$P_-$	1.61	4.1	0.68	2.80	1.93	2.7	0.89	2.7
QM	2.10	5.3	0.95	1.05	2.80	3.9	1.29	1.7

#### 3.5.1. Numerical results

The simulated axial intensity distributions are shown in *figure 29* for the four designs. The intensity is scaled with respect to the reference lens so that the relative intensity is given by the

Strehl ratio of the pupil filter. The simulated intensity distribution of the reference lens, supposed to be diffraction limited, is shown by the dotted line.

The axial intensity distributions of the quartic functions  $P_+$  (solid) and  $P_-$  (circles) show an axially extended depth of focus. It is apparent that  $P_+$  and  $P_-$  have the same axial intensity distribution split into a double peak. The axial gain is 4.1 relative to that obtained with the reference lens. The Strehl ratio is 0.26, which reflects a high light efficiency. The Quartic Multiplex function (dashed) shows a slightly higher axial gain of 5.3 with a Strehl ratio of 0.13. The distribution throughout the depth of focus is spread over multiple peaks and shows regions with zero light.

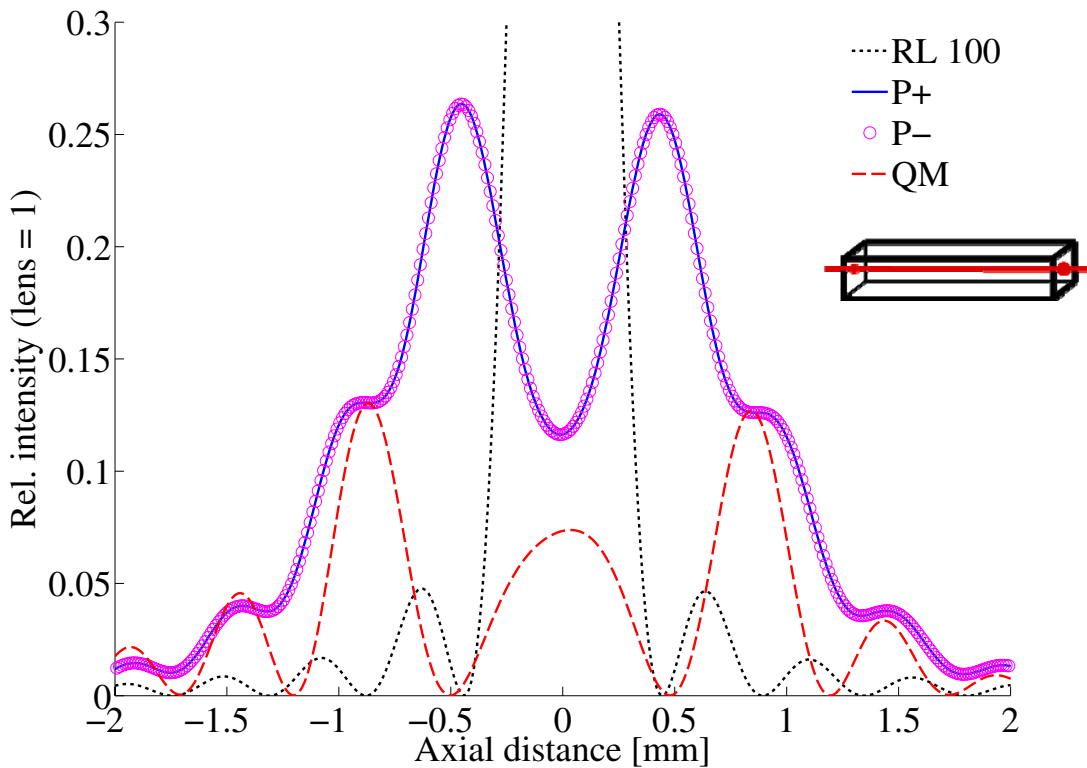


*Fig. 29: Simulated axial intensity distributions: reference lens with  $f = 100$  mm (dotted), 2 quartic functions with identical shape ( $P_+$ : solid,  $P_-$ : circles), and the Quartic Multiplex QM (dashed).*

The three-dimensional intensity distributions are shown in *figure 30*. The optical axis is scaled in mm, while the transversal axis is scaled to the full width half maximum of the reference lens (*fig. 30a*). The individual quartic functions show an inhomogeneous transversal spot size within the region of interest. The positive function  $P_+$  (*fig. 30b*) has a narrowed spot size

closer to the lens (to the left) with a  $G_T$  of 0.68 and a widened spot with a  $G_T$  of 2.8 further away from the lens. In the centre, the spot size is equal to that obtained with the reference lens. In addition, one can observe side-lobes of weaker intensity in which the transversal spot is narrower than that obtained by the reference lens. The negative function  $P_-$  (*fig. 30c*) behaves in a similar manner but with mirror symmetry with respect to the focal plane.

The Quartic Multiplex (*fig. 30d*) combines the transversal performance while keeping the extended depth of focus. The transversal FWHM of the Quartic Multiplex remains constant over the complete DoF, even within the small axial side-lobes outside the DoF. However, the main axial distribution is seen to split into 3 peaks due to interference effects. At regions where the on-axis axial intensity distribution tends to zero, a ring-shaped pattern is observed in the transversal cross-section instead of a circular spot.

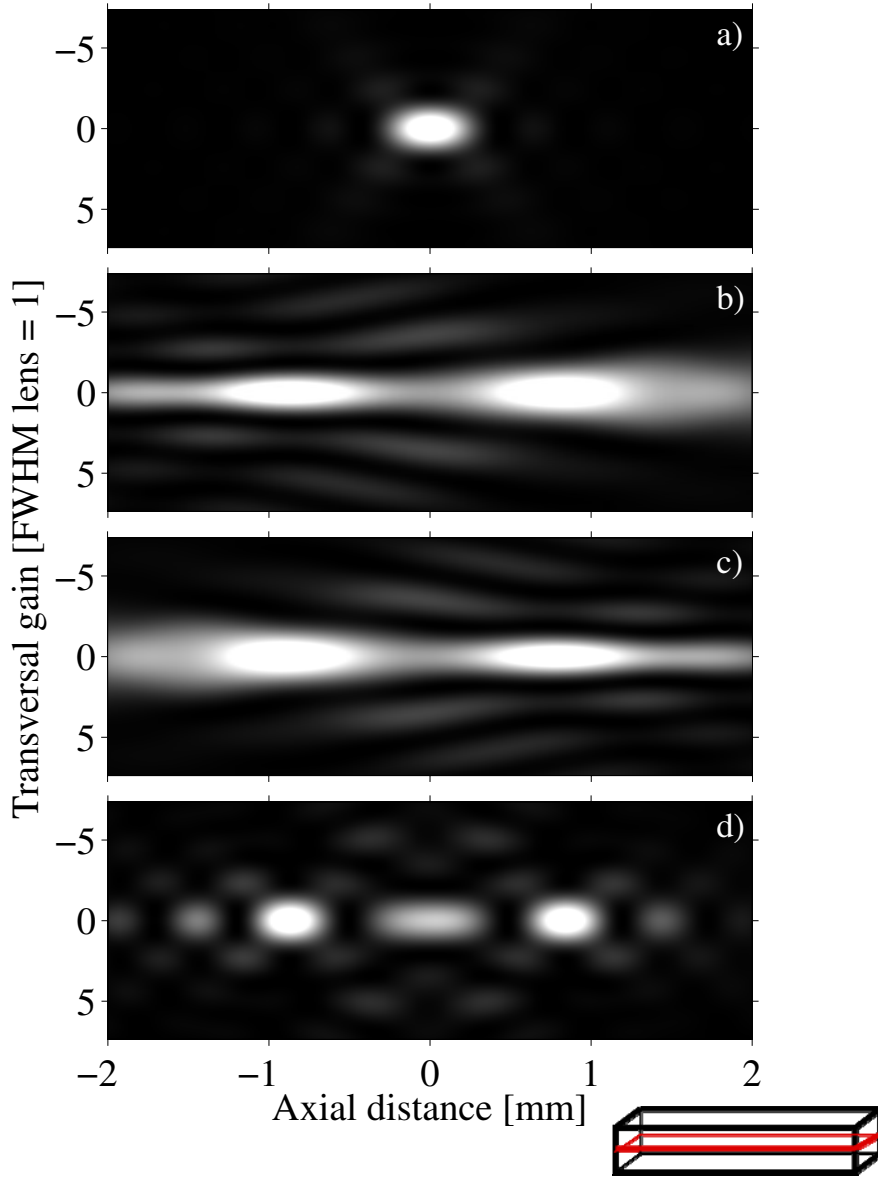


*Fig. 30: Simulated three-dimensional intensity distributions. The lateral coordinate is scaled to the FWHM of the unmodulated lens. a) RL100, b) positive quartic function  $P_+$ , c) negative quartic function  $P_-$ , d) Quartic Multiplex.*

### 3.5.2. Experimental results

The experimentally measured axial intensity distributions for the four pupil filters are shown in *figure 31*. The signal to noise ratio was optimized for every measurement by maximizing the camera integration time close to saturation at the maximum position. Therefore, the Strehl ratio of the different pupil filter designs relative to the reference peak was not measured, and all axial intensity distributions were normalized to 1. The reference lens (dotted line) is not

diffraction limited and shows an axial apodization of around a factor of two as compared to the numerical simulation. The axial intensity distributions of the quartic functions  $P_+$  (solid) and  $P_-$  (circles) show an extended depth of focus with an axial gain of around 3 compared to the reference lens. The positive function  $P_+$  decreases to the right with some wiggles while the negative function  $P_-$  does so to the left. However, they are not symmetric due to higher order aberrations. The Quartic Multiplex (dashed) shows a higher axial gain of 3.9. As predicted from the simulations, the axial intensity distribution shows interference effects resulting in multiple peaks with almost no intensity in between.

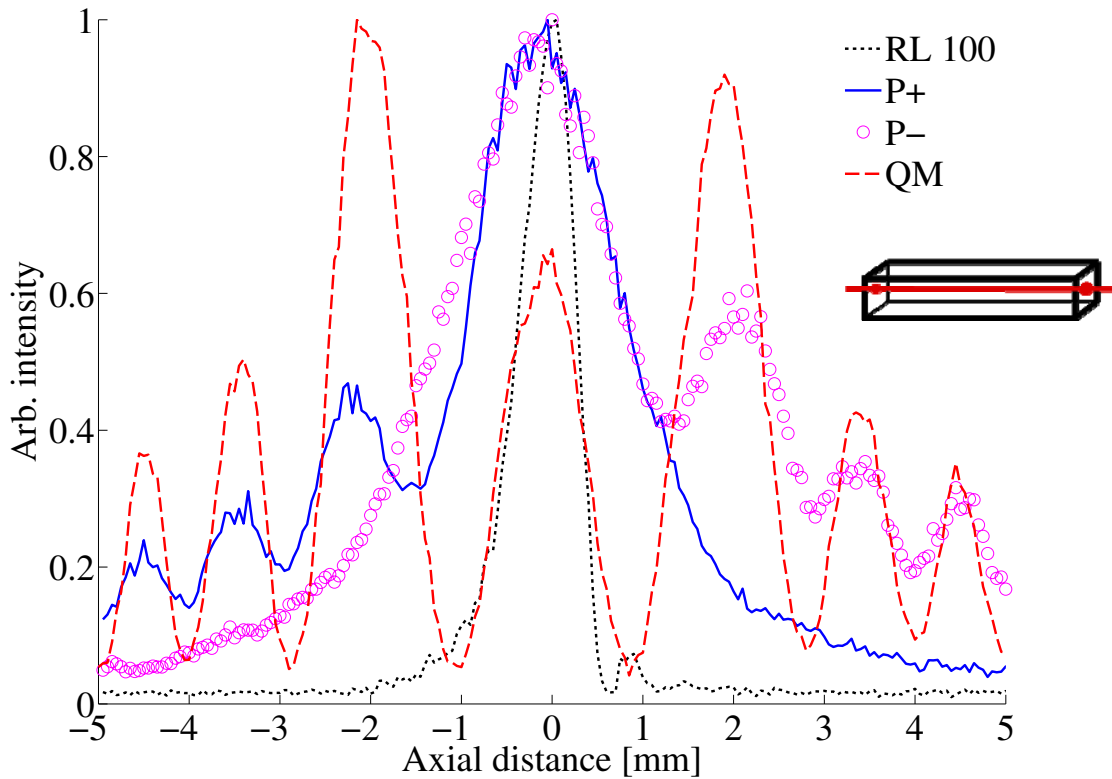
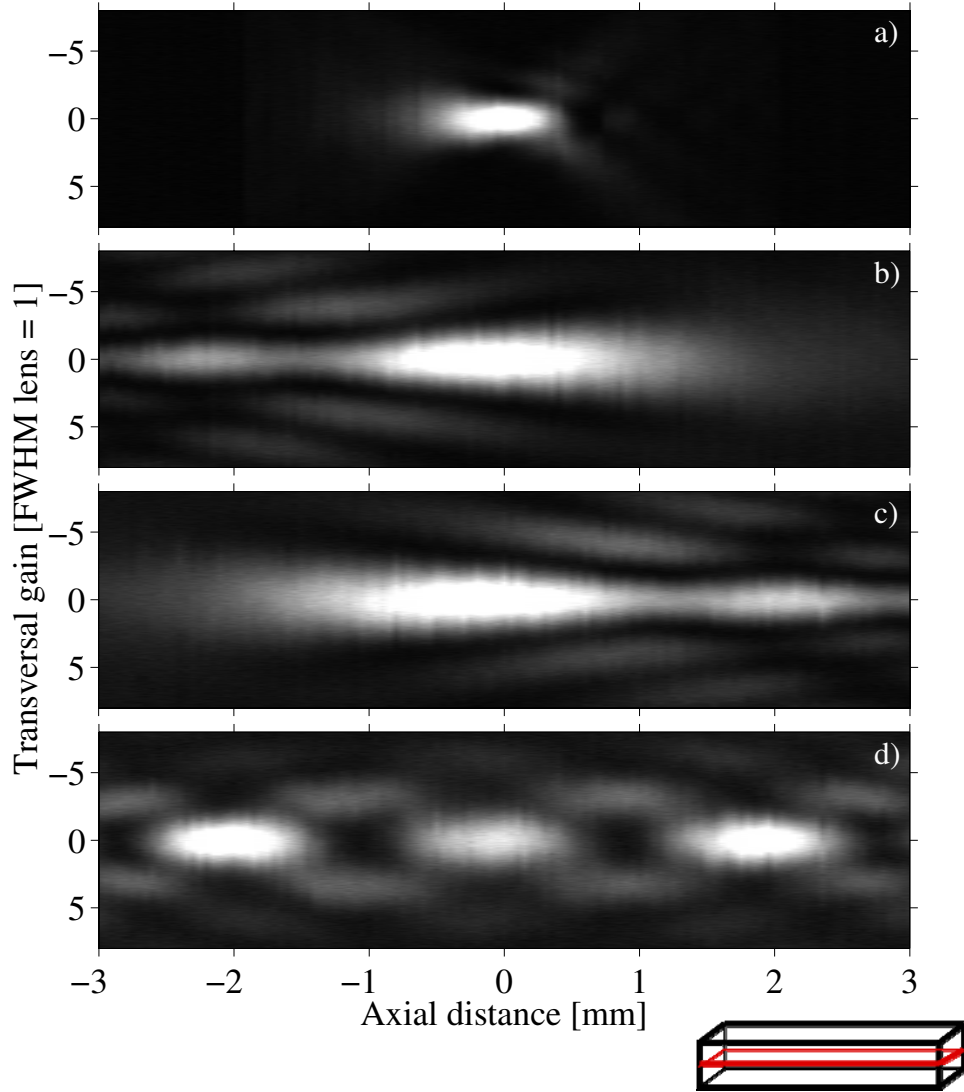


Fig. 31: Measured axial intensity distributions: reference lens with focus 100 mm (dotted), quartic function  $P_+$  (solid) and  $P_-$  (circles), and Quartic Multiplex QM (dashed).

The measured three-dimensional intensity distributions are shown in figure 32. The transversal gain for the measured  $FWHM$  of the reference lens is again set to 1. The simulated data are quite faithfully reproduced in the experiment. The positive (fig. 32b) and the negative (fig. 32c) quartic functions are seen to perform in a similar manner. The intensity distribution of the Quartic Multiplex (fig. 32d) shows an extended depth of focus with a constant transver-

sal spot size within the main peak and the axial side-peaks. The transversal gain varies around  $1.45 \pm 0.15$ . The interference effect is visible as is the formation of ring-shaped transversal spots across the cross-section between the axial peaks.



*Fig. 32: Measured three-dimensional intensity distributions. The lateral coordinate is set to 1 for the FWHM of the unmodulated lens. a) RL100, b)  $P_+$ , c)  $P_-$ , d) QM.*

### 3.5.3. Discussion

We have shown that a homogeneous spot over an elongated depth of focus can be generated using a Quartic Multiplex pure-phase pupil filter. The transversal gain is constant within 15 % over the extended DOF. The Strehl ratio from simulation is around 0.15, which is much better

than that obtained by complex pupil filters [57, 58] with values below 0.01 for a similar extended DOF. The results from the numerical simulation are validated with experimental results for  $\lambda = 532$  nm and a four-fold gain of the depth of focus. For comparison, we have also considered a continuous pure quartic phase function, which though providing a similar axial performance sees its transversal spot size change by a factor of 3 over the DOF.

There are minute deviations between the numerical simulation and the experimental data. Diffraction limited focusing is only achieved with perfect optics and proper alignment. In our experiment, there are many sources that introduce additional unwanted aberrations to the wavefront. The bent surface of the Pluto phase-SLM had to be corrected with a spherical term of around 3-4 wavelengths to minimize aberrations in the experiment, while higher order aberrations of the SLM were not accounted for. The reference lens used in the experiment, an optimized singlet lens, is not diffraction limited. Slight misalignment between the laser beam and the pupil function on the LCD-SLM may introduce asymmetric deviations from the simulation. However, The individual quartic functions show clearly each a superresolving and an apodized end with equal central spot size, which is in agreement with the simulations and the literature [53, 56]. The Quartic Multiplex performs as expected giving a homogeneous spot with constant size divided in multiple peaks.

Compared to other designs, the combination of high light efficiency, axial performance and simplicity of the function is very good with the proposed Quartic Multiplex design. The advantage of our design over other multiplex designs [49, 50] resides in its superior performance in terms of providing a piecewise continuous phase with only few diffractive features, a preservation of radial symmetry and a constant transversal spot size close to the diffraction limit. Further investigations have revealed that the proposed design has the potential to produce good transversal results even with an axial gain of more than 12. This allows for an independent customization of the elongation performance according to the needs of the target application.

The apparent disadvantage in single wavelength illumination are the multiple axial peaks and on-axis regions without any light. The regions of zero light intensity arise due to interference effects and are expected to vanish under white light illumination. A processed glass plate

with a surface structure corresponding to the phase function could be used instead of a SLM to implement the pupil filter with white light illumination.

### **3.6. Extended simulation studies for specific applications**

Based on first results of the QM design, we investigated in further possibilities and features to improve the extended DOF system.

#### **3.6.1. Performance comparison of $\rho^4$ and $\rho^6$ terms**

In order to test whether higher order terms could improve the performance of extending the DOF, a comparison was done between the fourth and sixth order term (*eq. 30*). The focal length parameter  $A_1$  was fixed to  $-1/45 \text{ mm}^{-1}$ , while the third order spherical aberration term  $A_2$  was changed between 0 and  $30*10^{-5} \text{ mm}^{-3}$ . Larger values reduced the Strehl ratio below 0.5 % and were not considered. The mean Strehl ratio inside the DOF was plotted against DOF and  $(\text{DOF})^{-1}$ . To compare this with the next higher order coefficient  $A_3$ , the  $A_2$  value was fixed at a certain value, changing  $A_3$  continuously from 0 to  $1*10^{-5} \text{ mm}^{-5}$ , representing the same range as before. This was done for 10 different  $A_2$  values (*fig. 33*). Differences in efficiency should increase or decrease the slopes of the lines with changing  $A_3$ .

$$\varphi \propto A_1\rho^2 + A_2\rho^4 + A_3\rho^6 \quad (30)$$

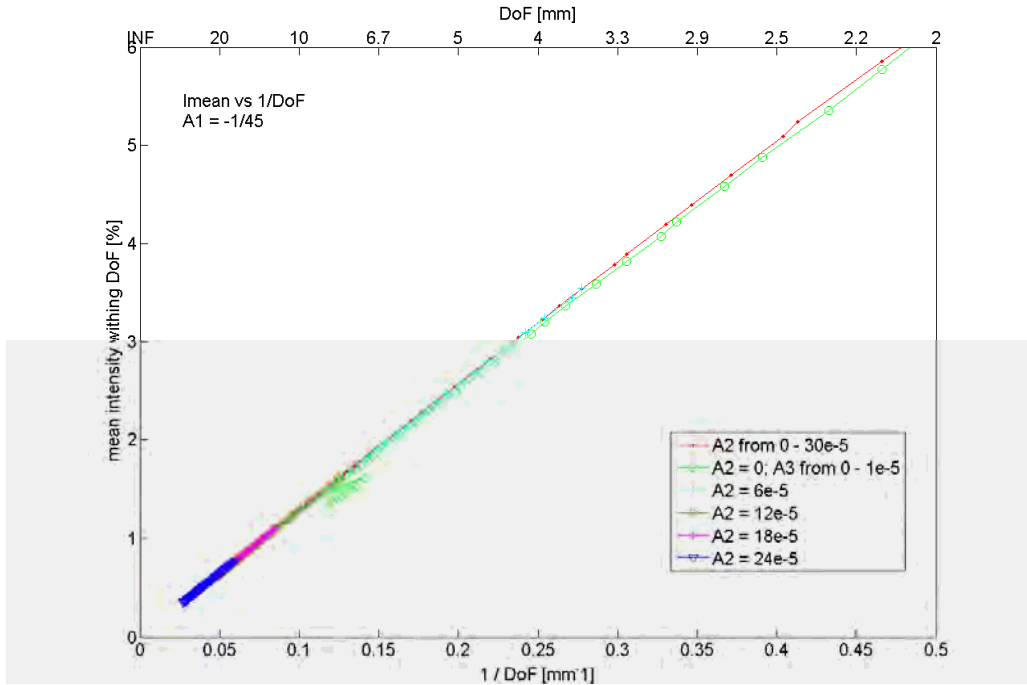


*Fig. 33: Comparison of a quartic function (red curve) with different sixth-order functions, which all have different fixed quartic coefficients. The gradient of all curves is equal, showing that the DOF performance of the fourth and sixth order coefficient is equal. The shift of the last few green points ( $A_2 = 0$ ,  $A_3$  variable) is an artefact created during automated data extraction.*

The resulting figures showed, however, that the slopes of changing  $A_2$  were almost exactly the same as those of changing  $A_3$ . The product DOF times Strehl ratio is constant and equal for the quartic and the sixth order parameter. That led to the assumption that the  $A_2$  coefficient was totally sufficient to extend the DOF, even giving a more homogeneous axial distribution than a combination of  $A_2$  and  $A_3$  coefficients with similar value of DOF (fig. 34).

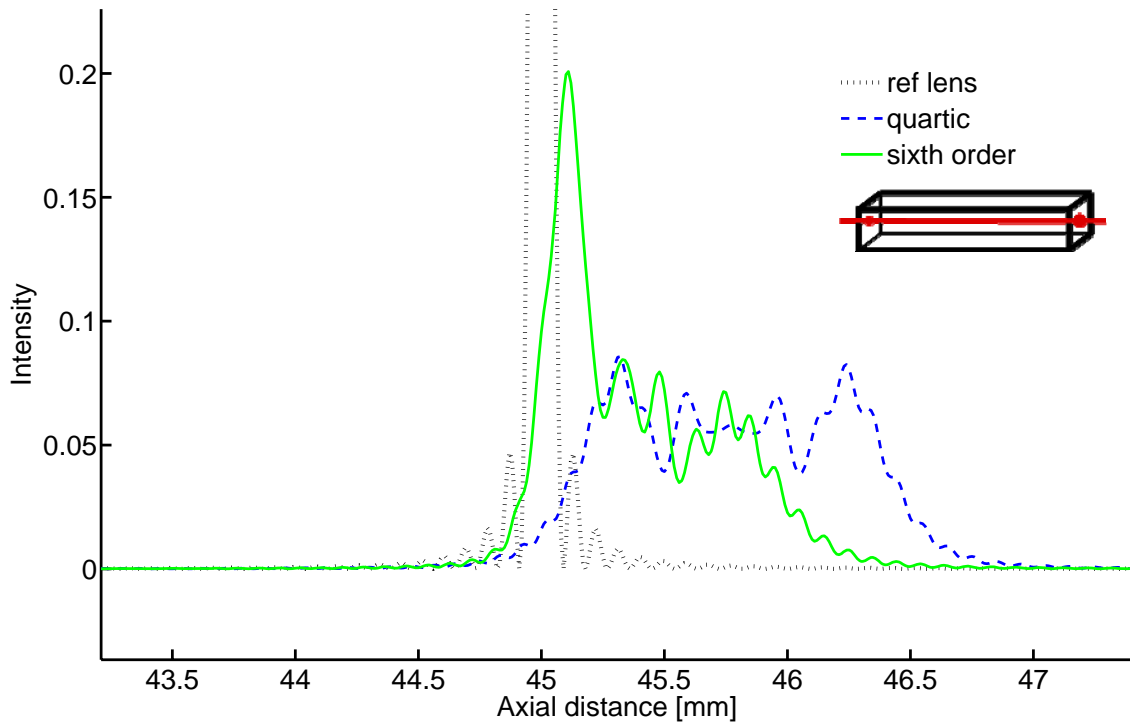


*Fig. 34: Extending the DOF to the same gain with a quartic (blue dashed) and sixth order (green solid) function.*

### 3.6.2. Simulations of finite distance imaging

To account for imaging objects at finite distance, spherical waves originating from axial points in object space were included. While for incident uniform plane waves, the phase front after the lens is equal to the pupil function, for incident spherical waves, an additional quadratic phase term is needed similar to the lens term to describe the refraction:

$$F_{tot} = F_{pupil} + \frac{k \cdot \rho^2}{2 \cdot dist} \quad (31)$$

For positive values of the distance, a diverging wavefront enters the pupil plane, while a negative value of the distance corresponds to a converging wavefront. *Figure 35* (dotted lines) shows the performance of a diffraction limited lens with focal length of 45 mm for single on-axis object points at different distances from infinity to 90 mm ( $2f$ ). It is consistent with the lens maker's equation, where the  $2f$  imaging gives the image also at  $2f$  with a magnification of

1. The analysis of a simple quartic  $P_+$  pupil filter showed that it performs qualitatively in the same way for any distance of the object (*Fig. 35*, full lines). This indicates that the phase pupil functions should perform as expected also for imaging applications.

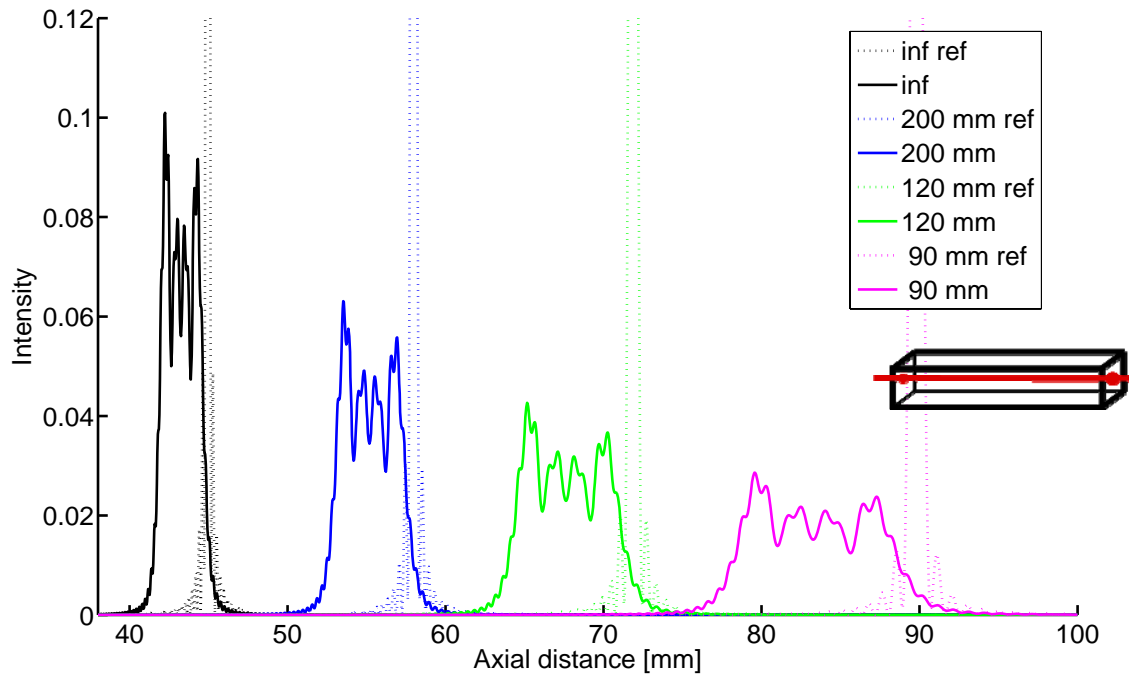


*Figure 35: Axial intensity distributions for the reference lens (dotted) and a simple quartic  $P_+$  pupil filter (dashed) for on-axis point objects with different finite distances (in colours).*

### 3.6.3. Simulations of white light illumination

Up to now, all the simulations and experiments were done at a single wavelength of 532 nm. Since the light in nature is polychromatic, it is important to assess the performance of the pupil filter in the entire visible spectrum (400–700 nm). It turns out that for larger wavelengths the elongation becomes more prominent. That makes sense, since the axial resolution is proportional to the wavelength (*eq. 2*). Therefore, the DOF increases for longer wavelengths. This effect occurs for a lens only calculation as well as for the different pupil functions.

To simulate the white light performance of the pupil filter, the calculation was repeated for discrete wavelength values. For incoherent light, as for example sunlight or halogen lamps, the light distribution is linear in intensity with respect to the wavelengths [65]. Therefore, the intensities were calculated in 25 steps of 12.5 nm within the visible region of 400 – 700 nm

and were added up (*eq. 32*), which was reported to yield an accurate white light performance [66]. As the refractive index for commonly used lens glass substrates (e.g. quartz, PMMA) does not change more than 1% inside this spectrum, it was assumed to be constant.

$$I_{wl} = \sum_{\lambda} I_{\lambda} \quad (32)$$

The performance of the QM design using this white light simulation is given in *figure 36*. For comparison, the axial intensity distribution of the reference lens (dotted line) and of the monochromatic illuminated QM (dashed line) is presented. The QM illuminated with white light (solid line) has an axial gain of 5.9 and a Strehl ratio of 0.09. Under white light illumination, the intensity distribution of the QM filter shows a homogeneous axial distribution in addition to the constant transversal spot size (*fig. 37*).

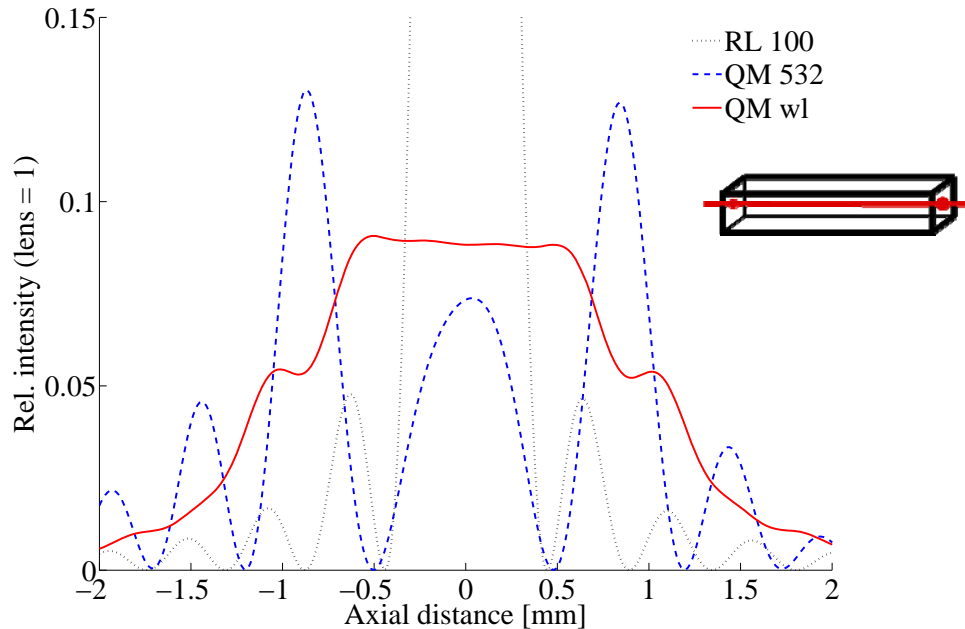


*Fig. 36: Simulated axial intensity distributions: reference lens with  $f = 100$  mm (RL100: dotted line), the Quartic Multiplex with monochromatic illumination (QM 532: dashed line), and the QM with white light illumination (QM wl: solid line).*

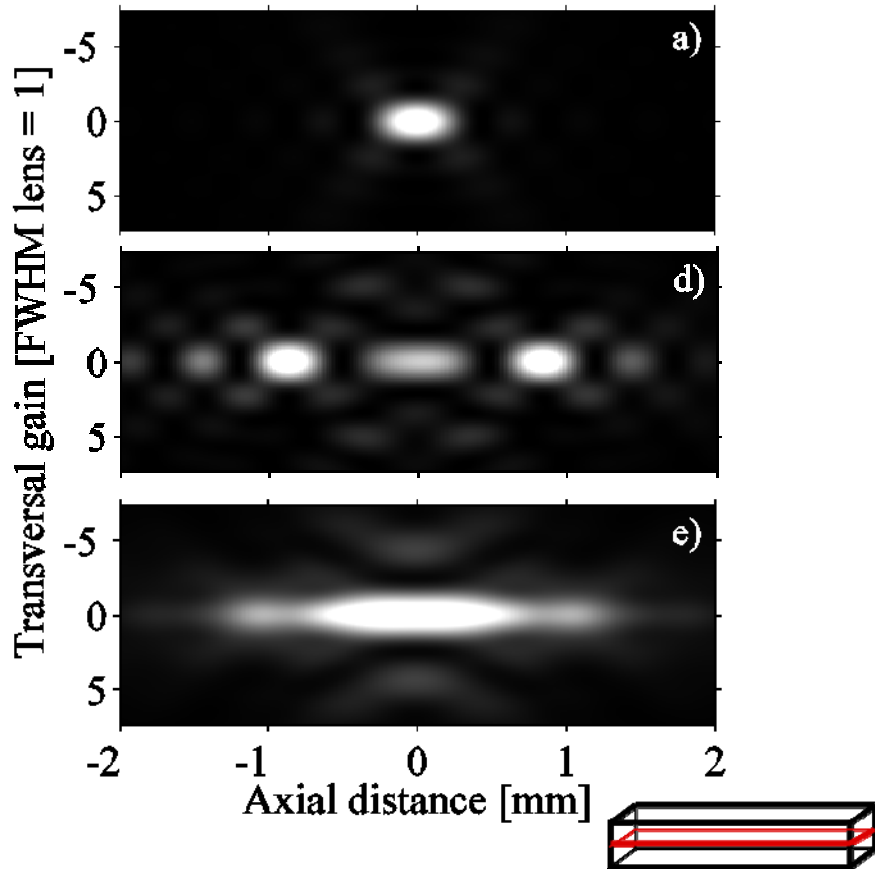


*Fig. 37: Simulated 3D intensity distribution for a) the reference lens; d) the QM monochromatic illuminated and e) the QM with white light illumination.*

### 3.7. Conclusion

We designed our Quartic Multiplex phase-only pupil filter by combining two opposite quartic phase functions with equal DOF in a radially multiplexed manner. Although this filter has a rather simple structure, it generates a homogeneous transversal spot over the extended DOF with a near diffraction limited resolution. With simulations and measurements of the PSF, we have shown its performance and effectiveness for a focusing lens.

At this stage of work, we assumed that the extended DOF method would work for standard white light imaging. From additional studies, finite distance imaging and white light performance was proven. The next step was to implement the DOF filter into an imaging system to study the performance under non-paraxial rays. Investigations in a complete aberration and performance analysis will lead it further to a final implementation.

For the field of ophthalmology, additional investigations need to be done. In the daily vision of the human eye, the opening of the iris changes under different brightness of the surrounding light. Multiplexing the pupil area inhibits the loss of performance when the iris reduces at bright light. For two zone filters, the outer zone is unused in that case. The advantage of our Quartic Multiplex over fully diffractive structures lies in the few step-like structures, reducing scattering that might introduce blur and background light. With its piecewise continuous phase function, we reduce the halo effects that can occur from full diffractive structures and still provide the desired extension of the DOF at high and low brightness.

A first prototype IOL was fabricated in PMMA with a diamond-turning milling machine by one of the partners of the CTI project. However, due to difficulties that the milling machine had with the step features, the performance was not satisfactory and production was abandoned. A different type of production is needed to fabricate the steep edges and curved surfaces in between. In addition, thick lenses in off-axis illumination suffer from primary aberrations like spherical aberration, coma, astigmatism, field curvature, distortion and chromatic aberration depending on the lens shape [67]. This has also to be considered for production of a test lens. Furthermore, medical considerations as infections arising from diffractive structures in the eye environment and concrete implantation procedures have to be examined.

## Chapter 4

# Correction of Spherical Aberrations in Focusing Applications

Specimen induced spherical aberrations are known to severely degrade the point spread function (PSF) of high numerical aperture (NA) systems in imaging and focusing applications. A planar refractive index mismatch is introduced by a suspension medium, a glass cover slide or when imaging into a thick transparent specimen. Thereby a focus shift and spherical aberrations are introduced. This reduces image contrast and transversal resolution and degrades the depth of focus [68, 69].

In order to correct the object induced spherical aberrations, we provide a new method to characterize the unknown planar medium first and then use this information for a phase correction of the wavefront [70]. The basic concept is compared to the state of the art first (*chap. 4.1*). The mathematical background for the characterization of the medium is given in *chapter 4.2*. The basic focusing set-up presented in *chapter 2.3* was slightly modified to perform the experimental proof of the method (*chap. 4.3*). The experimentally obtained results for different glass plates, which are used to model the planar refractive index mismatch, are compared to the known values for accuracy estimations (*chap. 4.4*). We also show that our method allows getting good results even if the lens system is not diffraction limited, but includes aberrations

(*chap. 4.5*). In order to simplify the integration of the method into a focusing system, we performed a study to use the same phase SLM device for the characterization and the correction (*chap. 4.6*). Finally, we present the results for correcting the spherical aberrations (*chap. 4.7*) together with an investigation of accuracy (*chap. 4.8*).

### 4.1. State-of-the-art of aberration correction

Several correction methods have been proposed to eliminate spherical aberrations. They include correcting the focus shift by using an adjustable path length in optical coherence tomography [71], objective coupled illumination in microscopy [72], wave front corrections of the scanning beam in two-photon microscopy [73] or changing the microscope conditions by changing the immersion oil, tube length, objective or cover glass thickness [74, 75]. For an unknown aberration inducing medium, iterative processes with adaptive feedback loops have been considered. Such adaptive aberration corrections contribute to optimizing the image quality without the *a priori* knowledge of the characteristics of the aberration source [76-79]. For *a priori* known parameters of the aberration inducing medium, i.e. the refractive index and the physical thickness, best results are obtained from geometrical calculations of the path length difference [80-82].

In order to characterize the medium, a standard measurement of the physical thickness and refractometry to obtain the index of refraction can be used for large, removable objects such as glass slides or fluids. Thereby unwanted alterations can occur in the sample when changing from the characterization system back to the application. Furthermore, if the medium is a part of the specimen under investigation or the sample is prepared and fixed with the aberration inducing medium, these techniques do not work, and a different set of characterization methods has to be applied. Since two measurands need to be quantified, at least two measurements under different conditions or two independent measurement systems are needed. The optical thickness can be measured with interferometric methods such as digital holographic microscopy. However, the optical thickness, being the product of the physical thickness and the refractive index, cannot be separated without an additional measurement or knowledge of one of the quantities. An independent measurement of the physical thickness can be obtained, for

example, with tomography [83] or with a reflective confocal measurement system [84]. By assuming a spherical shape of cell structures [85] additional information is gained by letting single cells flow through microchannels [86] or Fabry Perot cavities [87]. To our knowledge, only a few methods yet exist, which can extract the physical thickness and the refractive index simultaneously in a microscopic arrangement. Ellipsometry is able to analyze thin films [88], white light interferometry obtains the group index and thickness of transparent media [89, 90] and a Mach-Zehnder multiwavelength interferometer can generate a 2D map of the refractive index distribution and the thickness profile [91]. Further, an equivalent approach was reported whereby the immersion medium of a digital holographic microscope was changed to obtain a set of optical thickness maps, from which the refractive index and physical thickness was calculated [92]. The disadvantage of all these methods is that they involve an extensive additional measurement system before the target application of focusing or imaging can be improved.

We propose a method based on a phase-only spatial light modulator that first characterizes the aberration inducing medium in-situ and then corrects the spherical aberration directly in the system. To obtain both the physical thickness and the refractive index of the medium, we measure the induced focal shifts for paraxial and marginal rays with large angle. The angle dependence of the optical path difference inside the medium is given by the quartic phase function, the inverse of which is needed for correction. We demonstrate the method using a microscope objective with a numerical aperture of 0.3 and plates of different glasses to model the aberration inducing refractive index mismatch. The obtained measurement accuracy of 3 % is sufficient to compensate the spherical aberration completely. An axial elongation of the depth of field by a factor of 5 due to spherical aberration was fully corrected by the phase-only SLM.

With this unified set-up, we can characterize the spherical aberrations induced by the medium in-situ, and then correct it with an integrated phase SLM in the very same lens system that is used in the imaging or focusing application. The sample does not need to be moved or remounted during the complete process.

## 4.2. Characterization of the aberration inducing medium

A planar refractive index mismatch is shown in figure 38. Depending on the propagation direction of the light, this represents a focusing or imaging application. The microscope objective focuses or gathers the light through a glass plate with refractive index  $n$  and thickness  $d$ . Refraction by the glass plate induces a focal shift, which is defined by geometrical optics, i.e. Snell's law. The maximum incident angle  $\alpha_{0 \max}$  is related to the numerical aperture of the objective and the refractive index  $n_0$  of the surrounding medium.

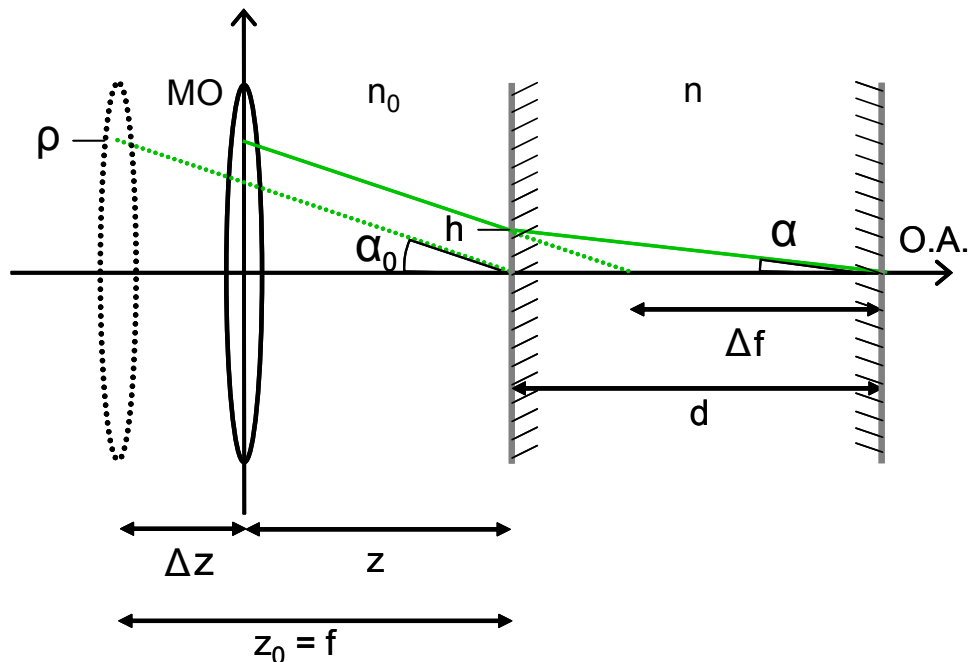


Figure 38: Scheme of a planar refractive index mismatch with thickness  $d$  (MO: infinity corrected microscope objective; O.A.: optical axis). Parameters are explained in the text.

In order to focus into the medium at depth  $d$ , the objective must be brought closer to the interface. From geometrical optics it follows that the new distance  $z$  between the objective and the glass surface is

$$z = \frac{\rho - h}{t_0} = \frac{\rho - d \cdot \tan \alpha}{t_0} = z_0 - d \frac{\tan \alpha}{t_0} \quad (33)$$

where  $\rho$  is the incident beam height in the lens plane with radial symmetry,  $h$  is the intercept height,  $t_0$  is the tangent of the incident angle ( $t_0 := \tan \alpha_0 = \rho/f$ ) and  $\alpha$  is the beam angle after refraction. The  $\tan \alpha$  term can be reformulated using trigonometric relations and Snell's law

so that the axial shift  $\Delta z$  that has to be applied to the objective to focus into the glass at depth  $d$  is obtained by:

$$\Delta z = z_0 - z = \frac{n_0 \cdot d}{\sqrt{n^2 + t_0^2 (n^2 - n_0^2)}} \quad (34)$$

The focal shift  $\Delta f$  itself is then given by

$$\Delta f = d - \Delta z = d \left( 1 - \frac{n_r}{\sqrt{1 + t_0^2 (1 - n_r^2)}} \right) \quad (35)$$

where  $n_r = n_0 / n$  is the ratio of the refractive indices. We expand *equation 35* to the second order in  $t_0^2$  and neglect terms of the order  $t_0^6$  and higher. The final equation for the focal shift becomes

$$\Delta f \approx d - dn_r \cdot \left[ 1 - \frac{1}{2} t_0^2 (1 - n_r^2) + \frac{3}{8} t_0^4 (1 - n_r^2)^2 \right] =: \Delta f_{MR} \quad (36)$$

The full *equation 36* has to be considered to describe the focal shift for marginal rays ( $\Delta f_{MR}$ ) with large incident angles occurring in systems with high numerical apertures. In case of paraxial rays, the tangent terms can be neglected, and the focus shift becomes

$$\Delta f_{PAR} := d - dn_r \quad (37)$$

To determine the physical thickness  $d$  and refractive index  $n$  of the medium, we measured  $\Delta f_{PAR}$  and  $\Delta f_{MR}$ . We used a microscope objective with high numerical aperture in combination with a set of apertures allowing for a controllable selection of optical rays. An iris diaphragm that only transmits the paraxial rays is used to measure the focus shift  $\Delta f_{PAR}$ . A dark-field diaphragm with known  $t_0$  that blocks all inner rays and transmits only rays at large angles is used to measure the marginal ray focus shift  $\Delta f_{MR}$ . By dividing the respective equations, the physical thickness  $d$  is eliminated and the resulting *equation 38* can be solved numerically for the refractive index ratio  $n_r$

$$\frac{\Delta f_{MR}}{\Delta f_{PAR}} \approx \frac{1 - n_r \cdot \left[ 1 - \frac{1}{2} t_0^2 (1 - n_r^2) + \frac{3}{8} t_0^4 (1 - n_r^2)^2 \right]}{1 - n_r} \quad (38)$$

After solving for the refractive index  $n$ , the physical thickness  $d$  can be evaluated using the paraxial focus shift  $\Delta f_{PAR}$  (*eq. 37*).

In summary, we are able to determine the refractive index and the physical thickness of an unknown planar medium. Two independent measurements are taken based on the non-linear dependency of spherical aberration on the incident angle. Using geometrical optics we are able to relate the refractive index and the physical thickness of the planar medium to the focus shift of rays with different angles [70].

### 4.3. PSF Measurement system

The experiments are performed with a home-built PSF measurement system (*chap. 2.3*). We used a 10x microscope objective with NA of 0.3 and infinity correction from Nikon to focus the light at a distance of 10 mm. The distance between the SLM and the 10x objective was set to 60 mm, the shortest possible in this configuration. Another MO was used to magnify the PSF with a magnification of 100x and much larger NA of 0.9. For the planar refractive index mismatch, we introduce different glass plates (Thorlabs) between the two objectives: calcium fluoride ( $\text{CaF}_2$ ,  $n = 1.43$ ,  $d = 5.25$  mm), BK7 ( $n = 1.52$ ,  $d = 5.35$  mm), sapphire ( $\text{Al}_2\text{O}_3$ ,  $n_{ord} = 1.77$ ,  $d = 5.00$  mm), and a quartz glass ( $n = 1.52$ ,  $d = 8$  mm). Their refractive indices were identified at a wavelength of 532 nm. Their thickness was measured with a calliper with a measurement accuracy of 0.05 mm, which corresponds to 1 % of the thickness  $d$ . Each glass plate was evaluated independently to determine the measurement accuracy of our method. It is important that the focused beam travels completely through the glass to ensure the full thickness effect. This also avoids spherical aberrations or scattering at the backside, which might influence the observation by the 100x MO.

Three different apertures were used to vary the incident angles. They were placed directly before the focusing 10x MO. The aperture allowing for full field illumination (FF) comprises

the full lens diameter ( $\rho = 1$ ). Paraxial illumination (PAR) is generated using an iris aperture with normalized radius of 0.2, while marginal rays (MR) at large angles are obtained with a ring aperture with inner and outer normalized radii of 0.9 and 1, respectively. The apertures were produced by first depositing a silver film on a glass plate and then by removing it from the respective regions by UV laser ablation (Fig. 39). With each aperture, the intensity peaks were measured through the focus and fitted by a Gaussian function to obtain the position of the maximum, followed by the determination of the axial focus shift.



*Fig. 39: Three different apertures to modulate the incident angle. Left: FF, middle: PAR, right: MR.*

Beside the focal shifts obtained with the different apertures, the actual tangent value  $t_0$  of the incident angle for the MR ray has to be known to obtain the refractive index (eq. 38). It turned out that the results are very sensitive to the value of  $t_0$ . Therefore, the actual value of the tangent  $t_0$  for the MR aperture was measured in the far-field (fig. 40). For that purpose, the magnifying 100x MO was removed and replaced by the camera. The stage moved the camera along the optical axis to capture the spot size of the different apertures until they fill the detector chip. From the known travel distance and pixel size of the camera, the tangent of the angle was calculated.

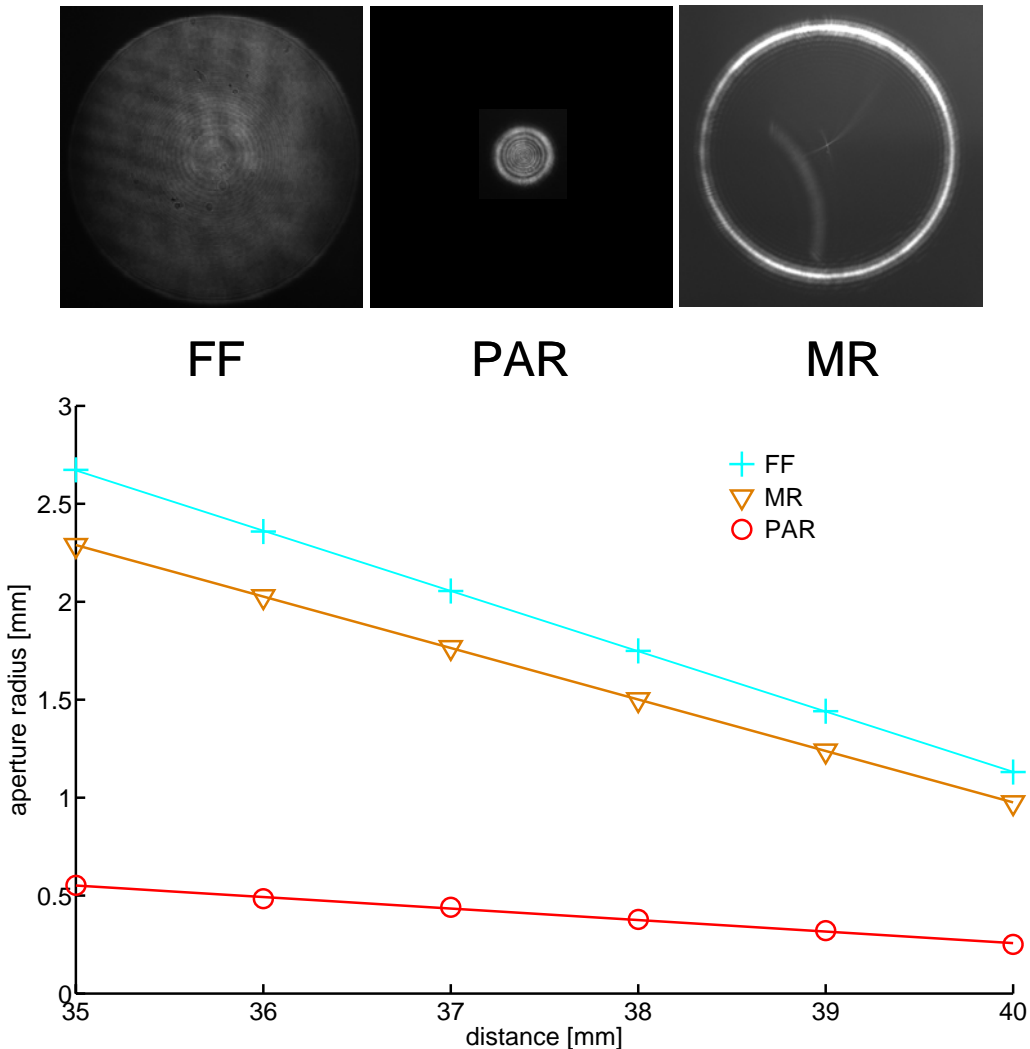


*Fig. 40: Tangent measurement in the far field for the three apertures. Top: Images at one position (FF: full field, MR: marginal rays, PAR: paraxial rays).*

Having measured the incident angle in the far-field for the three apertures relative to FF, MR and PAR illumination, a linear dependency between the tangent  $t_0$  and the radius  $\rho$  in the 10x MO input plane was obtained (fig. 41). The gradient parameter for the normalized aperture radius was  $\rho = 3.20 t_0$ . This results in a maximum tangent value of 0.313 for the maximal radius of 1, representing a numerical aperture of 0.299. This is in excellent agreement with the specified NA of 0.3.

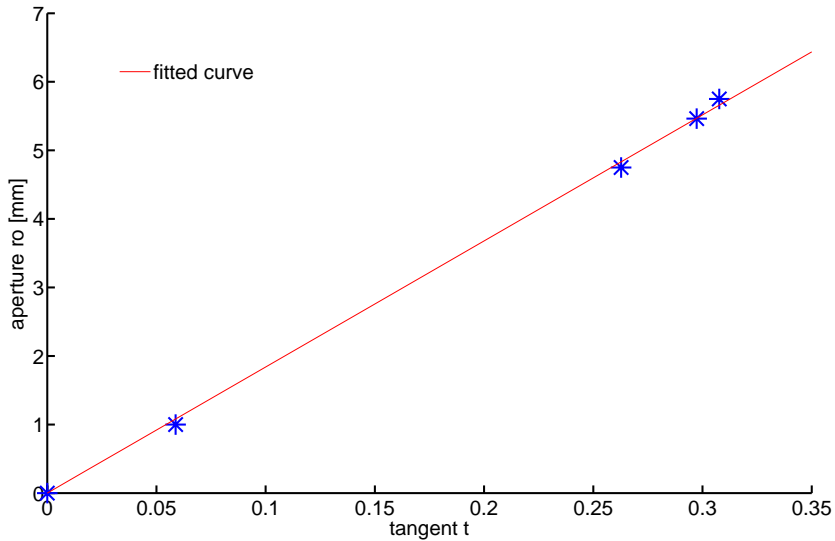


*Fig. 41: Linear dependency of the tangent and the aperture of the MO input plane.*

#### 4.4. Results for the glass plates

The axial intensity distribution obtained for each of the three apertures is presented in *figure 42*. The maxima of the reference peaks (*fig. 42 left*), i.e. the ones obtained with the objective used in air, are given for the apertures associated with FF, MR and PAR illuminations. They are almost at the same position, indicating that the objective is well corrected for spherical aberrations. The peaks for PAR and MR illuminations are wider as compared to the one obtained for FF illumination, as the apertures reduce the effective NA. The CaF<sub>2</sub> FF measurement contains spherical aberrations, which in our case contributes to the widening of the axial width by a factor of 2 and introduces a fine structure (*fig. 42 right*). The peaks for the PAR and MR illuminations are separated, each lying at one end of the FF intensity distribution. The focal shift for the MR illumination is larger, which is consistent with *equation 35*.

The characterization results for all glass plates are summarized in *table 5*. Inserting the results into *equation 38* and solving by Matlab led to the values of the refractive indices and the physical thickness of the glass plates. From the focal shifts measured for the PAR and MR illuminations, the calculated values for the refractive index and the thickness are presented together with the percentage deviation.

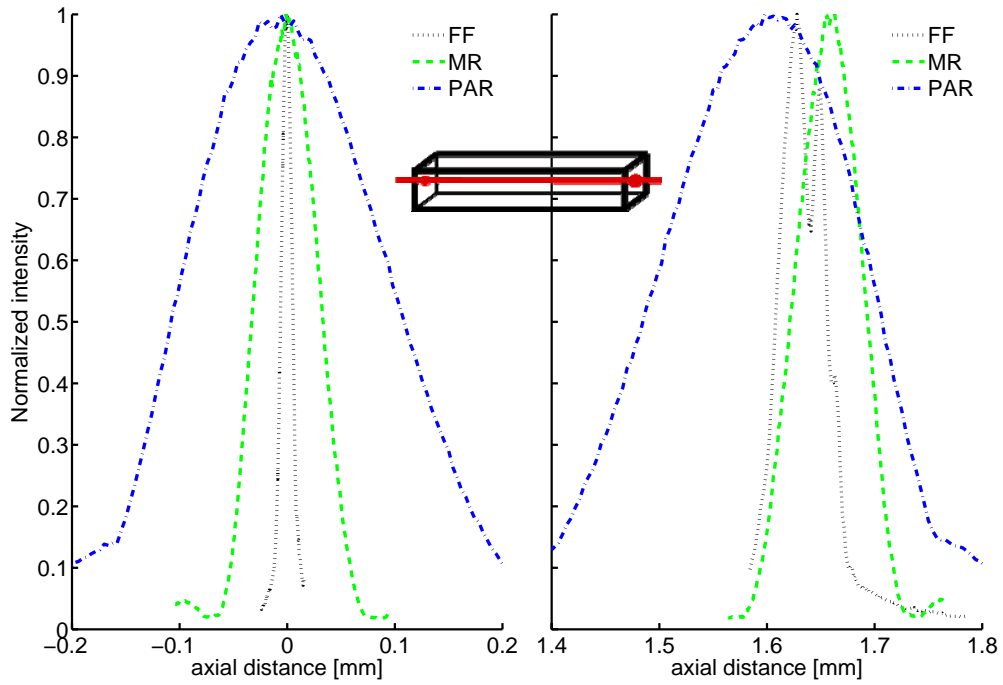


Figure 42: Axial intensity measurement results for the reference lens (left) and for CaF<sub>2</sub> (right). (FF: full field illumination, MR: marginal ray aperture, PAR: paraxial iris aperture)

**Table 5:** Results for different glass plates obtained with a 10x MO, NA 0.3 system.

	CaF <sub>2</sub>	BK7	Quartz	Sapphire
n (532 nm)	1.453	1.519	1.520	1.770
d (calliper) [mm]	5.25	5.35	8.00	5.00
$\Delta f_{\text{PAR}}$ [mm]	1.5969	1.8092	2.7671	2.1757
$\Delta f_{\text{MR}}$ [mm]	1.6760	1.8944	2.8439	2.2377
n (calculated)	1.454	1.506	1.534	1.812
% dev	+ 1.3 %	- 0.9 %	+ 0.9 %	+ 2.4 %
d (calculated) [mm]	5.12	5.38	7.95	4.86
% dev	- 2.5 %	+ 0.7%	- 0.6 %	- 2.9 %

The transversal FF focal spot size of the reference was measured to be 1.0  $\mu\text{m}$ , while the Rayleigh resolution of a NA 0.3 system predicts it to be 0.9  $\mu\text{m}$  at 532 nm wavelength. The

measurement value is close to the theoretical value, indicating that the set-up is operating close to the diffraction limit, which is also seen by the fact that the paraxial as well as the marginal rays are focused at almost the same axial position. Our measurements of the axial position of the maximum intensity are reproducible to half a micrometer, which is equivalent to introducing less than half a percent of error to the calculated values of the refractive index and physical thickness of the glass plates. Comparing the measured results with the known values, we obtain a measurement accuracy of better than 3%.

#### **4.5. Measurement results for an aberrated system**

We have also tested the method in systems that are not aberration free. In this case it is important to measure the focal shifts for each type of aperture relative to the respective reference measurement, i.e. the focus shifts of the PAR and MR illuminations are measured relative to the focal position of the PAR and MR values of the reference, respectively. Then, the resulting shifts represent the additional effect of the refractive index mismatch, because the system aberration is apparent in the shifts of the PAR and MR peaks of the reference (*fig. 43*). To induce aberration into the system, a finite 10x objective from Nikon for 160 mm DIN tube length was illuminated from infinity. Since this changed the NA compared to the normal usage, the illumination angle had to be measured beforehand in the far-field. The results using this system yielded an accuracy of around 2-3 % for the evaluation of the refractive index and the physical thickness. It thus proves that it is possible to characterize the additional aberration source independently from the aberration inherent in the optical system.

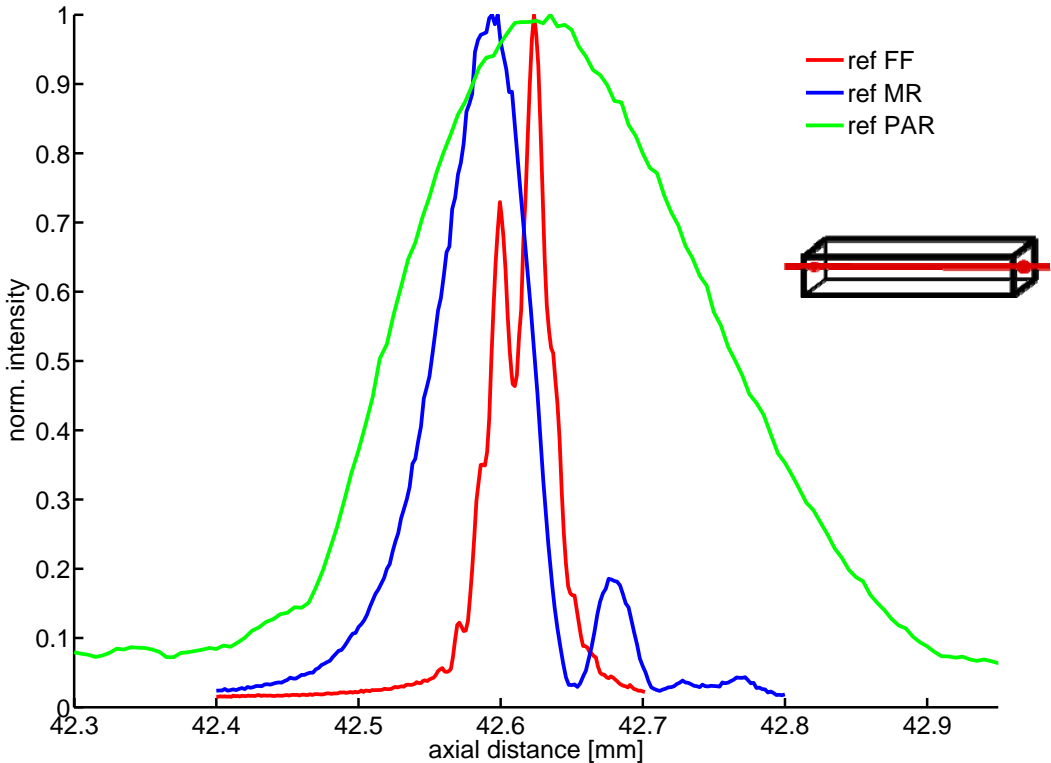


Fig. 43: Axial intensity measurement of the reference for an aberrated system, represented by a double peak of the FF intensity distribution.

#### 4.6. Aberration correction with a phase SLM

After obtaining the necessary information on the medium an aberration correction is performed. The main idea is to convert the angle dependency of the focal shift to a radial dependency of the wavefront correction within the pupil plane. As the phase SLM is limited to a modulation depth of  $2\pi$  radians, we cannot compensate for the full focal shift but only for the spherical aberration. We thus subtract the paraxial focal shift from the full focal shift for large angles (eq. 38). In this case, only the angle dependent component of spherical aberration remains (eq. 39).

$$\Delta f_{MR} - \Delta f_{PAR} = \frac{d}{2n} t_0^2 \left(1 - n_r^2\right) - \frac{3d}{8n} t_0^4 \left(1 - n_r^2\right)^2 \quad (39)$$

To obtain the corresponding phase correction, the focal shift difference has to be multiplied with the wave number  $k$  and the difference of the refractive indices;  $\varphi(\rho) = k(n-n_0)(\Delta f_{MR} - \Delta f_{PAR})$ . Converting the tangent of the incident angle to a radial dependency,  $\rho = 3.20 t_0$ , (see *chap. 4.3*) leads to the phase modulation function (*eq. 40*).

$$\varphi(\rho) = \frac{\pi d}{\lambda} (1 - n_r) \left( \frac{\rho^2}{3.2^2} (1 - n_r^2) - \frac{\rho^4}{3.2^4} \frac{3}{4} (1 - n_r^2)^2 \right) \quad (40)$$

Comparing the terms with Zernike's coefficients (*chap. 1.2*), we note that while the square term induces a simple focus shift, the term containing the radius to the power of four represents the third order spherical aberration. We again ignore the pure focus shift and only correct the spherical aberration term with our phase SLM, after wrapping the phase function to the interval  $(0, 2\pi)$ .

We demonstrate the correction of the spherical aberration for a  $7.95 \pm 0.05$  mm quartz glass with refractive index of 1.534 (see *table 5*). The full 3D intensity distribution for the FF illumination is shown in *figure 44* for three settings: focusing through air (*fig. 44a*), through the glass plate (*fig. 44b*), and idem with the spherical aberration corrected with the SLM (*fig. 44c*). The reference PSF has a depth of field of 13  $\mu\text{m}$ . After introducing aberrations from the 8 mm thick quartz glass, the depth of field was increased to 66  $\mu\text{m}$ , which represents an axial gain factor of 5. By applying the aberration correction obtained from the focal shifts, we were able to compensate for the spherical aberration completely and obtained again a PSF with a depth of field of 13  $\mu\text{m}$ .

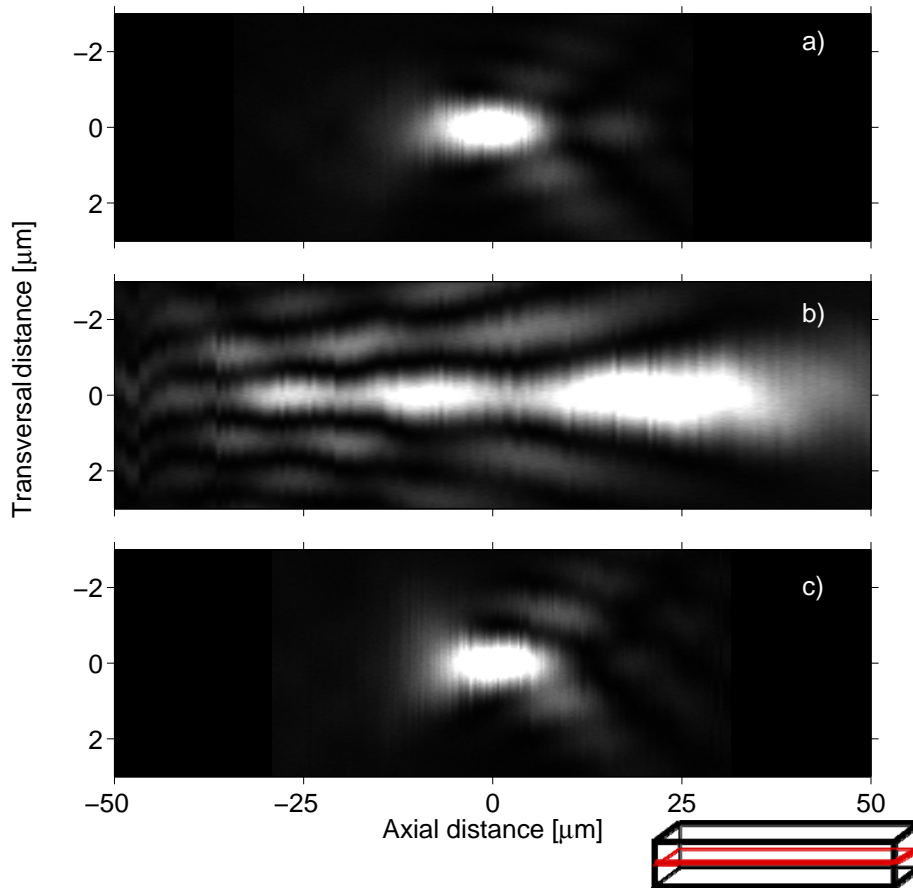
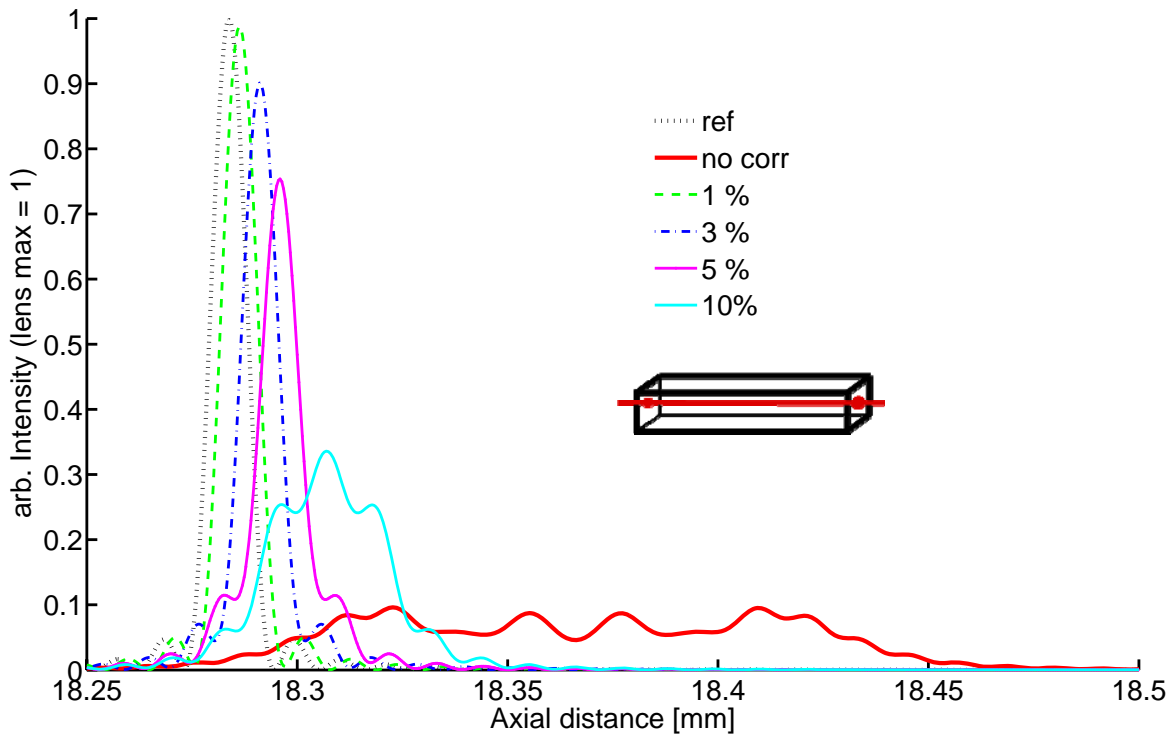


Figure 44: 3D PSF measurement results in FF illumination for focusing through a) air, b) quartz glass, c) quartz glass with aberration correction.

#### 4.7. Accuracy estimation based on numerical simulations

An accuracy estimation of the correction had to be performed, because the characterization of the aberration source contained a deviation of around 3%. To investigate in the outcome of a slightly wrong correction, we performed numerical simulations with the tools presented in chapter 2. We took the reverse approach by starting with a completely perfect correction, represented by the usual reference lens. To simulate a wrong correction, we added a spherical aberration term as a pupil filter from equation 40. We investigated in the axial intensity distributions for a simultaneous deviation of the refractive index and the thickness of up to 10 %. A deviation of 100 % represents the case where no correction is applied and is in good agreement to the measurements shown in previous sub-chapters. Two cases have to be examined. First, the deviation occurs in the same direction, meaning that both values are larger or

smaller than the actual real value (*fig. 45*). In this case, the ratio  $d / n$  is unchanged. Second, the deviations occur in the opposite direction, such that one is larger while the other one is smaller than the real value. Apparently, we have only found the latter situation in the experiment, and the simulations were thus adjusted (*fig. 46*). The numerical simulations showed that a thickness and refractive index accuracy of up to 5 % is good enough to compensate more than 95 % of the spherical aberration.



*Fig. 45: Axial intensity distributions with incomplete correction functions in same direction.*

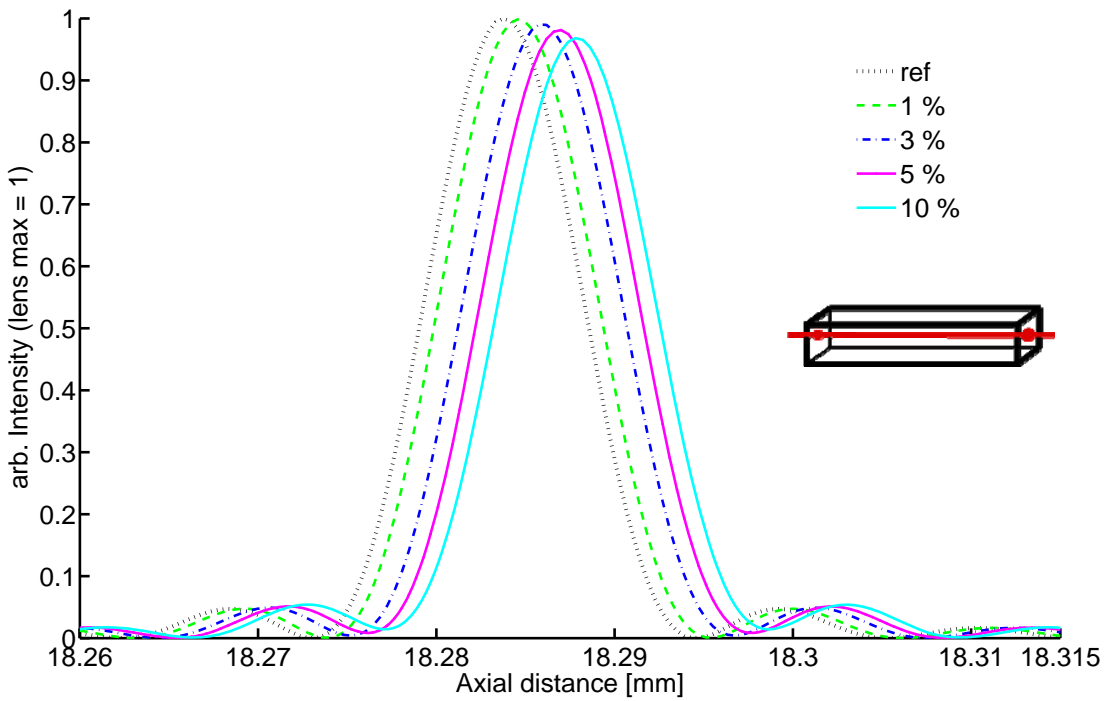


*Fig. 46: Axial intensity distributions with incomplete correction functions in opposite direction.*

#### 4.8. Conclusion

We have described a new dual step method based, respectively, on a controllable selection of optical rays (paraxial or marginal) and a phase-only spatial light modulator for measuring and correcting spherical aberrations induced by an unknown medium between lens and object of interest, for example, in a microscopic setup. We have considered a planar refractive index mismatch in a focusing PSF measurement system with a numerical aperture of 0.3. We use the different behaviour of paraxial rays compared to marginal rays with large angles to obtain two focus shift measures, which then are used to evaluate the refractive index and the physical thickness separately. From these characterization results, the phase correction to compensate the spherical aberrations is obtained. The method is reliable, does not require the remounting of the sample, and the aberration inducing medium can be characterized *in situ*. Depending on the application, either the focus shift  $\Delta f$  for focusing or the objective shift  $\Delta z$  in imaging can be measured.

The restriction of this method is that the introduced spherical aberration must be large enough to separate the PAR and the MR intensity position significantly. If, however, the difference between the PAR and MR rays is very small, almost no spherical aberration is present and correction is not needed. The remaining few per cent inaccuracy of our characterization results may arise from the manual positioning of the glass plates and the apertures or from inhomogeneities in the laser illumination or within the glass plates. However, the measurement accuracy is more than satisfactory to compensate the spherical aberration with the appropriate correction function.

Another significant advantage of the method lies in its intrinsic ability to work accurately for systems with much higher numerical apertures. With an increased maximum incident angle, the tangent term becomes more pronounced. Therefore, spherical aberrations introduce crucial PSF degeneration even for much smaller differences of refractive index and medium thickness. The system becomes more sensitive to a refractive index mismatch. In addition, this aberration setup can be combined with other aberration corrections, for example asymmetric aberrations as coma or distortion.

Further studies are needed to characterize and improve the system in imaging applications. Some will be presented in *chapter 5*. Problems while implementing it into an imaging system, e.g. a microscope, might arise regarding precise positioning of the modulation element, off-axis beams, examinations of real samples and their imaging quality. Even a more compact in-situ system can be realized with apertures generated directly with the SLM, allowing for characterization and correction of the spherical aberrations by only controlling the modulator (*chapter 5.3*).

#### 4. Correction of Spherical Aberrations in Focusing Applications

# Chapter 5

## Adaptive Optics Implemented in Microscopy

In this final chapter, the theories and applications of the previous chapters for modifying the PSF of a focusing laser beam were collected and implemented in an imaging setup. To obtain comparable data, the same 10x Nikon MO with numerical aperture of 0.3 was used as the imaging objective together with the liquid crystal phase modulator, assembled in an infinity-corrected model microscope (*chap. 5.1*). To characterize the system, different kind of standardized imaging targets were used.

As first application, an evaluation of the imaging performance of the different phase modulation designs for an extended depth of field (DOF) was done (*chap. 5.2*). An evaluation of the modulation transfer function (MTF) and the behaviour of the contrast while defocusing were performed for a quantitative characterization. To validate the method for real biological applications as cell microscopy, water fleas (*Daphnia galeata*) were imaged with the extended DOF lens system.

The second application was split into two main tasks: The in-situ characterization of an unknown planar refractive index mismatch and the consecutive correction of spherical aberrations induced by the medium. The phase modulation and the basic concept of obtaining the refractive index and physical thickness of the unknown medium are presented in *chapter 5.3*. Subsequently, the aberrations induced by imaging through a glass plate were analysed on the

basis of image contrast and quality. An aberration correction was then performed in-situ with the phase modulator (*chap. 5.4*) very similar to the results obtained in *chapter 4*.

### 5.1. Setup of the model microscope

A model microscope was built with an implemented phase spatial light modulator (SLM) with the same optics as presented in *chapter 2.3*. The setup consisted of three main parts: the illumination, the object beam and an additional laser beam for alignment and calibration (*fig. 47*).

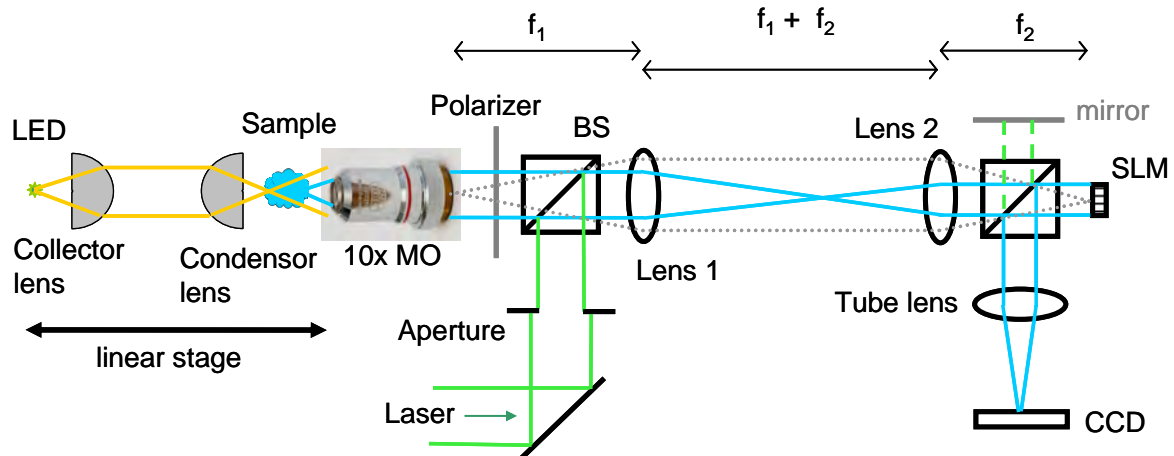


*Fig. 47: Schematic drawing of the microscope setup. The three main light beams are: sample beam (blue), LED illumination beam (yellow) and an expanded laser beam for adjustment and calibration (green). [MO: microscope objective, BS: beam splitter, SLM: spatial light modulator, CCD: camera]*

The main idea was to optically overlay the SLM onto the exit pupil plane of the microscope objective (MO) with a telescope arrangement (dotted gray line) in a standard infinity distance microscope (compare with *fig. 6* in *chapter 1.4*). The telescope lenses 1 and 2 projected the SLM plane to the correct position, if the SLM and the exit plane of the MO were positioned in the focal planes of the respective lenses. In addition, the focal lengths were chosen differently to reduce the object beam diameter to the size of the active area of the SLM (blue line). To maintain a collimated beam after the telescope part, the telescope lenses had to be separated by a distance equal to the sum of the focal lengths. In that case, the distance between the op-

tics was given and could not be modified after the choice of the optical design. The tube lens finally focused the object beam and generated the image on the camera. A polarizer introduced within the object beam was needed for a phase-only performance of the SLM. The illumination consisted of a green LED, whose diverging beam was collected by a lens and then focused on the sample with a condenser lens in a Köhler kind of illumination (yellow line). The illumination was mounted on a linear stage together with the sample to maintain a constant illumination. The additional laser beam was used to align the telescope and tube lenses and to assign the required illuminated region on the SLM (green line).

Three different samples were used to show the effectiveness of the applications with this microscopic arrangement (fig. 48). The standard USAF1951 resolution target was used for the characterization of the imaging performance. For a more detailed analysis over the full image field, the size and distribution of the individual features was not satisfactory. With this target, asymmetric imaging performances, for example inhomogeneous distortions of spherical aberration, were impracticable. To cover these cases, a grating with 80 line pairs per millimetre (lp/mm) was used instead, which corresponds to the 3<sup>rd</sup> element of the 6<sup>th</sup> group of the USAF1951 target. The constant size of the lines over the complete image field helped immensely in evaluating the overall imaging performance. Finally, juveniles of *Daphnia galeata* were used as biological example to prove the usefulness of the method for real biological samples.

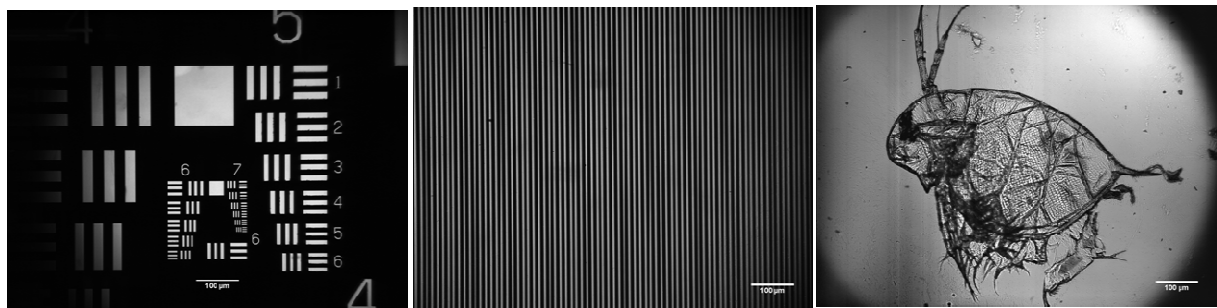


Fig. 48: Imaging samples used (left: USAF1951 target, middle: grating with 80 lp/mm, right: *Daphnia galeata*); the scale bar is 100  $\mu\text{m}$ .

### 5.1.1. Alignment of the microscope

A detailed description of the used optics with all important measures, the alignment procedure and the optical characterization of the model microscope are given below:

#### Optics used in the system

A green LED with a wavelength of 532 nm was used as almost incoherent illumination source as requirement for the SLM to work in phase-only modulation. An aspheric lens with focal length of 45 mm was used as collector. To match the illumination angle to the imaging angle, the condenser lens and the imaging MO had both a 10x magnification with a NA of 0.3. To be sure that the illumination covers the full imaging field, a Mitutoyo 10x MO (BD Plan Apo) with large field size was used. Because the illumination was moved together with the sample on the linear stage, a good illumination angle was obtained even for large defocus positions, as needed in the high depth of field application. The same Nikon 10x infinity MO from the previous focusing applications was used as imaging objective to maintain consistency and comparability of the results. The object beam emerging from the imaging objective had a diameter of 11.5 mm, while the active area of the Pluto SLM from Holoeye was 20x10 mm. The lenses of the telescope were aspheric doublets to maintain a good diffraction limited imaging with focal lengths of  $f_1 = 150$  mm and  $f_2 = 100$  mm. This reduced the size of the beam diameter after the telescope to  $11.5 * f_2 / f_1 = 7.66$  mm, a good size to fit on the SLM without alignment difficulties. A detailed description and calibration of the SLM was already provided in *chapter 2.3.1*. Another aspheric doublet with 100 mm focal length was used as tube lens to form a picture on the Prosilica camera.

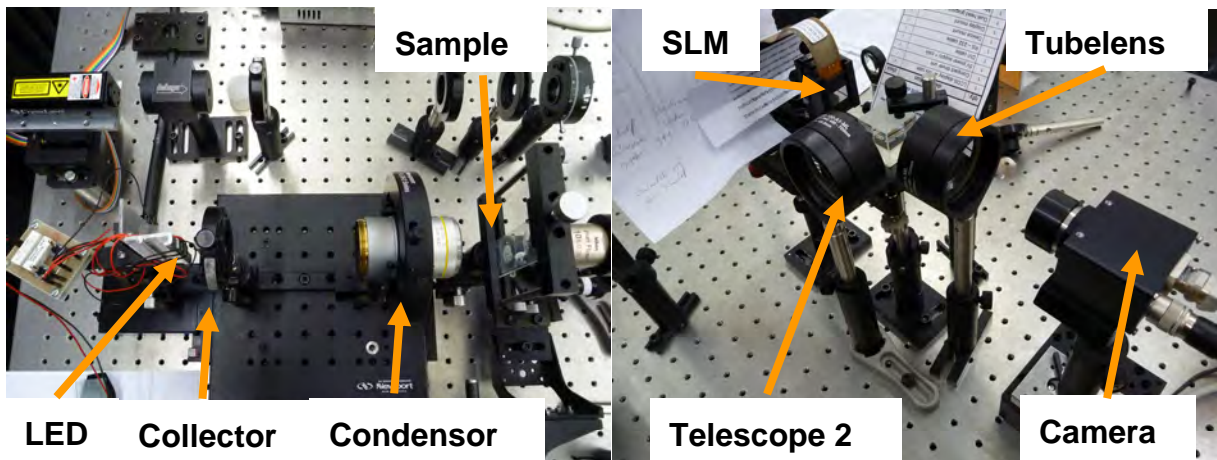


*Photo 3 left: illumination part; right: SLM modulation and detection part.*

#### Alignment procedure

A precise alignment of all the optics was crucial to obtain a diffraction limited imaging system. To obtain the desired phase modulation folded back to the exit pupil plane of the imaging MO, the distances between the optics and the field assignment on the SLM had to be adjusted properly. This complex task was simplified by introducing an additional laser beam for the alignment procedure.

In a first step, the imaging MO, the first beam splitter (BS) and the telescope lens 1 were placed at the right position. The collimated laser beam was set to the height of the MO opening and adjusted perpendicular to the BS. The telescope lens 1 could be easily mounted at the right tilt, position and height to focus the beam without divergence, while the telescope lens 2 collimated the laser beam again. The second BS, the spatial light modulator (SLM) and the reference mirror were introduced perpendicular and centred to the laser beam at the designed distance. Special care had to be taken to apply already the flatness correction to the SLM as described in *chapter 2.3.1*. Otherwise, the reflected beam became pre-focused and the further alignment steps became inaccurate. The tube lens and the camera were added such, that the laser beam was exactly focused on the camera. The laser intensity had to be reduced to avoid saturation. The reflection of the laser beam at the SLM was used to position the imaging MO exactly within the optical light path on axis and at right distance to the telescope lens 1. The remaining adjustment of the tilt of the MO could not have been done at this stage before the

alignment of the illumination part. The laser beam was then adjusted to the exact size of the MO opening with an aperture. The last step to assemble the imaging part of the infinity corrected microscope was to assign the active region of the SLM.

The illumination should match the imaging resolution to obtain a diffraction limited imaging system. Therefore, another MO with numerical aperture (NA) of 0.3 was used as condenser lens. To collect the light from the LED source, it was placed at the focus of a lens with short focal length. With a perfect optical alignment of the MOs, there was an overlap between the image of the sample and the image of the LED, disturbing the performance. In a Köhler illumination system, the image of the LED would be projected to the Fourier plane of the sample position, resulting in a homogeneous illumination. This is obtained by varying the distance between the LED, the collector and the condenser lens. Physically, every point of the LED illumination is completely distributed over the full sample. However, with our given geometry with a LED chip size of around 1 mm and a MO opening size of the condenser of around 20 mm, the distance between the LED and condenser would have been over 1 meter to fulfil the requirements of Köhler illumination. Therefore, we started at the perfect optical alignment and shifted the condenser lens into the direction of the LED, until the image of the LED was projected at the telescope lens 1 and the tube lens planes. The choice of the Mitutoyo MO with large field size enabled a full illumination of the smaller field size of the imaging MO in this configuration. Having the illumination part adjusted, a step-like adjustment of the tilt of the MO with its alignment to the illumination beam had to be done carefully until the object beam overlapped completely with the alignment laser beam. It was only then ensured that the modulation on the SLM was performed at the right position and distance.

The sample was then introduced on a separate three-axis stage on top of the linear stage of the illumination. A sharp image was obtained on the camera when the object was placed at the exact axial position.

### Characterization of the optical resolution

After assembling and aligning the model microscope, the USAF1951 resolution target was used to characterize the optical resolution. To obtain the MTF of the optical system, the con-

trast of every element on the resolution target was measured and plotted against the number of line pairs per mm (*fig. 49*). Our system was able to image the main groups 5 to 7, which corresponded to 32 – 228 line pairs per mm. The numerical simulation of the MTF was performed with the Matlab tool presented in *chapter 2*, where the transversal PSF of a diffraction limited lens with NA 0.3 was Fourier transformed. Although the higher frequencies were not measurable, the experimental values matched the simulation quite nice at lower frequencies. This indicated a diffraction limited arrangement of the system.

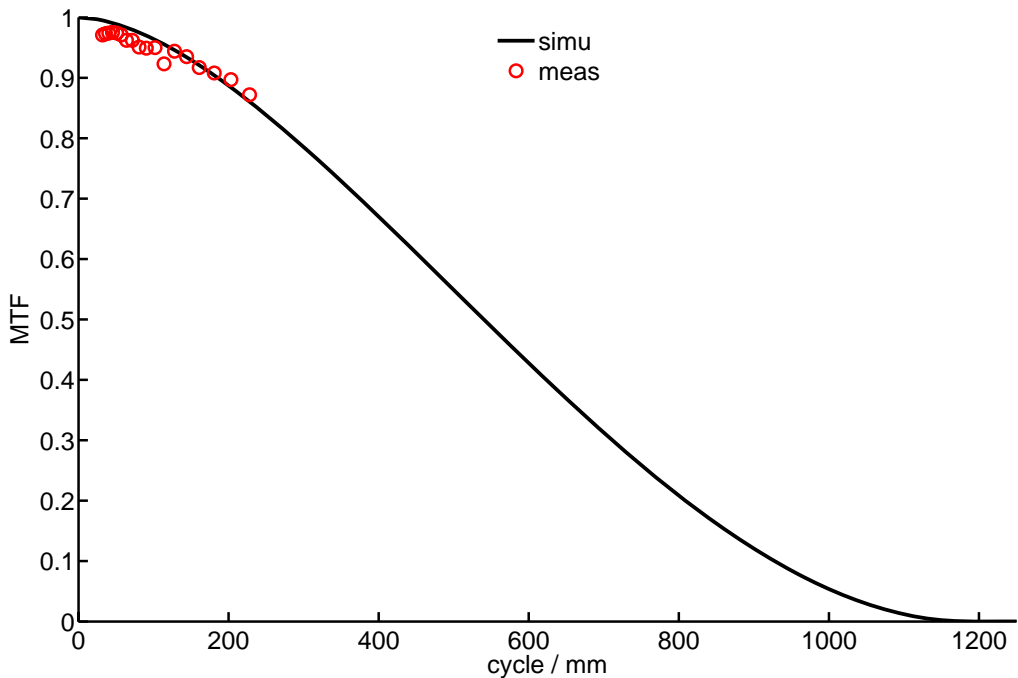


*Fig. 49: Simulated and measured MTF of the optical system with NA of 0.3.*

## 5.2. Extended depth of field

The Quartic Multiplex (QM) function (*chapter 3.4*) was used in the microscopic arrangement to show the performance of an extended depth of field (DOF) in imaging. The same QM lens design from *chapter 3.4* was applied to the SLM phase modulator. To quantify the performance, the 80 lp/mm grating was used to track the contrast of the lines while defocusing (*fig. 50*).

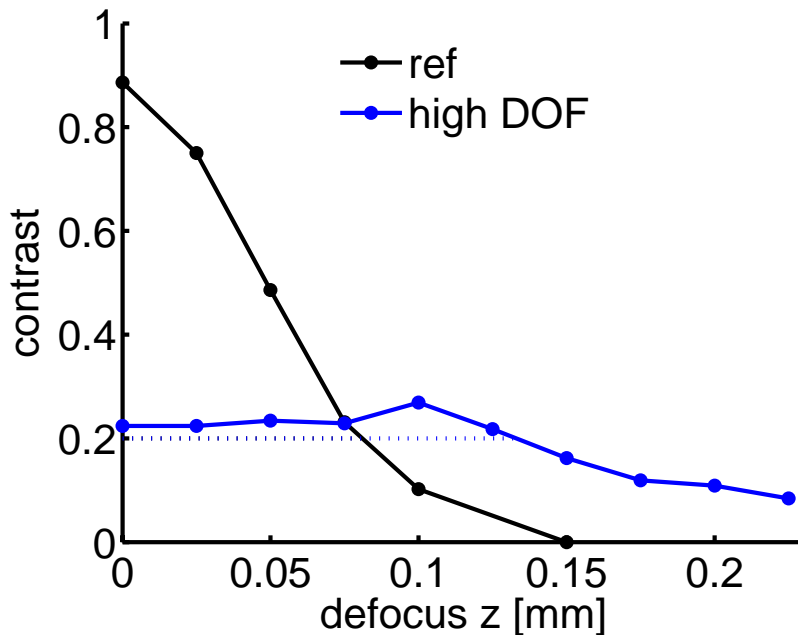


*Fig. 50: Contrast versus defocus position for the 80 lp/mm grating in diffraction limited and extended DOF arrangement.*

The diffraction limited reference was measured without any phase modulation and showed a typical axial PSF. By applying the QM modulation, the contrast at the nominal focal position dropped to 22%. This was expected and already indicated in the 3D intensity distributions of the focusing laser beam with its increased side-lobes (*fig. 32* in *chap. 3.5.2*). However, the contrast remained almost constant over a large defocus length. To compare it with the diffraction limit, we analyzed the defocus position where a contrast value of 20% still remained. The reference contrast fell below 20% at a defocus position of 0.08 mm, while the extended DOF image showed still 20% contrast at a defocus position of 0.13 mm. This is an axial gain of more than 1.5. Furthermore, the picture of the diffraction limited reference contained no more information after a defocusing of 0.15 mm, as the contrast dropped to zero. The picture of the

high DOF lens, however, was still interpretable even for defocusing positions of over 2.5 mm for the 80 lp/mm grating.

In a first experiment, we imaged the antennae of *Daphnia galeata* (*fig. 51*) to show the principle for a real biological three-dimensional object. We obtained a fixed sample of one specimen with two pairs of antennae separated along the imaging axis. First, each antenna pair was imaged separately under diffraction limited conditions (*fig. 51a-b*). From the position of the translation stage we measured a distance between the pair of antennae of 0.16 mm. The pair not in focus was almost unresolved and could only be guessed roughly. However, very fine details could be observed on the focused parts, for instance the fine hairs or small features close to the joints.

The second pair of images was taken with an extended DOF modulation. To match the depth of field to the distance between the pair of antennae, the quartic term was modified until a convincing picture was obtained visually. The raw picture (*fig. 51c*) showed, as expected, a low image contrast. But as intended, both pairs of antennae were clearly imaged. After a simple adjustment of the image contrast and brightness (*fig. 51d*), many details were still recognizable as the fine hair, scars and the extra spine with its fine sub-branches.

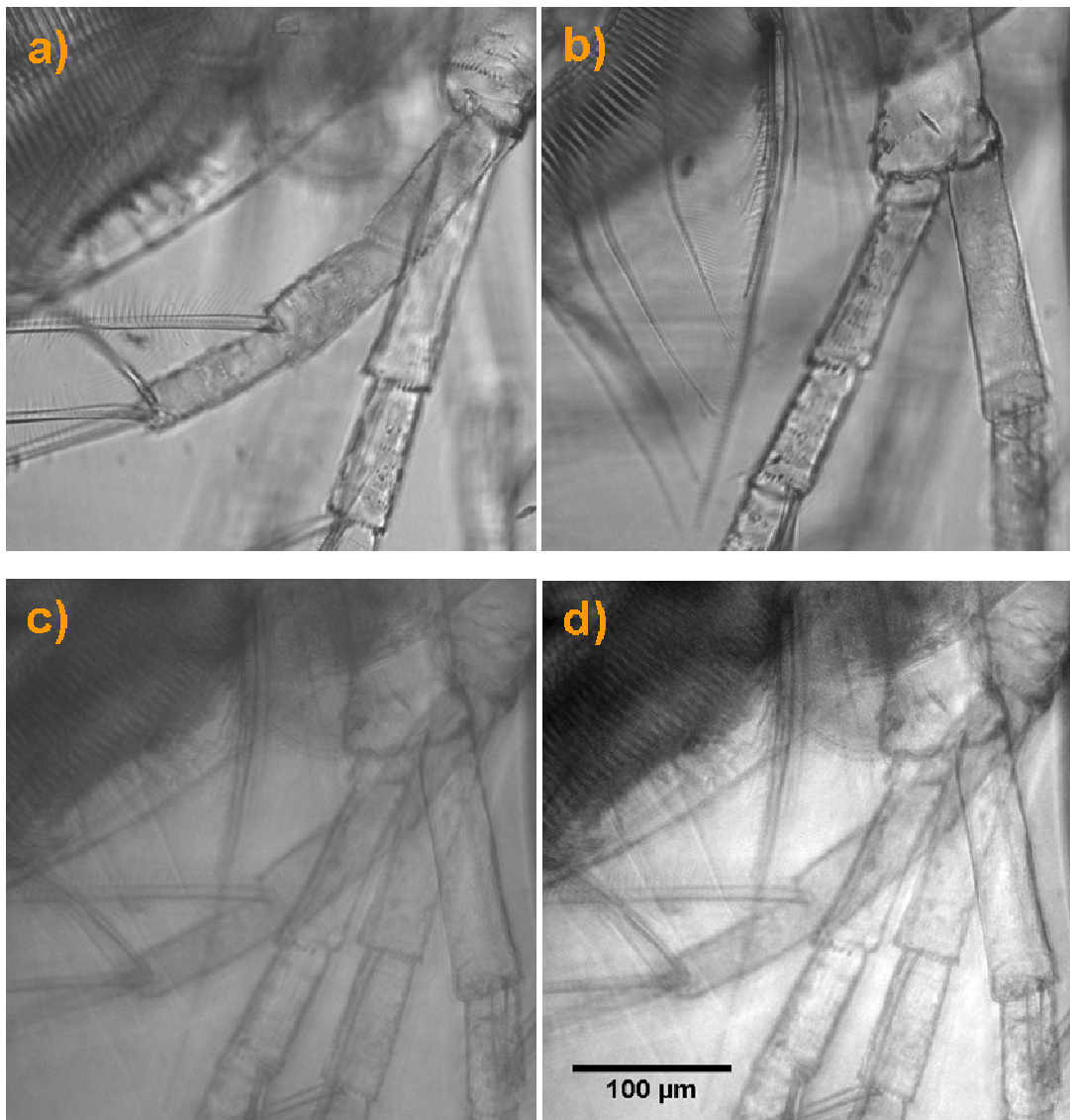


*Fig. 51: Antennae of *Daphnia galeata*. a-b): diffraction limited reference at two different positions, focused each on a pair of extremities. Lower pictures: image performed with a high DOF filter, raw picture (c) and after digital improvement of the brightness and contrast (d).*

A less magnified picture of a living *Daphnia galeata* is shown in *figure 52*. The four upper images were taken in diffraction limited arrangement at four different focal positions. The first picture is sharp at one of the antennae (*fig. 52a*), while the organelles and the border are blurry. The compound eye with its set of muscles and one of the liver lobes are sharp in *figure 52b*. The other liver lobe and the heart are the sharp parts in *figure 52c*. The last one is sharp at the other antenna, while the body is again blurry (*fig. 52d*).

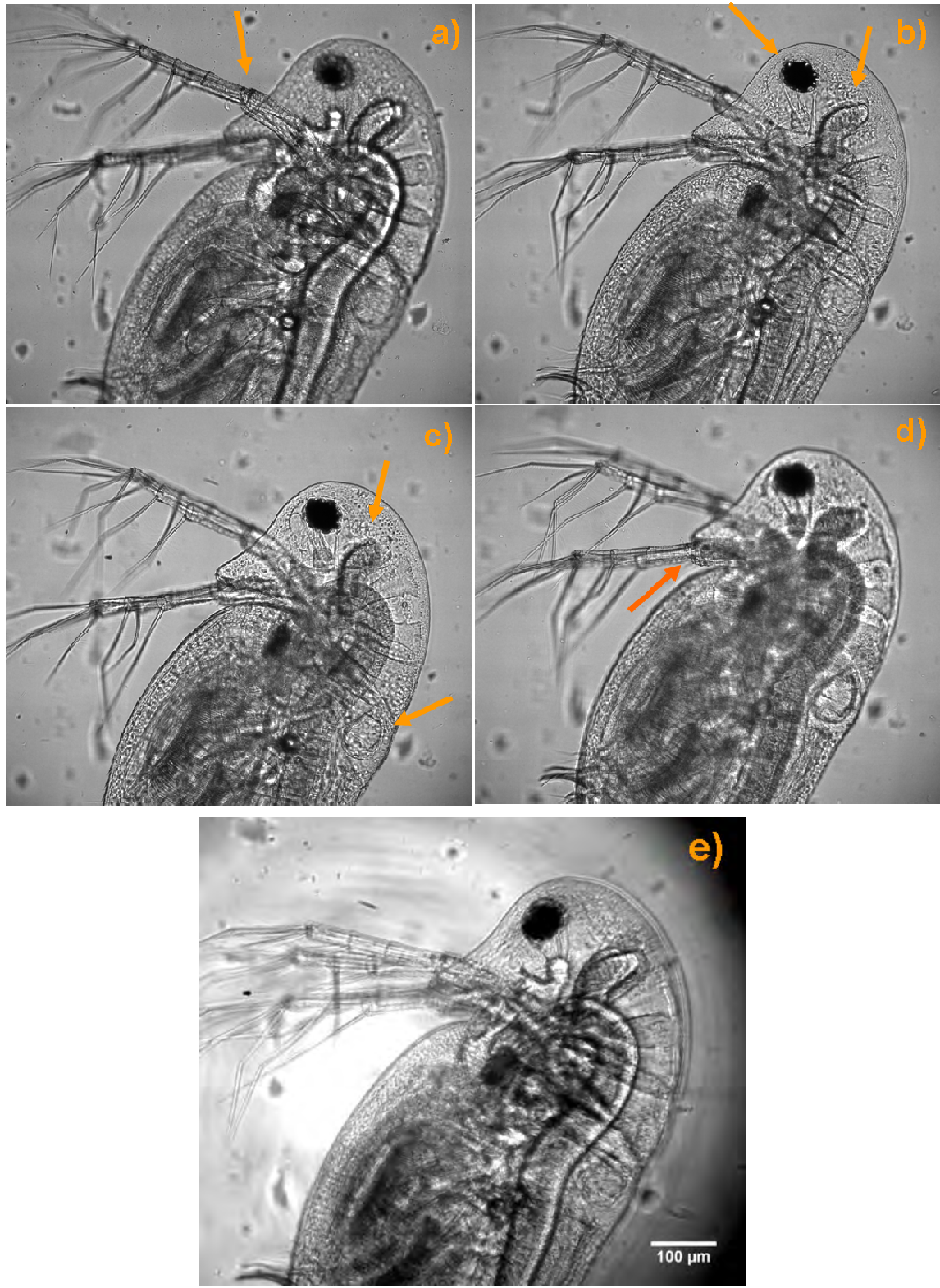


Fig. 52: Pictures of *Daphnia galeata* at 4 different focusing positions (a-d) in diffraction limited arrangement with arrows pointing at sharp features. The image with extended DOF lens (e) shows all features after adjustment of brightness and contrast.

The image performed with the extended DOF system had again a much lower contrast, but the adjustment of the brightness and image contrast helped again (*fig. 52e*). This time, the quartic term generating the DOF was much larger to cover the full depth of the animal. The higher DOF also extended the imaging field of the intermediate picture of the LED, which is slightly visible in the background. In the resulting image, however, all the mentioned features are simultaneously recognizable. Similar to the previous pictures, the full set of antennae with all branches can be observed. All the organelles as the eye with its muscles, both liver lobes, the gut and the heart can be evaluated. The border of the water flea can be examined all around. At regions where a lot of biological material was present, for example the belly part at the lower left side, all the images of the different overlapping features coincide and cannot be interpreted. This is a general problem for dense 3D objects and also present in diffraction limited pictures. A possible solution might be a specific marker, for example fluorescent beads, which highlights the important regions at different three-dimensional positions. The extended DOF lens would then image all the markers and therefore enhanced regions simultaneously.

To conclude, the image quality of the high DOF imaging system was quite good and an evaluation of the features possible for medium and large sized objects. For a detailed picture and very fine objects, the diffraction limited picture had to be examined. A possible imaging procedure might consist, first, of an overview picture with the extended DOF lens to analyze the existing objects and features. The second step would then be to focus on a specific feature of interest to take the highest resolved picture possible with the diffraction limited arrangement.

It is important to remember that the three-dimensional information is lost with the extended DOF lens. It is not possible to tell which antenna is below the other or how far they are separated. Other techniques such as z-scans can be performed in addition to the extended DOF modulation to obtain this information.

### 5.3. In-situ extraction of the refractive index and the thickness of a medium in imaging

The findings of *chapter 4* were converted from the focusing to an imaging application. The target was to obtain both, the refractive index and the physical thickness, of an unknown transparent medium, which was placed between the object and the imaging MO. The main idea of the method was to control the optical rays of the illumination of a focusing lens. The different behaviour of paraxial rays compared to marginal rays with large angles was used to obtain two focus shift measures, which then were used to calculate those two measures. To adapt the concept into an imaging application, we present a further reduction of the system by generating the controllable angle selection directly in-situ with the present phase SLM (*chap. 5.3.1*). The second step was to perform the measurement with a suitable feature within the object and a careful examination of the imaging generating process. The basic concept how to measure the medium is presented in *chapter 5.3.2*.

From these results, the appropriate phase modulation could be calculated to correct the induced spherical aberrations in the imaging setup (see *chapter 5.4*).

#### 5.3.1. Apertures generated in-situ by the phase SLM

A further simplification of the measurement set-up was achieved by generating the different apertures directly with the LCD phase modulator. With a phase-only modulation, the unwanted beams cannot be eliminated. Therefore, the idea was to spatially separate the unwanted rays from the ones containing the desired information. In our case, we introduced a quadratic phase modulation to defocus the unwanted regions of the aperture (*fig. 53*). In the PAR imaging mode, the inner rays passed without modulation while the outer rays became modulated, and vice-versa in case of MR imaging mode. The absolute value of the quadratic parameter  $A_1$  defined the defocusing distance of the regions.

The performance was validated in the focusing application and a similar measurement uncertainty of around 2-3 % was obtained compared to the introduced iris apertures.

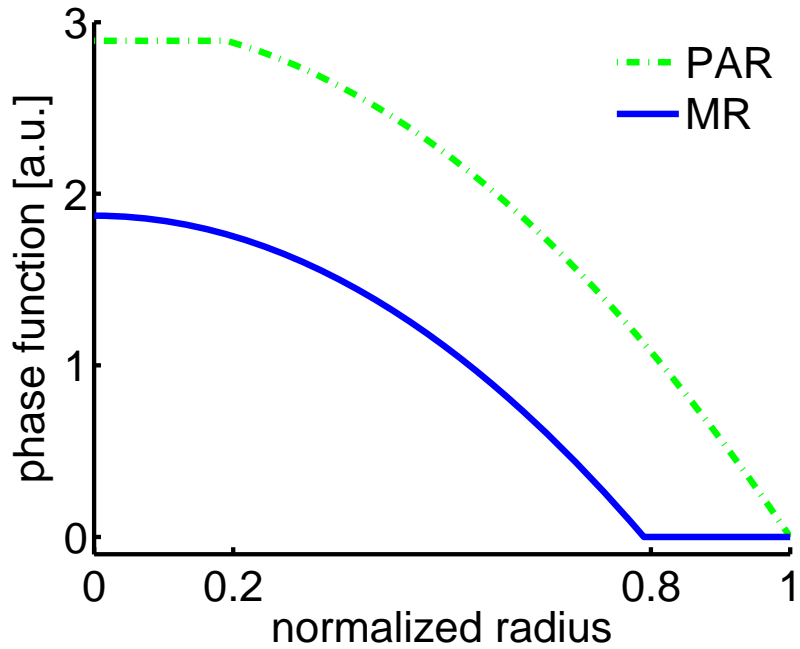


*Fig. 53: Quadratic radial symmetric phase sent to the modulator to separate paraxial (PAR) or marginal (MR) rays.*

To illustrate the conversion of the setup into an imaging arrangement, a schematic drawing of the imaging rays is shown in *figure 54*. Without any modulation, all the rays from the on-axis point source travel through the imaging MO and the tube lens onto the same spot on the camera (gray dotted lines), as long as the imaging system is aberration free. As a first approximation, we only observed on-axis objects.

In the PAR imaging mode (upper scheme in *fig. 54*), the outer imaging rays become shifted by the phase SLM. In that case, only the paraxial rays are focused on the camera to generate the picture, while the outer rays are focused behind the camera plane. This out-of-focus picture is overlaid on the camera as a blurry background. The MR imaging mode (lower scheme in *fig. 54*) is exactly the opposite. The outer rays with large angles are focused on the camera, while the paraxial rays become shifted and focus behind the camera plane. The sharp MR picture is again overlaid with a blurry background from the defocused paraxial picture.

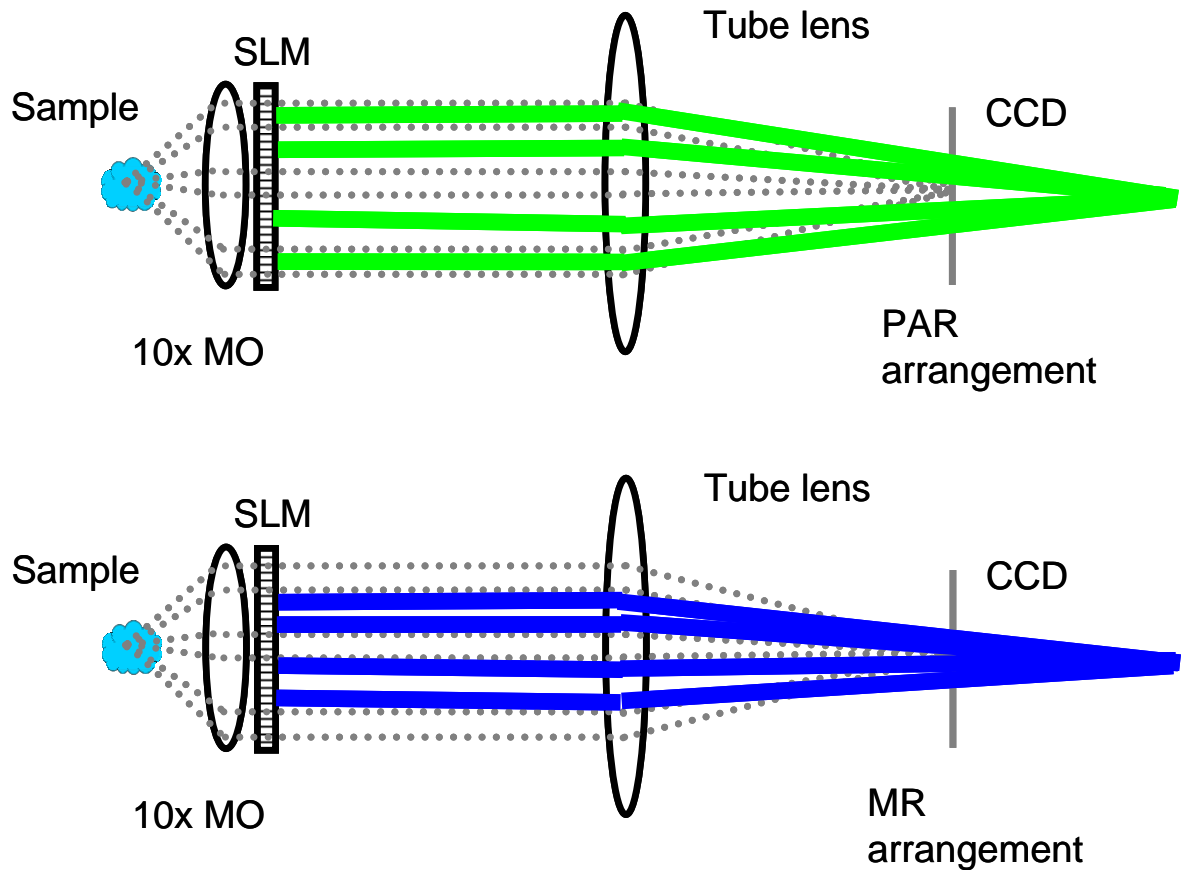


*Fig. 54: Schematic drawing of the image building process with in-situ generated apertures. Only the selected rays get imaged sharp on the camera: paraxial rays (upper scheme) or marginal rays (lower scheme).*

### 5.3.2. Evaluation concept of the unknown parameters of the medium

For the evaluation of the parameters of the unknown medium covering the object, the following procedure had to be performed: First, a punctual feature within the object has to be chosen that lays on axis of the imaging system. It is important that the object and the chosen feature within do not change during the whole characterization process. Otherwise, the relative measurements become unreliable. The positions of the best focus image under PAR and MR aperture mode were recorded. The reference position could be found by shifting the axial position until the surface of the medium became sharp, for example by focusing on a dust particle. The

resulting focus shifts for the PAR and MR imaging mode were then used with *equation 38* from *chapter 4* to calculate the refractive index and the physical thickness of the medium.

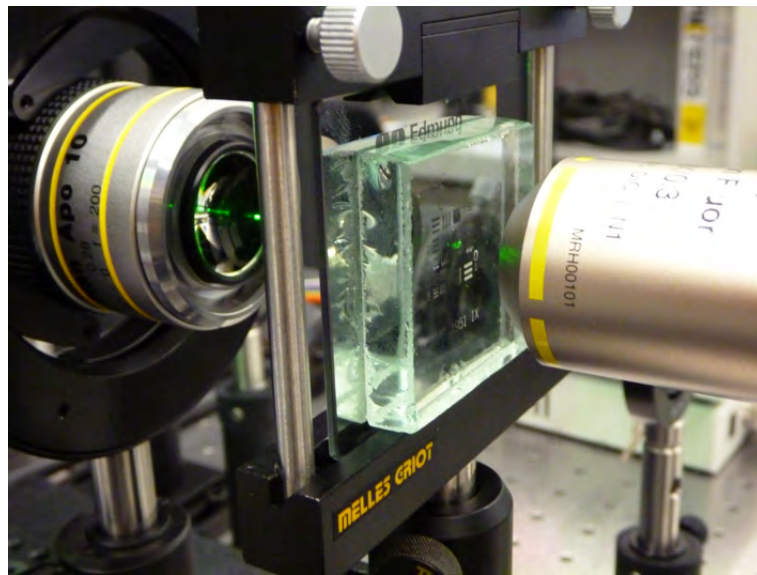


*Photo 4: MO arrangement for imaging through a glass plate.*

We have performed some test measurements to validate the method. Starting from the diffraction limited microscope arrangement, we introduced a 8 mm quartz glass between the object (line grating or USAF1951 target) and the imaging MO (*photo 4*). The reference position was obtained with a precision of around 1 micrometer. Results from the focusing application showed that this precision is enough to obtain measurement uncertainties of around 2-3 %. By applying the PAR aperture on the phase SLM, we observed an efficient defocusing of the unwanted region. In case of the MR aperture, however, the MR image of the on-axis object was pretty weak and overlaid by the blurry picture of the shifted PAR image. A precise evaluation of the best focus position was not yet possible and improvements in finding the exact focusing position are needed, especially for further use for full 3D objects. In addition, evaluations of measurement uncertainty and reproducibility have to be done. A fluorescent marker with strong intensity introduced into the sample might help finding the focal position within the target region.

In conclusion, we have presented a new complete system to simultaneously characterize an unknown transparent medium with its refractive index and thickness in an infinity corrected

brightfield microscope arrangement. The only additional part to the standard microscope setup is the phase SLM introduced with a pair of telescope lenses. The apertures can electronically be generated in-situ without modifying the object position or introducing additional optics. With the very same phase SLM, the introduced spherical aberrations can be corrected in a consecutive step (*chap. 5.4*).

In future studies, a consideration of a set of off-axis objects could give detailed information of the distribution of the medium's parameters. With a simultaneously performed analysis of several point sources within the object, a 2D map of an inhomogeneous aberration-inducing medium could be obtained. The consecutive aberration correction step would then be performed with an asymmetric correction function instead of the circular-symmetric correction function presented in the next sub-chapter.

### 5.4. Spherical aberration correction

Having obtained the parameters of the medium that induces the planar refractive index mismatch, the induced spherical aberrations (SA) can be corrected. In the following correction experiments, we imaged through an 8 mm thick quartz glass. The values obtained in *chapter 4.4* were then used for the correction phase function.

First, the aberrations arising from imaging through the glass are characterized over the full imaging field with the 80 lp/mm grating and the performance of the applied correction are analyzed. With a picture of a *Daphnia galeata*, the effect of SA in 3D biological samples is then presented together with an aberration correction.

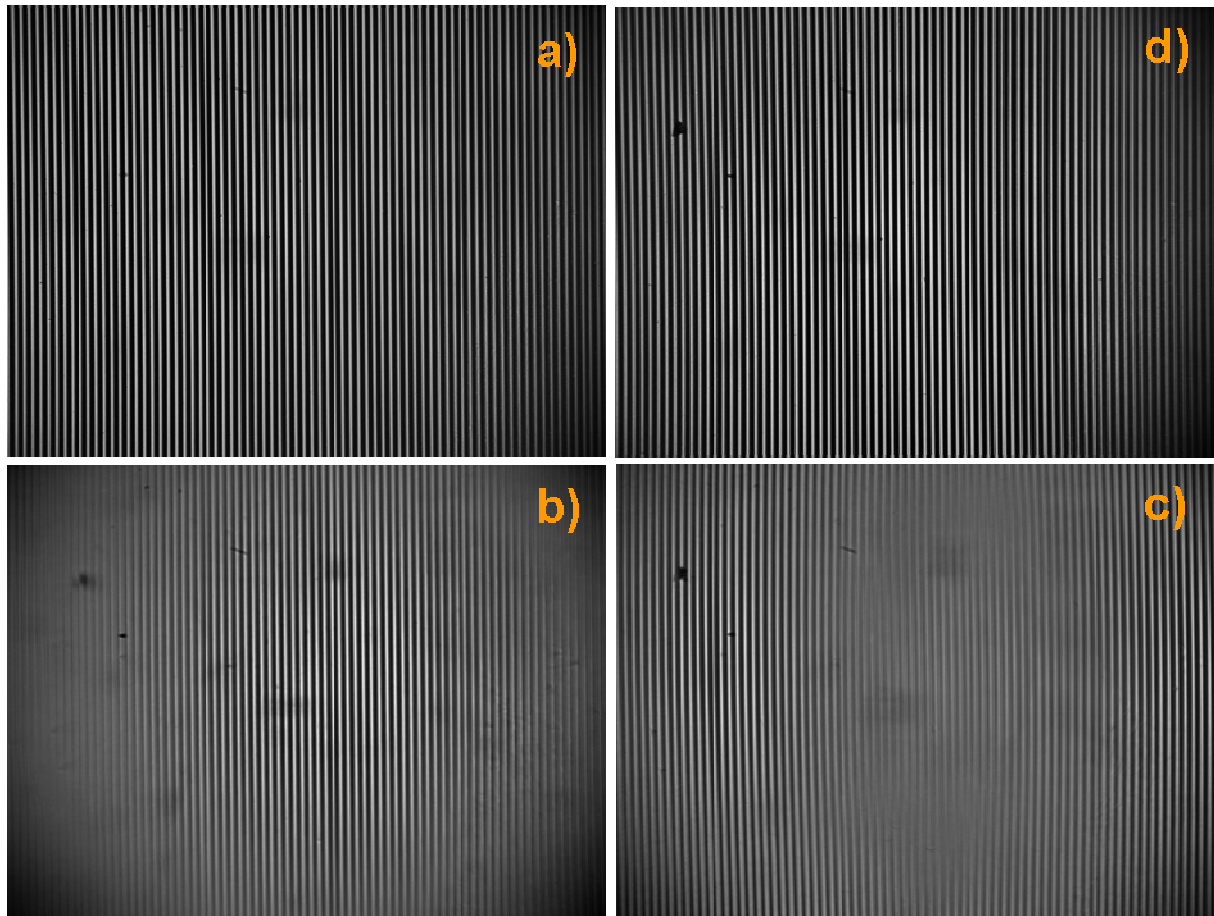


*Fig. 55: Spherical aberration correction performed with the 80 lp/mm grating. a) diffraction limited reference; imaged through a 8 mm quartz glass, either focused in the centre (b) or at the rim (c); d) imaged through a 8 mm quartz glass with aberration correction.*

Figure 55 presents the images obtained from the 80 lp/mm grating. The reference image was taken with the diffraction limited microscope setup (a). After introducing the quartz glass plate between the grating and the microscope objective, the image field got distorted. Two images were taken, one was focused in the middle (b) and the other at the rim (d). It can be clearly seen that the image field of a flat object became bent. After the spherical aberration correction with the phase SLM, the image became flat again with similar contrast as the reference (d).

To quantify the influence of the aberrations, line profiles through these images were taken (fig. 56). The contrast was more or less constant for the reference over the full image field.

The slight variation was due to inhomogeneous illumination and could be neglected. For the pictures taken through the glass (bottom pictures), the contrast was good either at the centre or at the rim, depending where the focal position was chosen. However, the contrast of the reference was restored again after the correction (top right).

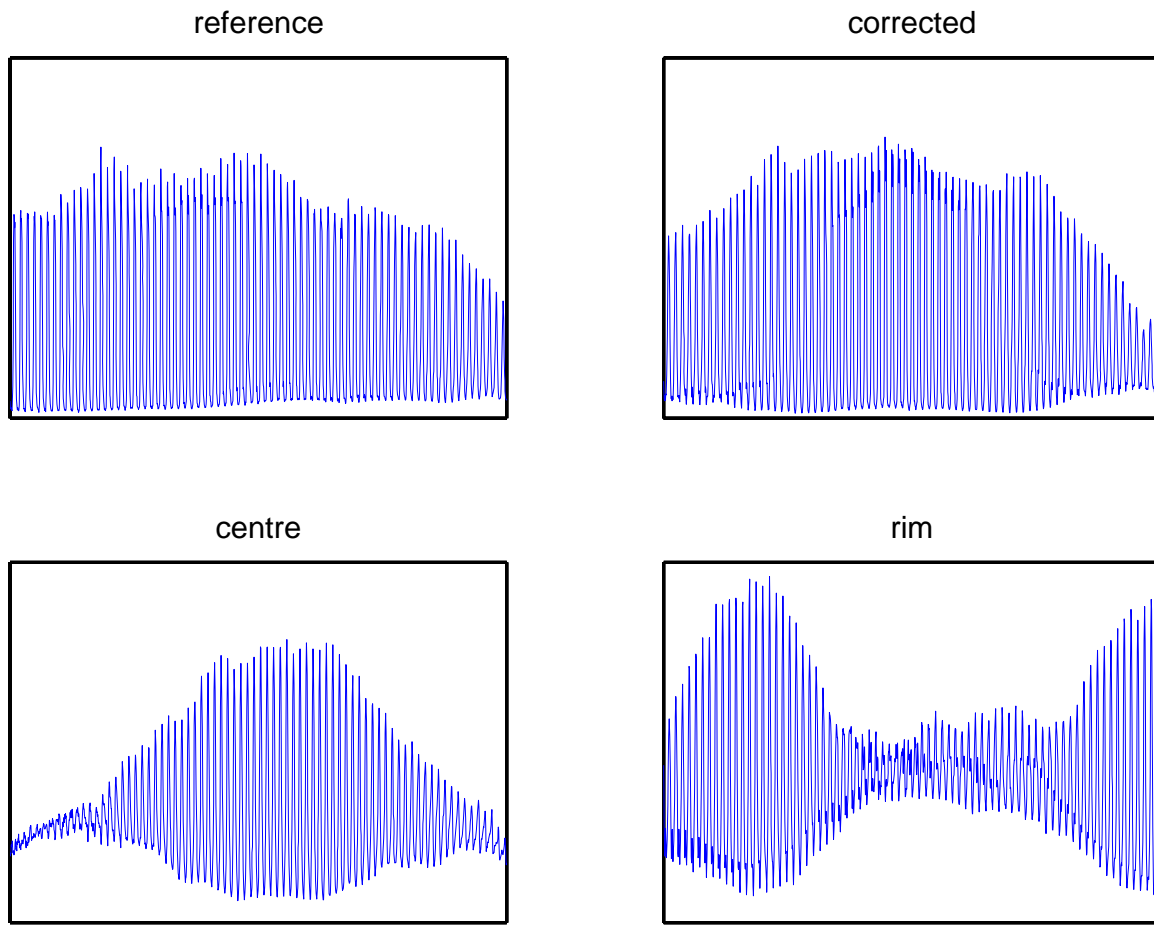


*Fig. 56: Line profiles of the 80 lp/mm grating with the same conditions as in figure 52.*

The distortion of the field was also shown with the shift of the focus position of the centre and rim positions (fig. 57). In this measurement, the previously presented four images were defocused and the contrast measured. The reference image of the grating (dotted black line) had at maximum position a contrast of 91 %, and then it dropped steadily with a depth of field (DOF) of around 0.1 mm over the full imaging field. The aberrated image at centre position (dash-dotted cyan line) had a very similar steepness and DOF, but a slightly lower maximum contrast of 80 % at the same position as the reference. At the rim (dashed violet line), the

steepness was much lower and the DOF was around 0.16 mm. As previously observed, the maximum position was lower with only 72 % contrast and was in addition shifted compared to the centre position, representing the distortion of the image field. After the correction of the aberrations (full red line), the initial distribution was restored over the full field with a maximum contrast of 88 % and the same steepness and DOF as the reference.

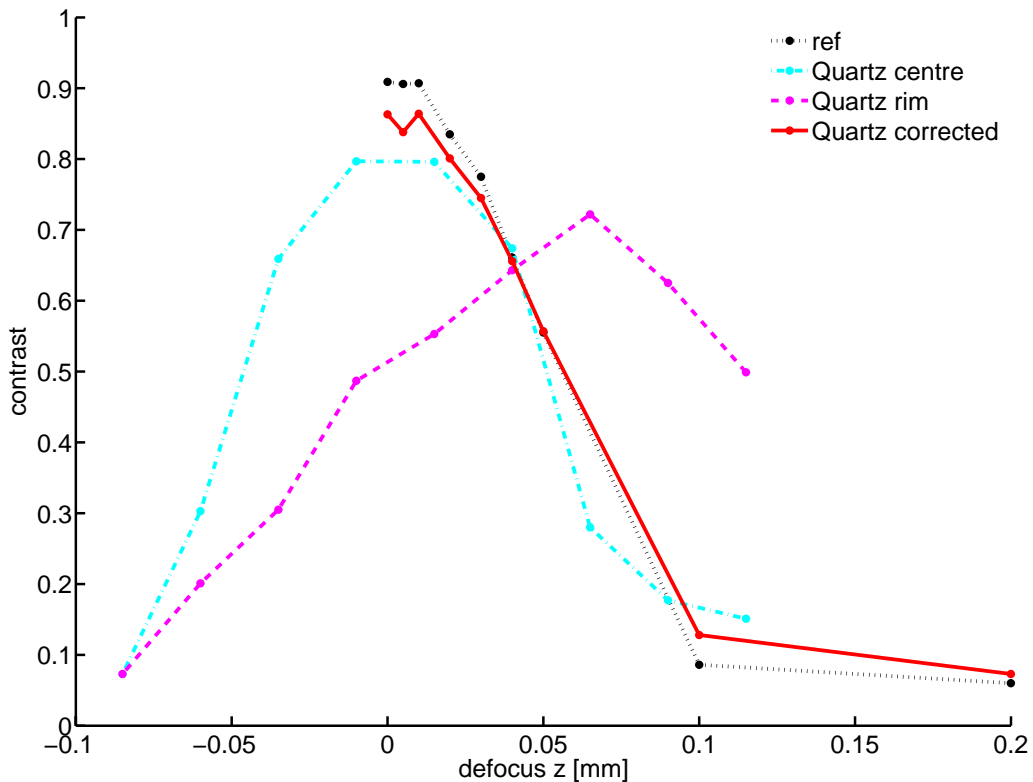


*Fig. 57: Contrast behaviour of the 80 lp/mm grating while defocusing during imaging through a 8 mm quartz glass.*

The analysis of the introduced spherical aberrations in a full 3D object was more difficult. Images of *Daphnia galeata* were taken with the same conditions: with the diffraction limited arrangement (*fig. 58a*), through the quartz glass (*fig 58b*) and through the glass with applied SA correction (*fig. 58c*). To compare the pictures, they were always focused at the green square in centre position, representing an on-axis object. At the rim, a reduction of image contrast was observed while imaging through the glass. The orange arrows indicate the most sig-

nificant regions, where the difference was clearly visible. The compound eye (feature 1), the pair of liver lobes (feature 2), the digestive tract (feature 3) and the heart (feature 4) showed a clear degradation compared to the reference. After the correction, the details were visible again, for example the pair of the liver.

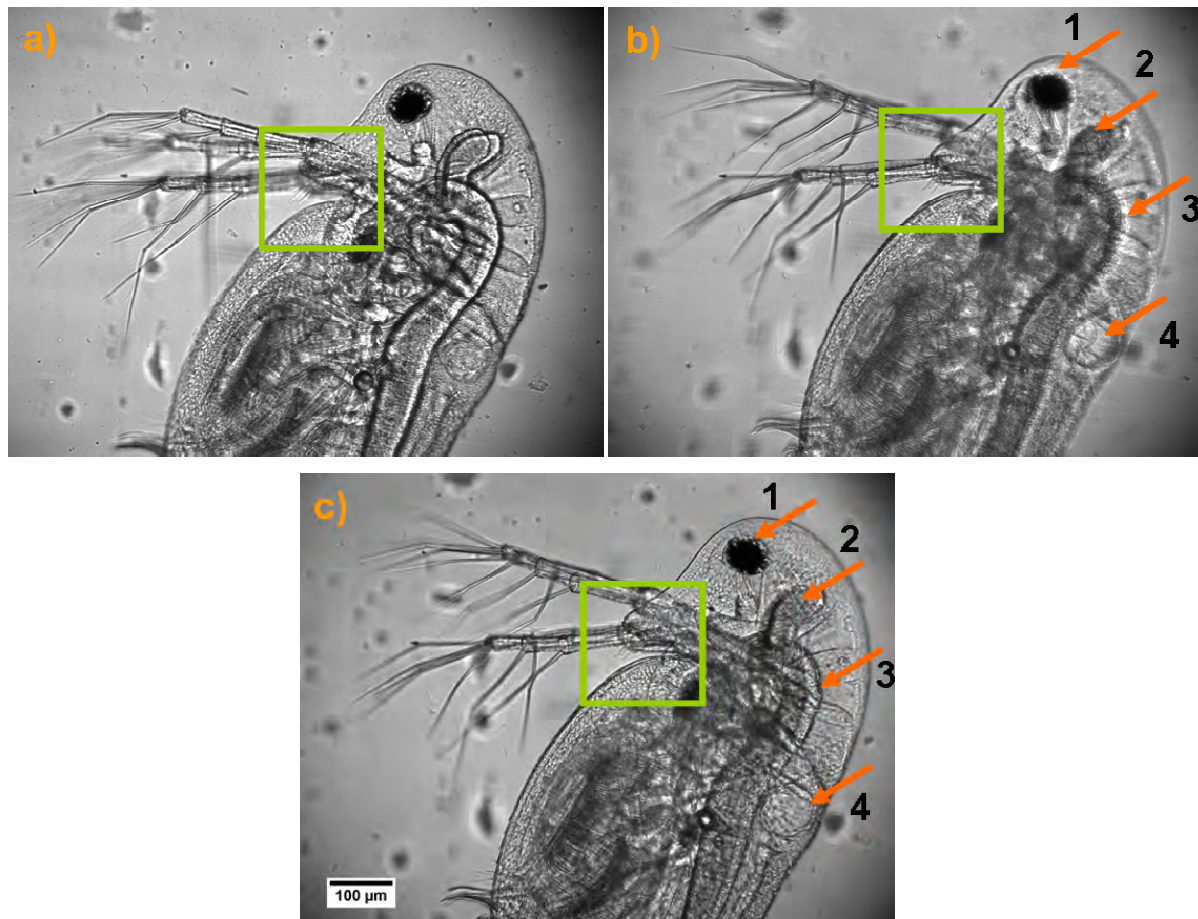


*Fig. 58: Imaging of *Daphnia galeata* with diffraction limited arrangement (a), through 8 mm quartz glass (b) and through quartz with spherical aberration correction (c). All pictures were focused in the green square. The arrows indicate regions where the aberration correction is clearly improving the image.*

For a more detailed quantification of MTF, a 2D Fourier transform (*fig. 59*) of the corrected and uncorrected images through the glass was performed of a partial region at the digestive tract (feature 3). The difference was not huge, but the frequency distribution covered a larger

range for the corrected image (right picture). This indicated a better contrast and resolution after correcting the SA.

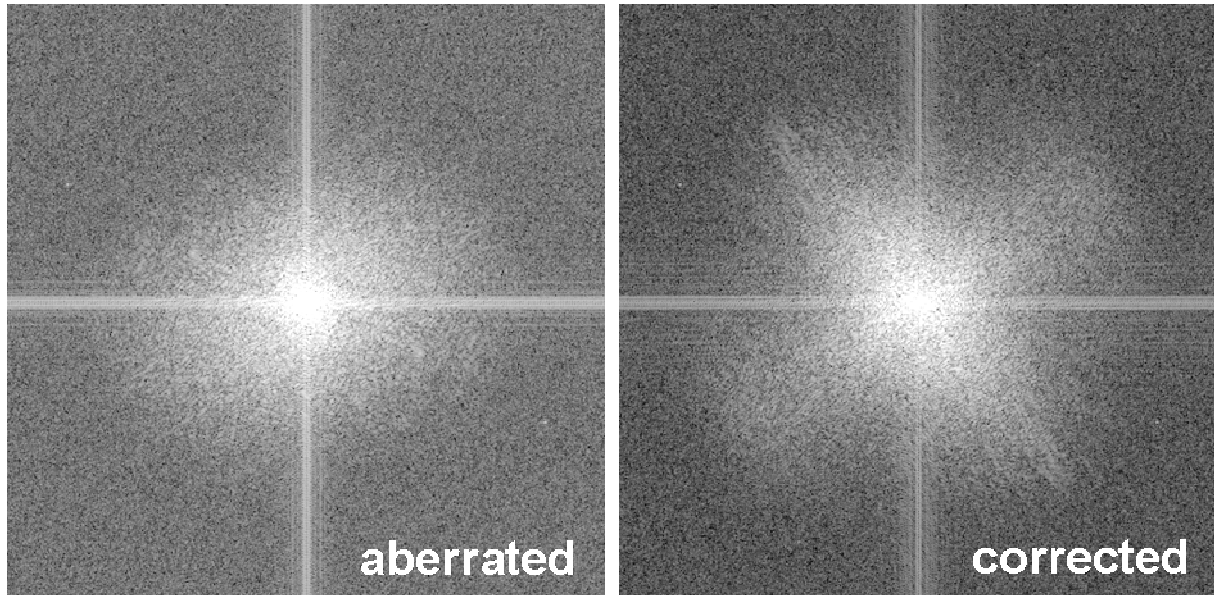


Fig. 59: Partial 2D Fourier-transform of the images through glass at position 3 in figure 55.

### 5.5. Conclusion

We have built an infinity corrected microscope with an implemented adaptive optics device for three applications. The performance of the different phase modulations was first characterized with a grating and then presented with a real biological sample, a water flea (*Daphnia galeata*).

The Quartic Multiplex pupil filter was able to extend the depth of field significantly. The 3D object was imaged in a single frame, making all the object features visible simultaneously. However, a reduction of the image contrast was observed, inhibiting the analysis of features close to the diffraction limit of the optical system. This could be improved with post-processing image contrast enhancements.

Second, the parameters of an unknown medium placed between the object under investigation and the imaging objective could be measured in-situ. With this wavefront-sensor-less method, the choice of the angle of the imaging rays was used to get two independent measurements of

the focus shift. From these two values, the refractive index and the physical thickness of the medium were calculated.

Finally, the obtained parameters of the medium were used to correct the spherical aberrations of the planar refractive index mismatch very efficiently. This provided a nearly diffraction limited performance while imaging through a thick glass plate. This method is applicable for many other imaging techniques as confocal, multiphoton and structured illumination microscopy and can be combined with further adaptive correction methods.

## 5. Adaptive Optics Implemented in Microscopy

# Chapter 6

## Conclusion

For the last 20 years, adaptive optics has been efficiently used in earth-bound astronomy to correct aberrations from atmospheric turbulences. However, the conversion of such systems into other imaging applications as microscopy or ophthalmology still needs major improvements and developments. We have developed new optical designs for phase pupil filters using simulations, and we have implemented adaptive phase modulation in two different optical arrangements: focusing laser light and imaging with a bright-field infinity-corrected microscope. The following three main results were obtained:

### High depth of field

We have focused a laser beam to a rod-like point spread function with a constant beam width similar to the diffraction-limited size. Compared to the state-of-the-art, our solution is beneficial in light efficiency, constant spot size and simplicity. The method requires only a single additional optical element, the spatial light modulator.

When implemented into a microscopic system, this enabled us to image objects from different distances sharply in a single camera frame. We have performed an inspection of a 3D object with a single optical image, without reducing the aperture as commonly used in photography. The image quality was further improved with a simple enhancement of the contrast.

## **6. Conclusion**

---

Because of this, in future, commercial microscopes might have such adaptive optics implemented. The development of a fully automated system can help in inspecting 3D objects. In ophthalmology, those designs might be implemented into the human eye as intra-ocular lens implants. An analysis of the image performance for the different object distances and under different lighting conditions has to be performed. Medical studies will show if our brain is able to process the new kind of input and adapt to the new 3D vision.

### **Characterization of an unknown medium**

Spherical aberrations are the main source of error when focusing through a medium. This induces a blurred picture or an ill-defined focal spot, thus degrading the performance of the optical system. We developed a two step correction procedure performed with a spatial light modulator. First, the refractive index and the thickness of an unknown medium were obtained using different incident angles. The choice of the incident rays was done with the adaptive optics phase element by separating the image of different lens regions in a very compact form. With this wavefront-sensor-less in-situ system, we were able to obtain a characterization accuracy of 2-3 % while focusing through the medium.

The current method is proven for on-axis objects within the optical imaging light path through the medium. However, this is sufficient for most applications in microscopic imaging, because the aberration inducing surrounding is, in many cases, approximately flat over the field of view. An enhancement of the method for off-axis points should be feasible, but needs a different mathematical basis to account for the different propagation angles. In addition, the introduction of a set of points to correct inhomogeneous aberrations over the full imaging field will improve the method significantly for complex samples. That step might need the use of adaptive feedback loops.

### **Correction of spherical aberrations**

The second step was to correct the spherical aberrations induced by the planar refractive index mismatch while focusing or imaging through the medium. We derived the needed phase functions using the parameters obtained from the characterization procedure. The correction was performed in the same system and we were able to completely correct a five-fold decrease of

## 6. Conclusion

the lens performance in both optical systems: for the focusing laser beam and in the microscope.

We have shown that both, the characterization of an unknown optical interface and the correction of the aberrated wavefront, are feasible with a single adaptive optical device (LCoS). This will allow building compact microscopes with only a few additional optical elements. Because the device can be digitally addressed, it will be possible to implement automated routines to adapt the wavefront correction in live-monitoring. Hence, real-time diffraction limited microscopy would be able in future and has a great potential in life cell biology. Furthermore, this method can be combined with other adaptive optics procedures to obtain the best possible correction needed.

## **6. Conclusion**

---

# Chapter 7

## Bibliography

1. M. Born, E. Wolf, and A. B. Bhatia, Principles of optics electromagnetic theory of propagation, interference and diffraction of light (Cambridge Univ. Press, Cambridge, 2005).
2. D. C. O'Shea, Diffractive optics design, fabrication, and test (SPIE Optical Engineering Press, Bellingham, WA, 2004).
3. G.-m. Dai, Wavefront optics for vision correction Guang-ming Dai (SPIE, Berlingham, Wash., 2008).
4. H. Gugel, J. Bewersdorf, S. Jakobs, J. Engelhardt, R. Storz, and S. W. Hell, "Cooperative 4Pi excitation and detection yields sevenfold sharper optical sections in live-cell microscopy," *Biophys. J.* **87**, 4146-4152 (2004).
5. M. Gu, Principles of three-dimensional imaging in confocal microscopes (World Scientific, Singapore, 1996).
6. M. Dyba, S. Jakobs, and S. W. Hell, "Immunofluorescence stimulated emission depletion microscopy," *Nat. Biotechnol.* **21**, 1303-1304 (2003).
7. E. Betzig, G. H. Patterson, R. Sougrat, O. W. Lindwasser, S. Olenych, J. S. Bonifacino, M. W. Davidson, J. Lippincott-Schwartz, and H. F. Hess, "Imaging intracellular fluorescent proteins at nanometer resolution," *Science* **313**, 1642-1645 (2006).
8. D. J. Stephens, and V. J. Allan, "Light microscopy techniques for live cell Imaging," *Science* **300**, 82-86 (2003).
9. R. K. Tyson, Principles of adaptive optics (Academic Press, Boston, 1998).
10. G. T. Di Francia, "Super-gain antennas and optical resolving power," *Il Nuovo Cimento* **9**, 426-438 (1952).

## 7. Bibliography

---

11. S. G. Lipson, "Why is super-resolution so inefficient?," *Micron* **34**, 309-312 (2003).
12. X. Gao, F. Zhou, W. Xu, and F. Gan, "Gradient force pattern, focal shift, and focal switch in an apodized optical system," *Optik* **116**, 99-106 (2005).
13. V. A. c. Sojfer, *Methods for computer design of diffractive optical elements* (Wiley, New York, 2002).
14. M. Born, E. Wolf, and A. B. Bhatia, *Principles of optics electromagnetic theory of propagation, interference and diffraction of light* (Cambridge Univ. Press, Cambridge, 2005).
15. J. W. Goodman, *Introduction to Fourier optics* (McGraw-Hill, New York, 1996).
16. K. D. Mielenz, "Algorithms for Fresnel diffraction at rectangular and circular apertures," *Journal of Research of the National Institute of Standards and Technology* **103**, 497-509 (1998).
17. M. Gu, *Advanced optical imaging theory* (Springer, Berlin, 1999).
18. L. Doskolovic, V. Kotjar, and V. A. c. Sojfer, *Iterative methods for diffractive optical elements computation* (Taylor & Francis, London, 1997).
19. W. H. Southwell, "Validity of the Fresnel Approximation in the near-Field," *Journal of the Optical Society of America* **71**, 7-14 (1981).
20. V. F. Canales, and M. P. Cagigal, "Pupil filter design by using a Bessel functions basis at the image plane," *Opt. Express* **14**, 10393-10402 (2006).
21. D. M. de Juana, V. F. Canales, P. J. Valle, and M. P. Cagigal, "Focusing properties of annular binary phase filters," *Optics Communications* **229**, 71-77 (2004).
22. D. Iwaniuk, E. Hack, and P. Rastogi, "Generation of a high depth of focus with constant transversal spot size using a phase-only pupil filter," *J. Mod. Opt.* **57**, 2141-2146 (2010).
23. V. Callegari, D. Iwaniuk, R. Bronnimann, E. Schmid, and U. Sennhauser, "Optimized fabrication of curved surfaces by a FIB for direct focusing with glass fibres," *J. Micro-mech. Microeng.* **19**, 5 (2009).
24. D. Iwaniuk, E. Hack, and P. Rastogi, "Generation of a high depth of focus with constant transversal spot size using a phase-only pupil filter," *J. Mod. Opt.* **57**, 2141-2146 (2010).
25. <http://en.wikipedia.org/wiki/Eye>.
26. <http://lasik.ucla.edu/los-angeles/vision-correction/multifocal-iols.htm>.
27. <http://www.allaboutvision.com/conditions/accommodating-iols.htm>.
28. <http://www.allaboutvision.com/conditions/multifocal-iols.htm>.
29. <http://lasikdoc.net/ucla/site/vision-correction/accommodating-iols.htm>.
30. C. J. R. Sheppard, J. Campos, J. C. Escalera, and S. Ledesma, "Two-zone pupil filters," *Optics Communications* **281**, 913-922 (2008).

## 7. Bibliography

---

31. C. J. R. Sheppard, J. Campos, J. C. Escalera, and S. Ledesma, "Three-zone pupil filters," *Optics Communications* **281**, 3623-3630 (2008).
32. Y. J. Zhang, "Design of three-dimensional superresolving binary amplitude filters by using the analytical method," *Optics Communications* **274**, 37-42 (2007).
33. P. N. Gundu, E. Hack, and P. Rastogi, "'Apodized superresolution' - concept and simulations," *Optics Communications* **249**, 101-107 (2005).
34. H. F. Zhu, M. J. Yun, H. Y. Gao, H. J. Gan, J. W. Chen, S. M. Zhou, and Z. Z. Xu, "Continuous radial superresolution filters with large focal depth," *J. Mod. Opt.* **53**, 1441-1450 (2006).
35. S. Ledesma, J. Campos, J. C. Escalera, and M. J. Yzuel, "Symmetry properties with pupil phase-filters," *Opt. Express* **12**, 2548-2559 (2004).
36. J. Rosen, B. Salik, and A. Yariv, "Pseudo-nondiffracting beams generated by radial harmonic functions," *Journal of the Optical Society of America A: Optics and Image Science, and Vision* **12**, 2446-2457 (1995).
37. M. A. Golub, V. Shurman, and I. Grossinger, "Extended focus diffractive optical element for Gaussian laser beams," *Appl. Optics* **45**, 144-150 (2006).
38. D. Zalvidea, C. Colautti, and E. E. Sicre, "Quality parameters analysis of optical imaging systems with enhanced focal depth using the Wigner distribution function," *J. Opt. Soc. Am. A-Opt. Image Sci. Vis.* **17**, 867-873 (2000).
39. S. M. Zhou, and C. H. Zhou, "Discrete continuous-phase superresolving filters," *Optics Letters* **29**, 2746-2748 (2004).
40. X. M. Gao, F. X. Gan, and W. D. Xu, "Superresolution by three-zone pure phase plate with 0, pi, 0 phase variation," *Opt. Laser Technol.* **39**, 1074-1080 (2007).
41. V. F. Canales, P. J. Valle, J. E. Oti, and M. P. Cagigal, "Variable resolution with pupil masks," *Optics Communications* **257**, 247-254 (2006).
42. X. M. Liu, L. R. Liu, D. A. Liu, and L. H. Bai, "Design and application of three-zone annular filters," *Optik* **117**, 453-461 (2006).
43. V. F. Canales, J. E. Oti, and M. P. Cagigal, "Three-dimensional control of the focal light intensity distribution by analytically designed phase masks," *Optics Communications* **247**, 11-18 (2005).
44. Z. Q. Liu, A. Flores, M. R. Wang, and J. J. Yang, "Diffractive infrared lens with extended depth of focus," *Opt. Eng.* **46**, 9 (2007).
45. A. Flores, M. R. Wang, and J. J. Yang, "Achromatic hybrid refractive-diffractive lens with extended depth of focus," *Appl. Optics* **43**, 5618-5630 (2004).
46. R. Liu, B. Z. Dong, G. Z. Yang, and B. Y. Gu, "Generation of pseudo-nondiffracting beams with use of diffractive phase elements designed by the conjugate-gradient method," *J. Opt. Soc. Am. A-Opt. Image Sci. Vis.* **15**, 144-151 (1998).

## 7. Bibliography

---

47. M. A. Golub, L. L. Doskolovich, N. L. Kazanskiy, S. I. Kharitonov, and V. A. Soifer, "Computer Generated Diffractive Multi-focal Lens," *J. Mod. Opt.* **39**, 1245 - 1251 (1992).
48. W. Fiala, and J. Pingitzer, "Analytical approach to diffractive multifocal lenses," *European Physical Journal-Applied Physics* **9**, 227-234 (2000).
49. E. Ben-Eliezer, Z. Zalevsky, E. Marom, and N. Konforti, "All-optical extended depth of field imaging system," *J. Opt. A-Pure Appl. Opt.* **5**, S164-S169 (2003).
50. C. Iemmi, J. Campos, J. C. Escalera, O. Lo?pez-Coronado, R. Gimeno, and M. J. Yzuel, "Depth of focus increase by multiplexing programmable diffractive lenses," *Opt. Express* **14**, 10207-10219 (2006).
51. J. A. Garcia, S. Bara, M. G. Garcia, Z. Jaroszewicz, A. Kolodziejczyk, and K. Petelczyc, "Imaging with extended focal depth by means of the refractive light sword optical element," *Opt. Express* **16**, 18371-18378 (2008).
52. L. B. Liu, C. Liu, W. C. Howe, C. J. R. Sheppard, and N. Q. Chen, "Binary-phase spatial filter for real-time swept-source optical coherence microscopy," *Optics Letters* **32**, 2375-2377 (2007).
53. S. Ledesma, J. C. Escalera, J. Campos, and M. J. Yzuel, "Evolution of the transverse response of an optical system with complex filters," *Optics Communications* **249**, 183-192 (2005).
54. V. F. Canales, and M. P. Cagigal, "Pupil filter design by using a Bessel functions basis at the image plane," *Opt. Express* **14**, 10393-10402 (2006).
55. M. Y. Yun, L. R. Liu, J. F. Sun, and D. A. Liu, "Three-dimensional superresolution by three-zone complex pupil filters," *J. Opt. Soc. Am. A-Opt. Image Sci. Vis.* **22**, 272-277 (2005).
56. S. Ledesma, J. C. Escalera, J. Campos, J. Mazzaferri, and M. J. Yzuel, "High depth of focus by combining annular lenses," *Optics Communications* **266**, 6-12 (2006).
57. J. A. Davis, C. S. Tuvey, O. Lopez-Coronado, J. Campos, M. J. Yzuel, and C. Iemmi, "Tailoring the depth of focus for optical imaging systems using a Fourier transform approach," *Optics Letters* **32**, 844-846 (2007).
58. Y. Xu, J. Singh, C. J. R. Sheppard, and N. Chen, "Ultra long high resolution beam by multi-zone rotationally symmetrical complex pupil filter," *Opt. Express* **15**, 6409-6413 (2007).
59. J. H. McLeod, "The axicon – a new type of optical element," *Journal of the Optical Society of America* **44**, 592-597 (1954).
60. A. Burvall, K. Kolacz, A. V. Goncharov, Z. Jaroszewicz, and C. Dainty, "Lens axicons in oblique illumination," *Appl. Optics* **46**, 312-318 (2007).
61. Z. Jaroszewicz, V. Climent, V. Duran, J. Lancis, A. Kolodziejczyk, A. Burvall, and A. T. Friberg, "Programmable axicon for variable inclination of the focal segment," *J. Mod. Opt.* **51**, 2185-2190 (2004).

## 7. Bibliography

---

62. S. L. Wen, J. Q. Su, J. Dong, F. H. Gao, Y. K. Guo, and Y. X. Zhang, "Spheric long-focal-depth lens," *Optics Communications* **278**, 14-16 (2007).
63. B. Z. Dong, G. Z. Yang, B. Y. Gu, and O. K. Ersoy, "Iterative optimization approach for designing an axicon with long focal depth and high transverse resolution," *J. Opt. Soc. Am. A-Opt. Image Sci. Vis.* **13**, 97-103 (1996).
64. A. Burvall, K. Kolacz, Z. Jaroszewicz, and A. T. Friberg, "Simple lens axicon," *Appl. Optics* **43**, 4838-4844 (2004).
65. J. W. Goodman, *Introduction to Fourier optics* (McGraw-Hill, New York, 1996).
66. C. Font, J. C. Escalera, and M. J. Yzuel, "Polychromatic Point Spread Function: Calculation Accuracy," *J. Mod. Opt.* **41**, 1401 - 1413 (1994).
67. W. J. Smith, *Modern optical engineering the design of optical systems* (McGraw-Hill, New York, 2008).
68. J. J. Stamnes, and D. Velauthapillai, "Focal shifts on focusing through a plane interface," *Optics Communications* **282**, 2286-2291 (2009).
69. E. J. Fernández, P. M. Prieto, and P. Artal, "Wave-aberration control with a liquid crystal on silicon (LCOS) spatial phase modulator," *Opt. Express* **17**, 11013-11025 (2009).
70. D. Iwaniuk, P. Rastogi, and E. Hack, "Correcting spherical aberrations induced by an unknown medium through determination of its refractive index and thickness," *Opt. Express* **19**, 19407-19414 (2011).
71. S. Labiau, G. David, S. Gigan, and A. C. Boccara, "Defocus test and defocus correction in full-field optical coherence tomography," *Opt. Lett.* **34**, 1576-1578 (2009).
72. D. Turaga, and T. E. Holy, "Miniaturization and defocus correction for objective-coupled planar illumination microscopy," *Optics Letters* **33**, 2302-2304 (2008).
73. P. N. Marsh, D. Burns, and J. M. Girkin, "Practical implementation of adaptive optics in multiphoton microscopy," *Optics Express* **11**, 1123-1130 (2003).
74. S. N. S. Reihani, and L. B. Oddershede, "Confocal microscopy of thick specimens," *J. Biomed. Opt.* **14**, 3 (2009).
75. D. S. Wan, M. Rajadhyaksha, and R. H. Webb, "Analysis of spherical aberration of a water immersion objective: application to specimens with refractive indices 1.33–1.40," *Journal of Microscopy* **197**, 274-284 (2000).
76. H. Hemmati, and Y. Chen, "Active optical compensation of low-quality optical system aberrations," *Opt. Lett.* **31**, 1630-1632 (2006).
77. L. Sherman, J. Y. Ye, O. Albert, and T. B. Norris, "Adaptive correction of depth-induced aberrations in multiphoton scanning microscopy using a deformable mirror," *Journal of Microscopy* **206**, 65-71 (2002).
78. M. J. Booth, "Wavefront sensorless adaptive optics for large aberrations," *Opt. Lett.* **32**, 5-7 (2007).

## 7. Bibliography

---

79. N. Ji, D. E. Milkie, and E. Betzig, "Adaptive optics via pupil segmentation for high-resolution imaging in biological tissues," *Nat. Methods* **7**, 141-U184 (2010).
80. P. Kner, J. W. Sedat, D. A. Agard, and Z. Kam, "High-resolution wide-field microscopy with adaptive optics for spherical aberration correction and motionless focusing," *J. Microsc.-Oxf.* **237**, 136-147 (2010).
81. H. Itoh, N. Matsumoto, and T. Inoue, "Spherical aberration correction suitable for a wavefront controller," *Opt. Express* **17**, 14367-14373 (2009).
82. J. W. Cha, J. Ballesta, and P. T. C. So, "Shack-Hartmann wavefront-sensor-based adaptive optics system for multiphoton microscopy," *J. Biomed. Opt.* **15**, 046022-046010 (2010).
83. W. J. Choi, D. I. Jeon, S. G. Ahn, J. H. Yoon, S. Kim, and B. H. Lee, "Full-field optical coherence microscopy for identifying live cancer cells by quantitative measurement of refractive index distribution," *Opt. Express* **18**, 23285-23295 (2010).
84. N. Lue, W. Choi, G. Popescu, Z. Yaqoob, K. Badizadegan, R. R. Dasari, and M. S. Feld, "Live Cell Refractometry Using Hilbert Phase Microscopy and Confocal Reflectance Microscopy," *J. Phys. Chem. A* **113**, 13327-13330 (2009).
85. B. Kemper, S. Kosmeier, P. Langehanenberg, G. von Bally, I. Bredebusch, W. Domischke, and J. Schnekenburger, "Integral refractive index determination of living suspension cells by multifocus digital holographic phase contrast microscopy," *J. Biomed. Opt.* **12**, 5 (2007).
86. N. Lue, G. Popescu, T. Ikeda, R. R. Dasari, K. Badizadegan, and M. S. Feld, "Live cell refractometry using microfluidic devices," *Opt. Lett.* **31**, 2759-2761 (2006).
87. W. Z. Song, X. M. Zhang, A. Q. Liu, C. S. Lim, P. H. Yap, and H. M. M. Hosseini, "Refractive index measurement of single living cells using on-chip Fabry-Perot cavity," *Appl. Phys. Lett.* **89**, 3 (2006).
88. H. Fujiwara, *Spectroscopic ellipsometry principles and applications* (Wiley, Chichester, 2007).
89. S. Kim, J. Na, M. J. Kim, and B. H. Lee, "Simultaneous measurement of refractive index and thickness by combining low-coherence interferometry and confocal optics," *Opt. Express* **16**, 5516-5526 (2008).
90. W. V. Sorin, and D. F. Gray, "Simultaneous thickness and group index measurement using optical low-coherence reflectometry," *IEEE Photonics Technol. Lett.* **4**, 105-107 (1992).
91. K. Lee, S. Y. Ryu, Y. K. Kwak, S. Kim, and Y. W. Lee, "Separation algorithm for a 2D refractive index distribution and thickness profile of a phase object by laser diode-based multiwavelength interferometry," *Rev. Sci. Instrum.* **80**, 5 (2009).
92. B. Rappaz, P. Marquet, E. Cuche, Y. Emery, C. Depeursinge, and P. J. Magistretti, "Measurement of the integral refractive index and dynamic cell morphometry of living cells with digital holographic microscopy," *Opt. Express* **13**, 9361-9373 (2005).





# Curriculum Vitae

## Daniel Iwaniuk

Affolternstr. 95

8050 Zürich

Date of birth 25<sup>th</sup> January 1983

Nationality Swiss

Civil status unmarried

Driving licence Cat. B

Telephone 076 321 50 30

Email Daniel@iwaniuk.ch



## Education

2007 – 2011	<b>PhD „Application of Adaptive Optics to Focusing and Imaging.“</b> Empa Dübendorf, Laboratory of Electronics / Metrology / Reliability Thesis Supervisor Prof. Pramod Rastogi, Applied Computing and Mechanics Laboratory, EPFL Lausanne
2005 – 2007	<b>Master of Science in Chemistry, ETH Zürich</b> Specialization: Physical Chemistry Final grade: 5.5
2002 – 2005	Bachelor of Science in Chemistry, ETH Zürich
2002	Matura Type C (Math), Örlikon, Zürich

## Work and project experience

2010	CTI Project „Development of intra-ocular lens implants with increased depth of focus“ with CCAT
2006	Master Thesis „High precision optical characterization of semiconductor saturable absorber mirrors for VECSELs“, Laboratory of ultrafast laser physics, Prof. Dr. U. Keller, Institute for Quantum Electronics, Department of Physics, ETH Zürich Grade: 6
2005	Semester Project „A HeNe-laser stabilized Étalon for absolute frequency locking of a near-infrared ring laser“, Prof. Dr. F. Merkt, Laboratory of Physical Chemistry, ETH Zürich

## **Research interest**

- Laser technology and development as a tool in material science, metrology and telecommunication
- Engineering of industrial optical and laser systems
- Imaging in biological applications, e.g. adaptive measurements in life-cell optical microscopy

## **Language skills**

German	Native language
Polish	2nd native language
English	Fluent in speaking and writing
French	School knowledge

## **IT skills**

Matlab	Extensive experience in application and programming
Labview	Extensive experience in application and programming
MS-Office	Advanced user
ImageJ	Advanced user
Zeemax	Intermediate user

## **Activities**

- Since 2004 member of the Badminton Club Irchel. Compete in the yearly Swiss championship and tournaments.
- Since 2010 chairman of the national Badminton tournament Irchel Classics with about 150 participants.

SCUBA diving

Reading science, science fiction and fantasy

Economy and stock market

Philosophy

## Publications

D. Iwaniuk, P. Rastogi, and E. Hack, *Correcting spherical aberrations induced by an unknown medium through determination of its refractive index and thickness*, Optics Express, vol. 19(20), p. 19407-19414, 2011.

D. Iwaniuk, E. Hack and P. Rastogi, *Generation of a high depth of focus with constant transversal spot size using a phase-only pupil filter*, Journal of Modern Optics, vol. 57(21), p. 2141-2146, 2010.

V. Callegari, D. Iwaniuk, R. Bronnimann, E. Schmid, U. Sennhauser, *Optimized fabrication of curved surfaces by a FIB for direct focusing with glass fibres*, Journal of Micromechanics and Microengineering, vol. 19, p. 5, 2009.

D. J. H. C. Maas, B. Rudin, A.-R. Bellancourt, D. Iwaniuk, T. Südmeier, and U. Keller, *High precision optical characterization of semiconductor saturable absorber mirrors*, Opt. Express, vol. 16, p. 7571-7579, 2008.

## Conference contributions

### **Presentation & Proceedings – Advanced Phase Measurement Methods in Optics and Imaging, Locarno, Switzerland:**

D. Iwaniuk and E. Hack, *Wavefront Modulation for an Elongated Depth of Focus with a Homogeneous Point Spread Function*. AIP Conference Proceedings, vol. 1236(1), p. 254-258, 2010

### **Poster – Biomedical Photonics Network (BMPN) Meeting, Bern, Switzerland:**

D. Iwaniuk, E. Hack and P. Rastogi, *White light pseudo-non-diffracting beam generated by a phase-only wavefront modulation*, Biomedical Photonics Network & Swisslaser.net, 2010

### **Presentation & Proceedings – Novel Techniques in Microscopy (NTM), Vancouver, Canada:**

D. Iwaniuk and E. Hack, *Measuring the 3D Point Spread Function of Super-Resolving Pupil Filters Focused into a Refractive Medium*, Novel Techniques in Microscopy, OSA Optical Society of America, paper NWB4, 2009

### **Presentation – Biomedical Photonics Network (BMPN) Meeting, St. Gallen, Switzerland:**

D. Iwaniuk, E. Hack and P. Rastogi, *Correcting the aberrations of a planar refractive index mismatch with a superresolution phase pupil-filter*, BMPN Biomedical Photonics Network, 2009

